
# Computational Analysis and Characterization of RC-135 External Aerodynamics

THESIS

Michael G. Chenery, Captain, USAF

AFIT/GAE/ENY/12-M06

**DEPARTMENT OF THE AIR FORCE**
**AIR UNIVERSITY**

***AIR FORCE INSTITUTE OF TECHNOLOGY***

**Wright-Patterson Air Force Base, Ohio**

AFIT/GAE/ENY/12-M06

# Computational Analysis and Characterization of RC-135 External Aerodynamics

THESIS

Presented to the Faculty

Department of Aeronautics and Astronautics

Graduate School of Engineering and Management

Air Force Institute of Technology

Air University

Air Education and Training Command

In Partial Fulfillment of the Requirements for the

Degree of Master of Science in Aeronautical Engineering

Michael G. Chenery, BS

Captain, USAF

March 2012

AFIT/GAE/ENY/12-M06

# Computational Analysis and Characterization of RC-135 External Aerodynamics

Michael G. Chenery, BS
Captain, USAF

Approved:

| | |
|---|---|
| Maj Andrew J. Lofthouse, PhD (Chairman) | 3/8/12 date |
| Mark F. Reeder, PhD (Member) | 08 Mar 12 date |
| Lt Col Ronald J. Simmons, PhD (Member) | 08 Mar 12 date |

# *Abstract*

Both the RC-135V/W Rivet Joint (RJ) and the RC-135U Combat Sent (CS) aircraft are United States Air Force (USAF) electronics reconnaissance platforms. The RJ is the USAF's standard airborne signals intelligence (SIGINT) gathering platform, while the CS is designed to collect technical intelligence on adversary radar emitter systems. Both aircraft are extensively modified C-135's characterized by protruding "cheek" fairings along the sides of the fuselage forward of the wings as well as the addition of numerous antennas along the top and bottom of the fuselage. The major distinguishing feature between the two variants is the nose radome, wherein the RJ has an elongated nose while the CS has the standard C-135 nose with a protruding "chin" radome along the underside. The RJ has recently experienced problems with antenna buffeting resulting in broken antennas and damage to the aircraft. Flight testing confirmed the presence of unsteady loading on certain antennas that has been traced back to the turbulent exhaust flow of a liquid cooling system (LCS) installed in the forward cheek fairings. Both variants have this modification but only the RJ has experienced structural damage. Computational fluid dynamics (CFD) was applied with the intention of characterizing the differences between the two variants. The LCS mass flow rate, angle of attack, and configuration of each variant was altered and results compared. Slight differences in the flow-field about each variant were noted with very similar turbulent fluctuations observed with the LCS installed. A strong correlation to angle of attack was confirmed while a weak correlation to mass flow rate was discerned.

*To Mom*

*Acknowledgements*

I would like to thank my research advisor, Maj Andrew Lofthouse, for all of the guidance, support, and wisdom bestowed on me over the course of this thesis effort. I would, also, like to thank my sponsor, David Stumpff, from the Big Safari Special Program Office in providing invaluable support and knowledge crucial to the completion of this project. John Staiger, from AFRL, proved to a much appreciated resource, providing much needed advice and training on the grid generation process. Additionally, this investigation would not have been possible without the use of the Raptor supercomputer maintained by the Air Force Research Lab Department of Defense Supercomputing Resource Center.

A special thanks goes out to our amazing Linux and HPC system administrators, Dave Doak and Don Bodle, without whom I would not have been able to reach this point. My fellow inhabitants of the Linux lab proved to be a priceless resource, serving as sounding boards, providing software-related guidance, and helping maintain the required sanity threshold needed to make it to graduation.

Michael G. Chenery

*Table of Contents*

Page

# *List of Figures*

# *List of Tables*

# Computational Analysis and Characterization of RC-135 External Aerodynamics

## I. Introduction

This research effort is driven by a need to better understand complex flow-fields around highly modified transport aircraft such that better decisions can be made concerning antenna placement. The RC-135V/W Rivet Joint has recently encountered problems with excessive antenna buffeting resulting in structural damage to both the antennas and fuselage skin. Despite a similar configuration with the exception of the forward fuselage geometry, the RC-135U Combat Sent has not experienced any structural damage. Flight testing has confirmed excessive vibration on multiple antennas on both variants related to a liquid cooling system (LCS) installed in the cheek radomes along the forward fuselage. Most importantly, this flight testing revealed that there is much that is not known about the flow field surrounding this highly modified family of aircraft and that more research is merited.

### *1.1 RC-135*

The RC-135 family of aircraft is derivative of a highly effective and proven airframe that has been widely utilized across not only the military but also the commercial markets to provide a variety of flexible and reliable services. The Boeing 367-80 was built in 1954 as a prototype jet transport aircraft that was designed, originally, to promote the advantages of jet airliners over the current propeller-driven airliners of the time. This prototype then developed into the C-135 military transport aircraft and later into the 707 commercial passenger jet. Many different variants emerged from the C-135 including the KC-135 Stratotankers and the RC-135 reconnaissance family of aircraft. The RC-135W traces it's lineage directly from the C-135B while the RC-135V and RC-135U are derivative of the RC-135B. The RC-135V and RC-135W

are considered aerodynamically identical as they have the same external configuration. The RC-135V/W variants are known as the Rivet Joint and are characterized by a long nose radome and cheek fairings as shown in Figure 1.1. The RC-135U


Figure 1.1: RC-135V/W Rivet Joint [1]

variant is known as the Combat Sent and is characterized by a short nose radome, chin radome, and cheek fairings in addition to antenna arrays on the wingtips and an extended tail as shown in Figures 1.2 and 1.4. Both the Rivet Joint and the Combat


Figure 1.2: RC-135U Combat Sent [1]

Sent variants are powered by four CFM International F108-CF-100 high bypass ratio turbofan engines. All airframe and mission systems modifications are handled by L-3

Communications out of Greenville, Texas under the oversight of the Big Safari Special Program Office out of Wright-Patterson Air Force Base in Dayton, Ohio. [10–12]

Each of the RC-135 variants has particular modifications that provide a unique capability to the war-fighter. The Rivet Joint's mission is to support theater and national level consumers with near real time on-scene intelligence collection, analysis and dissemination capabilities. The aircraft is highly capable through an extensive on-board sensor suite that allows the mission crew to detect, identify, and geolocate signals throughout the electromagnetic spectrum. An overview of the antennas installed on the Baseline 9 (BL9) configuration is shown in Figure 1.3. The crew can

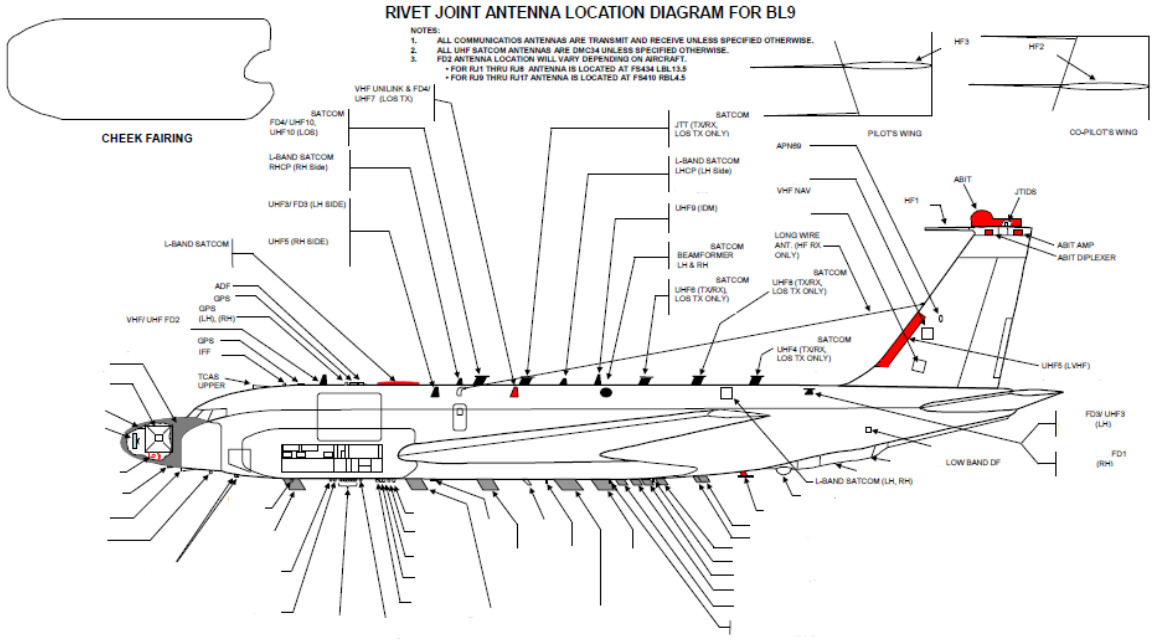


Figure 1.3: RC-135V/W Rivet Joint BL9 antenna locations [2]

also forward collected data in a variety of formats to numerous customers through an extensive communications suite. The mission crew consists of two pilots, one navigator, electronic warfare officers, and intelligence operators in addition to in-flight maintenance technicians. [10]

The Combat Sent's mission is to locate and identify foreign military land, naval, and airborne radar signals. The collected data is provided to the joint war-fighting

and intelligence communities for further analysis. The mission crew consists of two pilots, two navigators, two airborne systems engineers, and at least ten electronic warfare officers in addition to various electronic, technical, and area specialists. [11]

### *1.2 Motivation and Objectives of Current Research*

Since the end of the Cold War, as the focus has shifted from strategic to tactical threats, more and more requirements have been levied on the RC-135 program. This has led to a tremendous effort to equip an already crowded jet with more electronics and more sensors. This is in addition to the fact that many of these airframes have been in service since the early 1960s. In order to keep up with the demand for new capabilities and maintain an aging airframe, the RC-135 program follows a spiral development plan, wherein a new baseline is released every two years providing new capabilities to the war fighter. There is an extensive maintenance program with every aircraft rotating through the depot every four years for inspection, maintenance, and upgrades.

As this program has progressed, the already extensive on-board sensor suite has evolved and expanded. One of the byproducts of this progress has been the need for a better cooling system. To address this problem, a liquid cooling system (LCS) was installed in both the Rivet Joint and Combat Sent aircraft. This system consists of ducting through the forward cheek fairings feeding an internal radiator as shown in Figure 1.4. The Combat Sent was the first aircraft to have the LCS integrated and flew since the late 1990s with no problems relating to structural damage to antennas. Although, at this time the Combat Sent did not have the same antennas installed that would later cause problems with the Rivet Joint.

The first Rivet Joint variants with the LCS installed were delivered in January 2009 and by March of the same year, structural problems with the UHF3 antenna began to crop up as cracks were observed on the antenna. The most serious incident occurred in November 2009 when UHF3 broke off in flight and, in the process of doing so, liberated the HF long-wire mast and wire and left dents along the side of the aft


Figure 1.4: RC-135U Combat Sent showing LCS with louver installed over exhaust [1]

fuselage on the pilot side [3]. Figure 1.5 shows the resultant damage. Subsequent flight testing confirmed the increased antenna loading not only on UHF-3 but on the UHF-5 and UHF-7 Unilink antennas as well. [8, 13] It was found that there was significant loading on the antennas of the Combat Sent as well that could contribute to buffeting resulting in premature structural fatigue [7]. This problem is currently being investigated by Big Safari and L-3 Communications along with Air Force Research Labs (AFRL) support.

This effort has identified a gap in the analysis process occurring when a change to the external configuration is warranted. The changes are typically driven by new requirements relating to signal processing, i.e. new signal to receive and/or transmit. The location is determined, primarily from radio frequency (RF) requirements, but also with a subjective aerodynamic evaluation by senior L-3 Communications aerodynamics engineers. This evaluation is performed by engineers with many years of RC-135 specific experience relating to the application of a variety of antenna shapes. Additionally, L-3 Communications maintains a library of aerodynamic characteristics of commonly used shapes (blades, domes, balls, teardrops, etc.). This library

Figure 1.5: Damage to UHF3 and HF long-wire mast from the November 2009 incident [3]

is utilized by the engineers to define "keep out" zones aft of obstacles, wherein new structures should not be added. [13]

The latest modification to the external configuration merged two separate and successful configurations into one common configuration on each variant, with the exception of the "chin" on the Combat Sent. The cheek mounted cooling system was derived from the Combat Sent while the UHF3 and UHF5 antennas were originally installed on the Rivet Joint. The aerodynamic buffeting issue immediately became a problem with the Rivet Joint and later, to a lessor extent, with the Combat Sent when the UHF3 and UHF5 antennas were installed. [13]

In order to address these issues and prevent future problems, a better understanding of the external aerodynamics over complex configurations, such as the Rivet Joint and Combat Sent, is needed. The current methodology, although antiquated, has been successful, but the recent structural failures have pointed out it's weaknesses and, thus, a modified approach is warranted. The objective of this research is to provide an increased level of insight into the complex aerodynamics apparent with the

interaction of atypical fuselage shapes and numerous antennae in close proximity to one another.

Computational fluid dynamics (CFD) techniques are applied to both the Rivet Joint and Combat Sent variants with the objective of achieving a better understanding of the flow-field about each aircraft. Simplified models are compared with the exact same geometry on each model with the exception of the nose region. The antennas are modeled based on the Rivet Joint BL9 configuration and only the antennas along the upper fuselage are included. The geometry is varied by removing the LCS and antennas independently, resulting in four configurations for each variant. The mass flow rate and angle of attack is also varied for investigation of sensitivity to these parameters independently. Verification is provided in the form of a joint time step and grid refinement sensitivity study and validation is provided by means of comparison to flight test data.

This chapter has laid the foundation, identifying the root of the problem, familiarizing the reader with the RC-135 family of aircraft, and leaving the reader with the motivation and overall objectives of this research. Chapter II will describe the expected flow physics that will be encountered in this research and will delve into the analysis techniques that will be applied including the theory behind the applied flow solver, Kestrel. Additionally, the previous research applied to this problem will be discussed. Chapter III describes the research methodology: exploring the grid generation process, solver settings, and detailing the various studies to be undertaken in this effort. Chapter IV presents the results and Chapter V contains the conclusions and recommendations for future work.

# II. Background

This chapter presents a study of topics relevant to this research. Studying large aircraft aerodynamics is a difficult task whether by experimental or computational means. It is extremely difficult to produce a study that accurately captures every feature of the flow-field over an entire aircraft, therefore one must recognize the physics that would be expected and make simplifications such that the area and features of interest are brought into focus. In order to be able to accomplish this, a sound understanding of aerodynamic principles and computational fluid dynamics is required. In addition, an understanding of specialized post-processing techniques including spectral and vortex analysis is needed. Previous and ongoing research efforts also need to be discussed in order to better understand how this research effort will expand the knowledge base related to the ongoing problems.

## *2.1 Flow Physics*

The RC-135 aircraft operates primarily in the transonic flow regime. This regime has unique challenges not the least of which are the effects of compressibility. Additionally, the installation of the LCS imparts the complexity surrounding three-dimensional jet flow entering the flow-field resulting in high levels of vorticity likened to that observed off of wing tips or strakes. Even neglecting this feature, the complex configuration by itself demands interactions between the viscous boundary layer and shock waves along with regions of separated flow. Understanding the interactions among the various features inherent to this complex flow field is the focus of this research.

*2.1.1 Transonic Considerations.* The transonic flow regime is characterized by mixed regions of locally subsonic and supersonic flow and is apparent in flow over a body traveling at free-stream Mach numbers near unity. Almost all modern transport/utility aircraft operate in this regime as this is the highest velocity achievable in an efficient manner due to the drag divergence phenomenon. This phenomenon is characterized by a large increase in drag as the Mach number approaches unity.

Supersonic aircraft are designed to break through this barrier as quickly as possibly and thus spend as little time as possible in this regime due to the associated high drag penalties. The velocity at which this regime is first encountered is dependent on the body shape and is known as the critical Mach number and is defined as the Mach number at which sonic flow is first encountered on the body. Most transonic aircraft operate at or slightly above their critical Mach number in order to provide an optimal balance between velocity and drag. In actuality, the increase in drag is not significant until slightly past the critical Mach number. Although shock waves may occur, they are weak enough that they do not cause significant flow separation that is the source of this large increase in drag. Therefore, the drag-divergence Mach number must be defined as the free-stream Mach number at which this large drag rise begins. [14]

The characteristic of primary importance in the transonic regime is the presence of shock waves occurring at the termination of local regimes of supersonic flow. These shock waves are typically weak, incurring only a small total pressure loss, but the large adverse pressure gradient induced by the shock can lead to boundary layer flow separation. This is due to the fundamental nature of shock waves, in that they cause an almost discontinuous increase in pressure in the stream-wise direction. This increase in pressure in the direction of flow, otherwise known as an adverse pressure gradient, is universally known to lead to boundary layer separation. [14]

In aircraft design, there has been much research into increasing the critical Mach number (and thus drag-divergence Mach number) such as will expand the flight envelope for transonic aircraft or reduce the peak transonic drag for supersonic aircraft. These advancements include the introduction of thinner airfoils and swept wings, which both apply the concept of supercritical airfoils that utilize a lower thickness-to-chord ratio to provide higher critical Mach and lower peak drag. Another example is the transonic area rule that states that the cross-sectional area of the body should have a smooth variation with longitudinal distance along the body, which serves to decrease the peak transonic drag. [14]

The above theory focuses on the onset of the drag-divergence phenomenon that is caused by boundary layer separation. This research is more concerned with the effects of this shock wave/boundary layer interaction on the flow downstream rather than the effect on drag. There can be shock-induced separation in both inviscid and viscous flows alike and thus the presence of supersonic flow alone is not the only effect that must be examined. The addition of turbulence and the complexities inherent to boundary layers can cause additional complications and should be examined in more depth.

*2.1.2 Turbulence Theory.* Turbulence can be defined as an unsteady, three-dimensional, non-linear phenomena that occurs when inertial forces dominate viscous forces. The primary non-dimensional parameter used in describing turbulence is the Reynolds number, which is defined as the ratio of inertial to viscous forces:

$$Re_x = \frac{V_\infty x}{\nu} \tag{2.1}$$

where $V_\infty$ is the free-stream velocity, $x$ is a reference length, and $\nu$ is the kinematic viscosity. At low Reynolds numbers, the viscous forces act to damp out any disturbances in the flow but as Reynolds number increases the viscous forces are no longer able to adequately damp the overwhelming inertial forces. Mass and momentum transfer is higher within turbulent flows as related to laminar flows and shear/boundary layers tend to be thicker. [4]

Figure 2.1 shows how energy is partitioned among the varying turbulent eddy sizes. Wave number is inversely proportional to turbulent length scale. Most of the turbulent kinetic energy is in the larger eddies produced by instabilities in the mean flow. The smaller eddies then take energy from the larger energy producing eddies in the inertial regime, cascading down to the smallest eddies where the remaining kinetic energy is dissipated to heat due to viscous effects. For high Reynolds number flows, the smallest turbulent length scales can be on the order of $10^{-6}$ times that of the aircraft reference length. The Navier-Stokes equations provide the means to directly

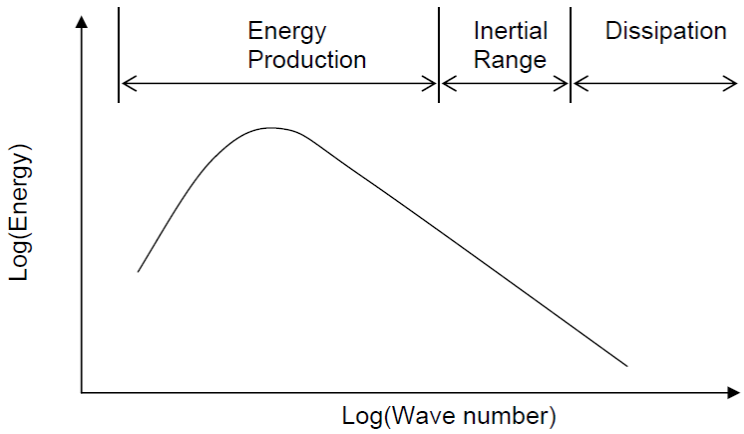


Figure 2.1: Turbulent energy spectrum [4]

simulate turbulent flows, yet in order to resolve the smallest turbulent length scale the number of grid points required to discretize an entire aircraft is astronomical and unrealistic with today's technology. [4]

The boundary layer is the viscous region of fluid next to a solid wall in which viscous effects dominate due to the fundamental requirement that velocity must be zero at the wall. The boundary layer thickness, $\delta_{99}$, is defined as the distance from the wall where viscous effects become negligible and the velocity is equal to 99 percent of local free-stream. Other parameters that must be introduced when examining boundary layers include $u^+$ and $y^+$ which are defined as:

$$u^+ = \frac{u}{u_\tau} \tag{2.2}$$

$$y^+ = \frac{\rho_w u_\tau y}{\mu_w} \tag{2.3}$$

where the friction velocity, $u_\tau$ is defined as:

$$u_\tau = \sqrt{\frac{\tau_w}{\rho_w}} \tag{2.4}$$

and the subscript $w$ is indicative of the value at the wall and the wall shear stress, $\tau_w$, is defined as:

$$\tau_w = \mu \frac{\partial u}{\partial y}\bigg|_w \tag{2.5}$$

The boundary layer can be divided into four layers comprising two regions. The inner region is broken down into the laminar sublayer ($0 < y^+ < 5$), the buffer layer ($5 < y^+ < 30$), and the log layer ($30 < y^+ < 1000$) while the outer region consists of the wake layer ($y^+ > 1000$). [4]

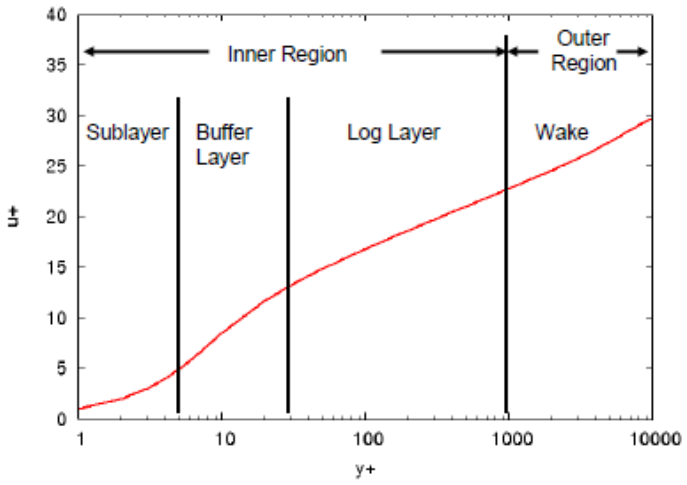


Figure 2.2: Boundary layer regions [4]

The boundary layer is highly sensitive to pressure gradients. An adverse pressure gradient is defined as $\partial p_0/\partial x > 0$ and occurs when $\partial u/\partial x < 0$. Conversely, a favorable pressure gradient is defined as $\partial p_0/\partial x < 0$ and occurs when $\partial u/\partial x > 0$. Separation occurs when $\partial u/\partial y <= 0$ and thus as wall shear stress becomes negative. Therefore adverse pressure gradients can lead to negative skin friction and thus boundary layer separation while favorable pressure gradients tend to stabilize the boundary layer. Turbulent boundary layers have the advantage that they can resist separation longer coupled with the disadvantages of increased wall friction and heat transfer. [4, 15]

## *2.2 Turbulence Modeling*

The most accurate method of simulating unsteady turbulent flows would be to use Direct Numerical Simulation (DNS) which directly solves the Navier-Stokes (NS) equations. In integral form, the Navier-Stokes equations are [16]:

$$\frac{\partial}{\partial t}\iiint_V \mathbf{Q}dV + \iint_S \left(\mathbf{f}\hat{i} + \mathbf{g}\hat{j} + \mathbf{h}\hat{k}\right)\cdot \hat{n}dS = \iint_S \left(\mathbf{r}\hat{i} + \mathbf{s}\hat{j} + \mathbf{t}\hat{k}\right)\cdot \hat{n}dS \qquad (2.6)$$

where the vector of conserved variables is defined as:

$$\mathbf{Q} = \begin{bmatrix} \rho \\ \rho u \\ \rho v \\ \rho w \\ \rho e \end{bmatrix}$$

the convective flux vectors are defined as:

$$\mathbf{f} = \begin{bmatrix} \rho u \\ \rho u^2 + p \\ \rho uv \\ \rho uw \\ \rho u(\rho e + p) \end{bmatrix} \quad \mathbf{g} = \begin{bmatrix} \rho v \\ \rho uv \\ \rho v^2 + p \\ \rho vw \\ \rho v(\rho e + p) \end{bmatrix} \quad \mathbf{h} = \begin{bmatrix} \rho w \\ \rho uw \\ \rho vw \\ \rho w^2 + p \\ \rho w(\rho e + p) \end{bmatrix}$$

and the viscous flux vectors are defined as:

$$\mathbf{r} = \begin{bmatrix} 0 \\ \tau_{xx} \\ \tau_{xy} \\ \tau_{xz} \\ a \end{bmatrix} \quad \mathbf{s} = \begin{bmatrix} 0 \\ \tau_{xy} \\ \tau_{yy} \\ \tau_{yz} \\ b \end{bmatrix} \quad \mathbf{t} = \begin{bmatrix} 0 \\ \tau_{xz} \\ \tau_{yz} \\ \tau_{zz} \\ c \end{bmatrix}$$

with:

$$a = u\tau_{xx} + v\tau_{xy} + w\tau_{xz} + \kappa T_x$$
$$b = u\tau_{xy} + v\tau_{yy} + w\tau_{yz} + \kappa T_y$$
$$c = u\tau_{xz} + v\tau_{yz} + w\tau_{zz} + \kappa T_z$$

In the above equations, $V$ is defined as the fluid element volume; $S$ is the fluid element surface area; $\hat{n}$ is the outward-pointing unit normal to $S$; $\rho$ and $p$ are density and pressure respectfully; $u$, $v$, and $w$ are the components of velocity; $e$ is specific energy per unit volume; $T$ is temperature; $\kappa$ is the thermal conductivity; and $\tau_{ij}$ is the viscous stress tensor. This results in five equations for six unknowns and the ideal gas law is typically used in order to close the system of equations. [16] The problem with using this method is that the computational domain would have to be refined enough such that the smallest turbulent scales are captured and the time steps small enough such that the full spectrum of turbulent frequencies are realized. This is impractical for all but the simplest geometries at low Reynolds numbers due to computational limitations. [4]

Reynolds-Averaged Navier-Stokes (RANS) was developed based on the assumption that the unsteady nature of the flow could be adequately modeled using empirically derived correlations. The RANS equations are derived by decomposing the NS equations into time-averaged and turbulent-fluctuation terms ($v_i = \overline{v_i} + v_i'$). The equations are essentially the same with the exception of being time-averaged and one additional term that is known as the Reynolds-stress tensor [17]:

$$\tau_{ij}^R = -\rho\overline{v_i'v_j'} = \begin{bmatrix} \rho\overline{(u')^2} & \rho\overline{u'v'} & \rho\overline{u'w'} \\ \rho\overline{v'u'} & \rho\overline{(v')^2} & \rho\overline{v'w'} \\ \rho\overline{w'u'} & \rho\overline{w'v'} & \rho\overline{(w')^2} \end{bmatrix} \tag{2.7}$$

Additionally, turbulent kinetic energy is defined as [17]:

$$K = \frac{1}{2}\overline{v_i' v_i'} = \frac{1}{2}\left[\overline{(u')^2} + \overline{(v')^2} + \overline{(w')^2}\right] \tag{2.8}$$

In order to close the RANS equations, some type of model must be applied such as will solve for the Reynolds-stress tensor. [4, 17]

The Spalart-Allmaras one-equation turbulence model is arguably the most popular model applied to turbulent flows today. Spalart and Allmaras developed this RANS model as a single transport equation for turbulent viscosity, $\tilde{\nu}$. This models the Reynolds-stress by applying the Boussinesq hypothesis [17]:

$$\tau_{ij}^R = 2\mu_T \overline{S_{ij}} - \frac{2}{3}\rho K \delta_{ij} \tag{2.9}$$

where $\overline{S_{ij}}$ is the Reynolds-averaged strain-rate tensor. In this equation, eddy viscosity $\mu_T$ is a proportionality factor and is related to turbulent viscosity by $\tilde{\nu} = \mu_T/\rho$. [17] It was derived using empiricism, dimensional analysis, Galilean invariance, and selective dependence on molecular viscosity. This model is fairly stable and reasonably accurate for varying turbulent flow regimes although this model is known to over-damp some unsteady flows. [4, 18]

There are significant limitations when applying RANS turbulence models to unsteady flows. These models tend to over-damp the inherent unsteadiness in the flow by producing an abundance of eddy viscosity. This problem stems from the basic assumption that all temporal and spatial scales of the unsteady turbulent motion are to be captured and modeled. RANS models are very accurate within the boundary layer but fail to adequately model highly unsteady separated flow regimes. Large Eddy Simulation (LES) was introduced as a compromise between DNS and RANS providing a practical means to simulate unsteady turbulent flows. In this method, the largest scales of turbulence are solved for directly while the smaller isotropic scales of turbulence are modeled using a subgrid model. LES requires the grid to be sufficiently

refined such that all of the anisotropic scales are captured and while LES is not as computationally expensive as DNS, it is still too expensive in the near-wall region of attached boundary layers for most practical use. [4]

Detached-Eddy Simulation (DES) is the latest approach to turbulence modeling which attempts to bridge the gap between RANS and LES such that can be applied to high Reynolds number separated flows. DES is designed to model the boundary layer completely using RANS while regions of separated flow are modeled using LES. This provides a balance between the high computational expense of LES and the inaccuracies of RANS outside of the boundary layer. In general, the determination of which mode of operation should be utilized is dependent on the length scale, $\tilde{d}$, that is passed down to the turbulence model in order to regulate the production of eddy viscosity: $\tilde{d} = min(d, C_{DES}\Delta)$ where $d$ is the wall distance, $C_{DES}$ is of order one, and $\Delta = max(\Delta x, \Delta y, \Delta z)$ is a typical measure of grid spacing although there are different methods of calculating this measure. The problem with this methodology is the large dependence on grid spacing. To illustrate this, Spalart et al. presents three different grid types for modeling a boundary layer as shown in Fig. 2.3. [5]

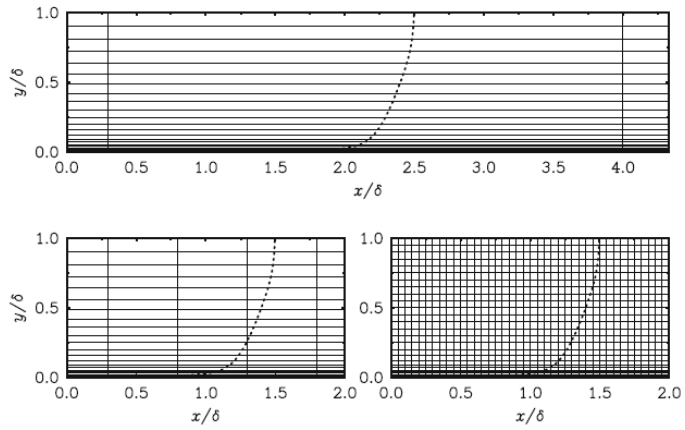


Figure 2.3: Grids in a boundary layer. *Top* Type I, natural DES; *left* Type II, ambiguous spacing; *right* Type III, LES. *Dotted lines* mean velocity. $\delta$ is the boundary-layer thickness. Assume $\Delta z \approx \Delta x \approx \Delta_{\parallel}$ [5]

The Type I grid is a typical boundary layer grid design both for RANS and DES wherein the grid spacing in the wall-parallel direction is much greater than the

spacing in the wall-normal direction. This allows for the wall-parallel spacing to set $\Delta$ and exceed the boundary layer thickness, $\delta$, thus ensuring that the model stays in RANS mode throughout the boundary layer since $\tilde{d} = d$ throughout. The Type III grid demonstrates what happens when both wall-parallel and wall-normal spacings are much smaller than $\delta$. This grid activates LES throughout most of the boundary layer as $\tilde{d} = C_{DES}\Delta$ that is ultimately effective but inefficient and even impractical for high Reynolds number flows due to the large grid size required. The Type II grid demonstrates the effects of having wall-parallel spacing smaller than the boundary layer thickness but not refined enough to resolve the fine velocity fluctuations within the boundary layer. This grid will activate LES throughout the upper two-thirds of the boundary layer and thus will under predict the eddy viscosity and ultimately the modeled Reynolds stress which is known as modeled stress depletion (MSD). MSD becomes an issue for complex geometries that may require the wall-parallel spacing to be much smaller in order to adequately capture the geometry or for regions approaching separation where the boundary layer grows to exceed the wall-parallel spacing. [5]

Delayed Detached-Eddy Simulation (DDES) was proposed by Spalart et al., as a derivative of the proposal by Menter and Kuntz [19], that is a modified form of DES that uses blending functions to protect the boundary layer and thus "preserve RANS mode" or "delay LES function." For one-equation versions of DDES a parameter, $r$, is introduced that is defined as the ratio (squared) of a model length scale to the wall distance or for an eddy-viscosity model such as S-A:

$$r_d \equiv \frac{\nu_t + \nu}{\sqrt{U_{i,j}U_{i,j}}\kappa^2 d^2} \tag{2.10}$$

where $\nu_t$ is the kinematic eddy viscosity, $\nu$ the molecular viscosity, $U_{i,j}$ the velocity gradients, $\kappa$ the Karman constant, and $d$ the distance to the wall. This parameter is designed to be equal to one in the logarithmic layer and fall to zero towards the edge

of the boundary layer. This parameter is then used in the blending function:

$$f_d \equiv 1 - tanh([8r_d]^3) \tag{2.11}$$

which is designed to be one in the LES region, where $r_d << 1$, and zero elsewhere. This new function can now be applied by redefining the DES length scale:

$$\tilde{d} \equiv d - f_d max(0, d - C_{DES}\Delta) \tag{2.12}$$

where $f_d = 0$ activates RANS mode ($\tilde{d} = d$) and $f_d = 1$ activates conventional DES ($\tilde{d} = min(d, C_{DES}\Delta)$). This reformulation results in a dependence not only on the grid but adds a time dependence as well as a dependence on the eddy-viscosity field. This has been proven to prevent MSD problems and provide a more robust and flexible solution to complex high Reynolds number separated flows. [5]

## *2.3 Computational Fluid Dynamics*

Computational fluid dynamics (CFD) is the process of simulating fluid flows by numerically solving the governing equations as defined by conservation of mass, momentum, and energy. The governing equations take many forms such as that of the Navier-Stokes and RANS equations presented in Section 2.2. There are many different forms of these equations based on what assumptions the user is willing to make. The Euler equations are a simplified form of these equations that neglects viscous effects. No matter what equations are to be applied the overall process is the same with three major components involved: grid generation, flow solver, and post-processing. The grid generation and flow solver components will be examined in more depth in the next two sections. Post-processing is the process of analyzing the flow solution data produced by the flow solver.

*2.3.1 Grid Generation: ANSYS ICEM CFD.* Before solving the governing equations the spatial domain must be discretized. This includes both the discretiza-

tion of all boundary surfaces as well as the volume enclosed within. This is commonly known as grid generation and there are two basic methods to choose from including structured and unstructured grids. When using either method, this process starts with a model being imported from a Computer Aided Design (CAD) program into a grid generation program. Typically, the data imported from CAD has imperfections including discontinuities or overlaps between surfaces, missing surfaces, etc. Therefore, the first step is always to perform geometry repair which can be a difficult task in and of itself.

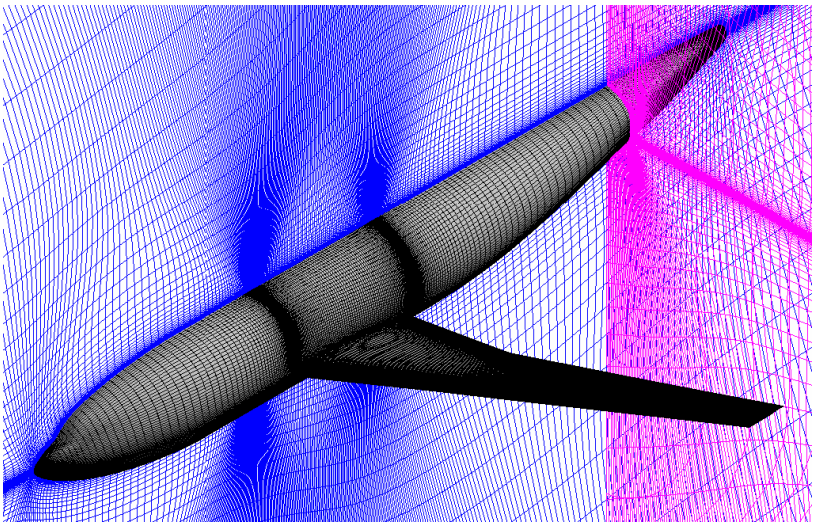

Figure 2.4: Example of a structured grid [6]

There are two major approaches to grid generation: structured and unstructured. Structured grids are ones in which the connectivity is easily mapped within a data structure in computational space. An example is shown in Figure 2.4. This type of grid has the advantage of containing regularly shaped cells, ease of computational indexing, and is great for boundary layers where high aspect ratio cells are desired in order to better capture the wall normal gradients. Unfortunately, a structured grid is difficult to apply to complicated geometries and results in non-orthogonality and highly skewed cells, which can add error to the numerical solution. For this research, an unstructured tetrahedral grid generation technique was chosen as it provides the advantage of being able to discretize complex geometries quickly and with a minimum

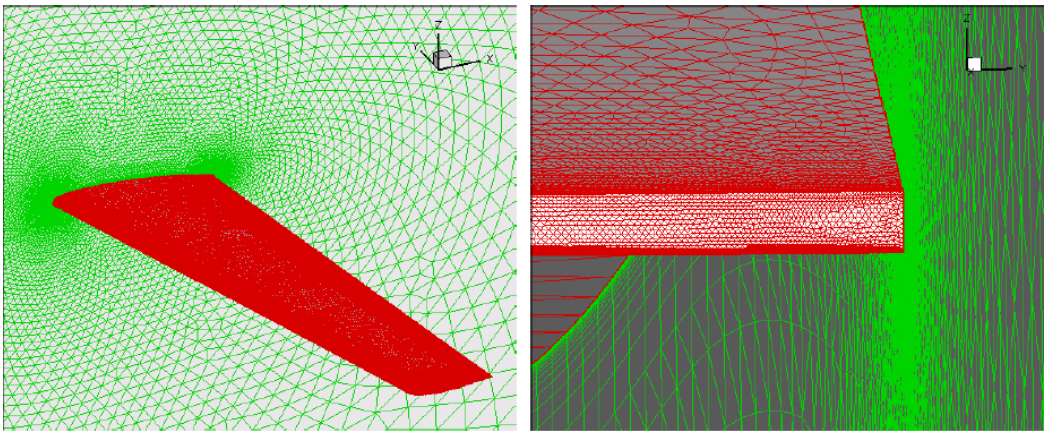

Figure 2.5: Example of an unstructured grid [6]

of user intervention. An example of an unstructured grid is shown in Figure 2.5. The flow solver being used in this investigation is designed specifically for unstructured grids.

*2.3.2 Flow Solver: CREATE-AV/Kestrel v2.1.2.* Kestrel is an aircraft simulation software package developed by the Computational Research and Engineering Acquisition Tools and Environments Air Vehicles project (CREATE-AV). It was created to aid in the Department of Defense (DOD) fixed-wing aircraft acquisition process by providing accurate, timely, and easy-to-use simulations to users across the design process. Kestrel provides many capabilities including prescribed motion, six-degree-of-freedom rigid body motion, mesh deformation, and control surface deflections in addition to providing the classical static simulation capability as is applied in this study. All of these various components are linked to the most important component, the flow solver. The flow solver integrated into Kestrel is based on the Air Vehicles Unstructured Solver (AVUS) developed by Air Force Research Labs CFD Research Branch (AFRL/RBAC) in the 1990s. The Kestrel team originally chose this solver for its performance, feature set, accuracy, maintainability, and availability of source code and the modified version is known as kAVUS. [20]

The kAVUS component is a finite-volume, cell-centered solver that provides the ability to solve axi-symmetric, two- or three-dimensional, unsteady, compressible

Reynolds Averaged Navier-Stokes (RANS) equations on hybrid unstructured grids. First-order temporal and spatial accuracy is provided by Godunov's exact Riemann method [21]. Second-order spatial accuracy is achieved by applying a least-squares reconstruction [22]. First- and second-order temporal accuracy is provided by Tomaro's unconditionally stable point-implicit scheme with Newton sub-iterations applied for increased accuracy [23]. Temporal damping coefficients are applied, which control the diagonal dominance of the flux Jacobian matrices. These coefficients damp out the errors associated with the temporal integration scheme, improving stability at the expense of temporal accuracy. In order to produce a Navier-Stokes solver the viscous terms patterned after MacCormack are applied to the above inviscid algorithm [24]. The temporal accuracy is unaffected by the addition of these viscous terms. The following turbulence models are available:

- Spalart-Allmaras one-equation
- Delayed Detached Eddy Simulation (DDES) with Spalart-Allmaras
- Wilcox k-$\omega$ two-equation
- Wilcox k-$\omega$ two-equation with Shear-Stress Transport (SST)
- Menter's baseline (BSL) model
- BSL model with SST

Wall functions are also available for all turbulence models using adiabatic no-slip wall boundary conditions. [20]

### *2.4 Vortex Analysis*

Vortices can be found in both turbulent, viscous flows and inviscid flows alike. This flow feature is simply a region of rotationality in the flow field. A great example is the longitudinal vortices shed off of the wing tips. This same effect can be seen in other locations as well such as sharp junctions at wing/fuselage intersection that can often be the source of longitudinal vortices that will effect the flow downstream.

When examining vortices, both the vorticity and strain tensors must be taken into account. The vorticity tensor is defined as:

$$\Omega_{ij} = \frac{1}{2}\left(\frac{\partial u_i}{\partial x_j} - \frac{\partial u_j}{\partial x_i}\right) \tag{2.13}$$

The largest magnitudes of vorticity should occur in the boundary layer and in the core of a vortex. The rate-of-strain tensor is defined as:

$$S_{ij} = \frac{1}{2}\left(\frac{\partial u_i}{\partial x_j} + \frac{\partial u_j}{\partial x_i}\right) \tag{2.14}$$

The largest magnitudes of rate-of-strain will also be found near the wall in the boundary layer while the magnitude of strain should be near zero in a vortex core. [4]

Historically, the definition of a vortex is very subjective identifying structures with rotating reference frames relative to one another. Regions of high vorticity, as defined above, are then used to identify vortex regions. This is not always the most accurate methodology, therefore Hunt, Wray and Moin [25] introduced the Q-criterion, which defines a vortex as a spatial region where the vorticity tensor dominates that of the rate-of-strain tensor or:

$$Q = \frac{1}{2}\left[|\Omega|^2 - |S|^2\right] > 0 \tag{2.15}$$

Ultimately, this results in two different parameters for examining vortex regions where vorticity defines the larger vortex structures and Q-criterion defines the smaller scales of the vortex structure. [26]

### *2.5 Spectral Analysis*

Since the flow-field examined in this study exhibits highly unsteady time dependent features, spectral analysis is applied in order to better understand what is going on. The Fourier function can be used to break a signal down into its spectral components in the frequency domain. The Fourier transform allows for the conversion

of a signal from the time domain to the frequency domain by application of a complex exponential transform. For a continuous signal, the Fourier transform is defined as:

$$X(f) = \int_{-\infty}^{+\infty} x(t)exp(-i2\pi ft)dt \tag{2.16}$$

The problem with the above transform is that all signals of practical use are discrete signals of finite length. This is where the discrete Fourier transform is useful and is defined as:

$$F_k = \frac{1}{N}\sum_{n=0}^{N-1}\left(x_n exp\left(-i\frac{2\pi}{N}nk\right)\right), k = 0, 1, ..., N-1 \tag{2.17}$$

where $N$ is an even number of time domain samples, $n$ is the time domain sample index, and $k$ is the frequency domain index. Once the signal has been converted to the frequency spectrum it can then be manipulated to extract the power spectral density (PSD).

The instantaneous power of a signal, $x(t)$, is defined as $|x(t)|^2$, or in other words, it's mean square value. When examined in the frequency spectrum, the power spectral density is equivalent to the mean square values of the signal's frequency bands where PSD for discrete signals is defined as:

$$PSD_k = \left[\frac{F_k F_k^*}{\Delta f}\right], k = 0 \tag{2.18}$$

$$PSD_k = \frac{1}{2}\left[\frac{F_k F_k^*}{\Delta f}\right], k = 1, ..., \frac{N}{2} - 1 \tag{2.19}$$

where $F_k$ is the Fourier coefficient normalized such that it is an amplitude as is defined in Eq. 2.17. The 1/2 factor stems from the fact that the mean square of a sine wave is equal to half its peak value. The $k = 0$ equation does not require this conversion as its mean square value is equal to the peak value for a signal with zero frequency and such a signal is known as a DC signal. Finally, each PSD coefficient is evaluated over the frequency band $1/\Delta f$ since PSD is a description of the variation of a signal's power versus frequency and thus is integrated over that band, $df$. [27]

*2.5.1 Sound Pressure Level.* Sound pressure level (SPL) is a logarithmic measure of pressure fluctuations relative to a reference pressure and is measured in decibels (dB) above the reference value. The standard reference sound pressure in air is 20 $\mu Pa$, which is commonly accepted as the threshold of human hearing. [27]

$$SPL = 10log\left(\frac{{p_{rms}}^2}{p_{ref}^2}\right) = 20log\left(\frac{p_{rms}}{p_{ref}}\right) \tag{2.20}$$

*2.5.2 Multi-Windowing Method.* Due to the fact that a sample must be restricted to a finite time interval and the method of breaking down the signal into an orthogonal trigonometric basis set over this interval, the problem of spectral leakage presents itself. Over all possible frequencies, only those which coincide with the basis will project onto a single basis vector whereas all other frequencies will display nonzero projections onto the entire basis set. Ultimately, this means that frequencies other than those of the basis set will present themselves when in reality they are not present in the sample. Therefore, spectral leakage is a result of processing finite-duration records leading to discontinuities at the boundaries of the observation that are responsible for artificial spectral contributions over the entire basis set. [28]

A window is a weighting function that can be applied to a data set in order to reduce the spectral leakage associated with finite observation intervals. Windows are applied to the basis set so that the overwhelming projection will occur only on those basis vectors with a signal close to that of the signal frequency. Since the error inherent in the spectral analysis occurs at the boundaries of the sample, then windows are typically applied to partitioned overlapping data of 50 to 75 percent overlap. In order to apply this method the sample partitions must be statistically stationary with respect to one another. [27, 28]

One of the more popular windows is the Hamming window, which is a raised-cosine window designed to achieve minimum sidelobe levels. The window is defined

as:

$$w(n) = \left\{ \begin{array}{l} 0.54 + 0.46cos\left[\frac{2\pi}{N}n\right], n = -\frac{N}{2}, ..., -1, 0, 1, ..., \frac{N}{2} \\ 0.54 - 0.46cos\left[\frac{2\pi}{N}n\right], n = 0, 1, 2, ...N - 1 \end{array} \right] \tag{2.21}$$

A Hamming window is shown in Figure 2.6 in both the time and frequency domain for a symmetric 64 point sample.

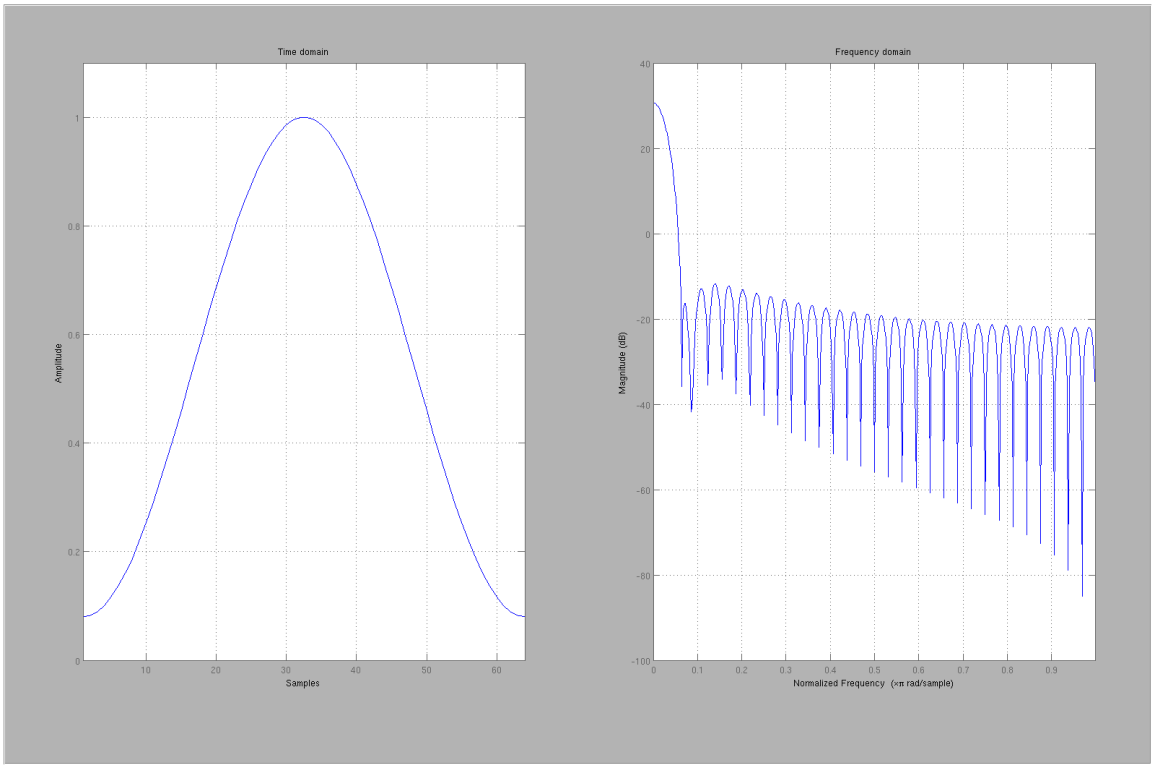


Figure 2.6: 64-point Hamming window

An application of this method is proposed by Welch, using a Fourier transform on segmented windows in order to calculate power spectral density. Welch's method involves dividing the record into overlapping sections, calculating modified periodograms of each section, and them averaging these modified periodograms. This method is meant to be more computationally efficient than other approaches. A modified periodogram is calculated by applying a data window to each section and then taking the finite Fourier transform of each windowed section. The estimate of power spectra is the average of these modified periodograms. [29]

## *2.6 Flight Testing*

Flight testing has been performed with both the Rivet Joint and Combat Sent variants with a primary objective of evaluating vibration response of the upper fuselage antennas. Specifically, this flight testing focused on the similarly placed UHF3, UHF5, and UHF7 Unilink antennas as shown in Figure 2.7. Figure 2.8 shows the locations of the accelerometers and microphones for all of the flight tests.

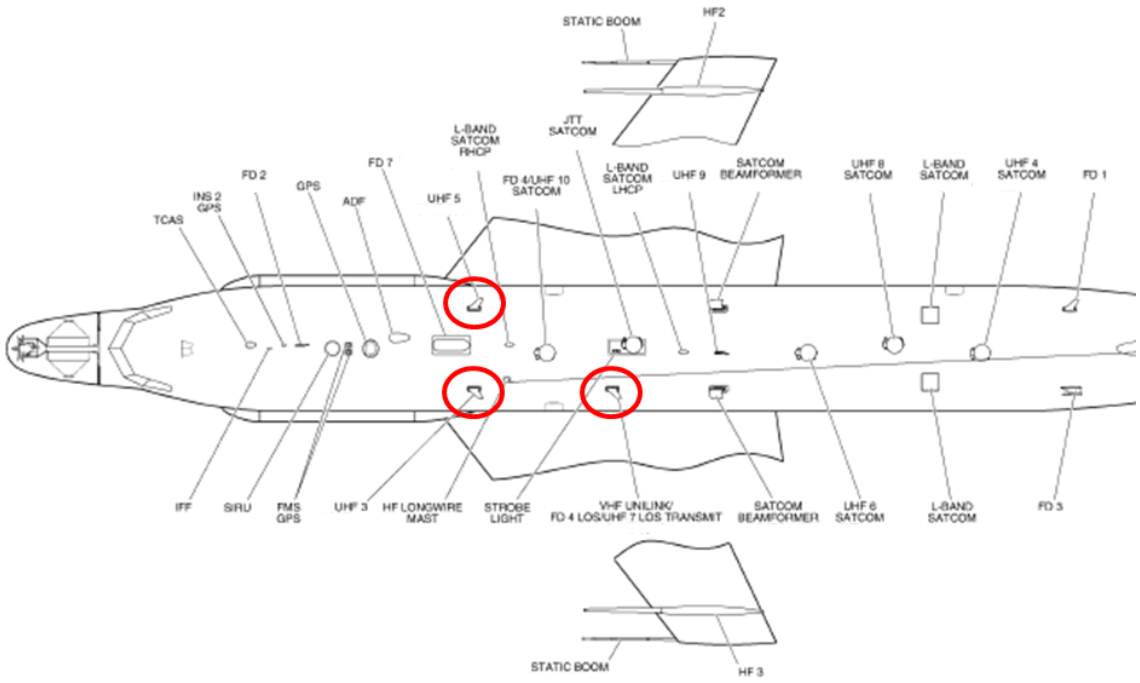


Figure 2.7: RC-135V/W BL9 antenna locations along the top of the fuselage with UHF3, UHF5, and UHF7 Unilink shown circled in red

The flight testing of the Combat Sent variant examined the effects of having the louver installed over the exhaust duct of the LCS. The louver was shown installed on the Combat Sent in Figure 1.4 of Chapter I. Tests were conducted with and without the louver, as well as with the exhaust capped. The vibration response of the UHF3, UHF5, and UHF7 Unilink antennas are similar between the two variants with the louver on. With louvers installed, the peak response of the UHF3 and UHF5 antennas ranged from approximately 3g to a maximum response approaching 15g, while the Unilink antenna ranged from 9g to in excess of 22g. To put this in

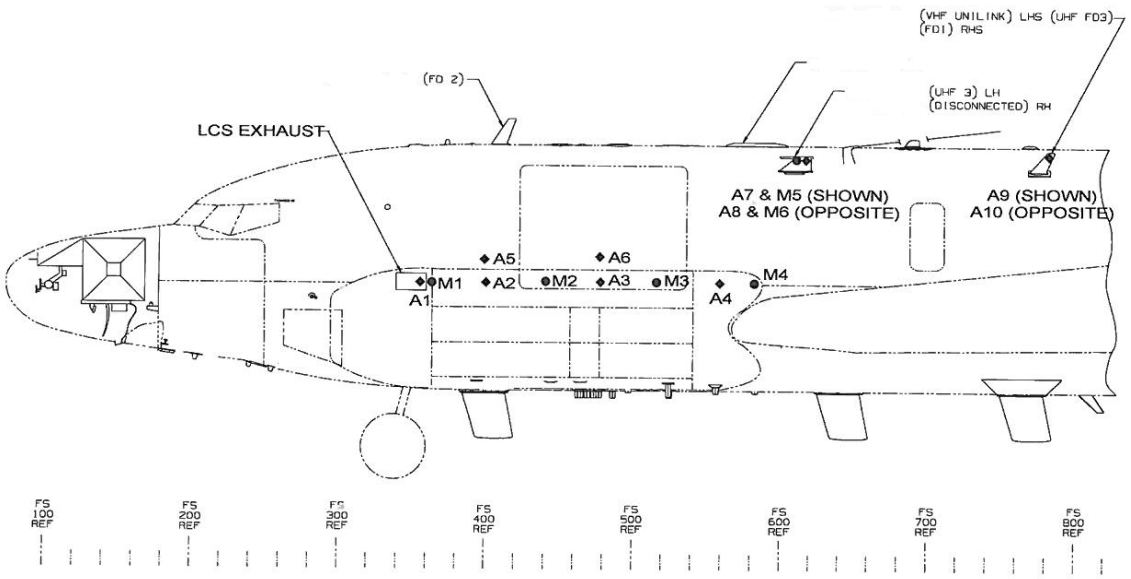


Figure 2.8: RC-135V/W accelerometer and microphone locations for flight testing

perspective, the manufacturer specified vibration limit for the Sensor Systems, Inc. S65-8262-305 antenna is 10g. With louvers removed, the peak responses did drop to a range of approximately 3g to a little over 6g for the UHF3 and UHF5 antennas and a range of 3.6g to 12g for the Unilink antennas. [7]

The flight tests demonstrated that the antenna response is sensitive to angle of attack, measured as the long flight durations allowed for a significant variation in airplane gross weight. Thus the higher peak responses correspond to higher gross weights and thus higher angles of attack. Figure 2.9 shows the maximum vibration response of the UHF3, UHF5, and Unilink antennas for a flight condition of 26,000 ft and 345 KIAS with the louvers installed on the Rivet Joint. [7]

In order to determine if the results were sensitive to the material of the antenna itself, UHF5 was replaced with a mast of higher natural frequency than the original S65-8262-305 antenna. The maximum vibration response of the two antennas is shown in Figure 2.10 demonstrating not only that using a stiffer antenna reduces the peak vibrational response but that the antennas will vibrate at the natural frequencies of the material. [7]

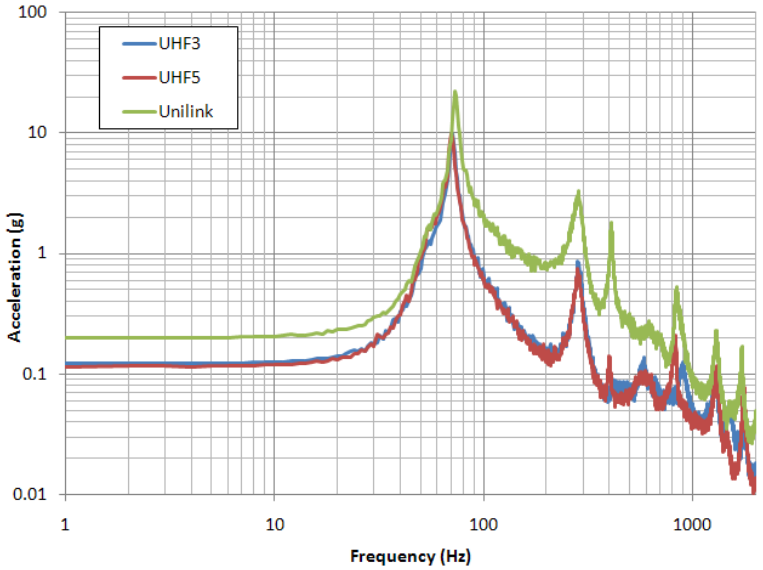


Figure 2.9: Rivet Joint antennas response - louvers installed [7]

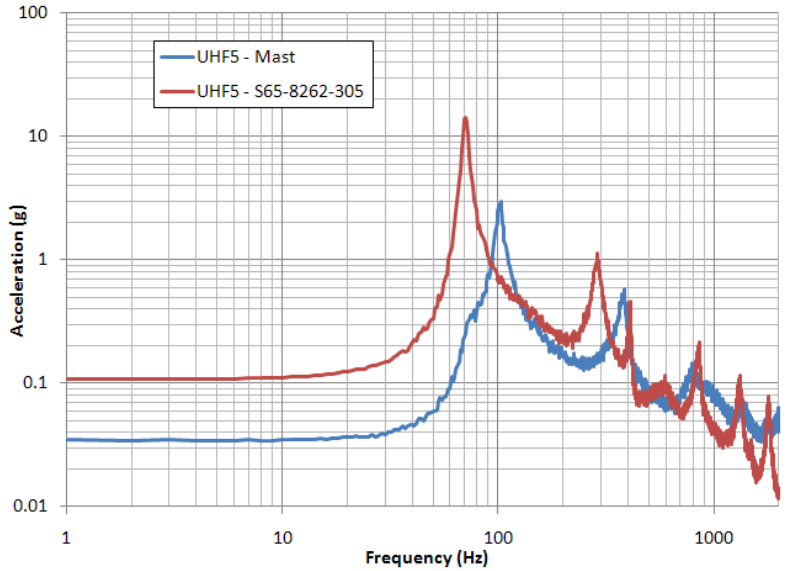


Figure 2.10: UHF5 mast response [7]

In order to find a good correlation to flow conditions that could induce antenna buffeting, the aircraft was also instrumented with microphones in various locations. Elevated sound pressure levels correspond to higher pressure fluctuations and thus the possibility of antenna buffeting. Figure 2.11 shows an example of the acoustic spectrum along the cheeks aft of the LCS exhaust. This corresponds to the Rivet Joint with no louver installed on the left cheek at Mach 0.67 and 29,000 feet and an angle of attack of approximately 2.5 degrees (199,300 lb gross weight). The primary frequency is in the range of 60 to 70 Hz and note that the sound pressure level drops with longitudinal distance from the LCS exhaust. [7]

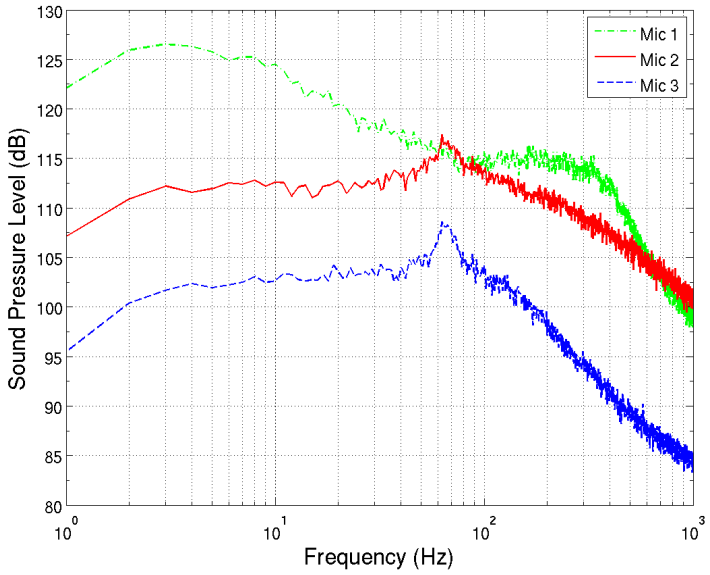


Figure 2.11: RC-135V/W acoustic response along the cheeks [7]

Due to a continuation of problems with the Rivet Joint, additional testing was performed with the UHF3 antenna removed in order to attempt to capture the noise environment at the location of this antenna without it affecting the flow. Figure 2.12 shows the acoustic spectrum at the LCS exhaust outlet. The dominant frequency at the LCS exhaust was determined to be in the range of 40-45 Hz at this location. At the location of the UHF antenna, the dominant frequency captured was in the range of 65-70 Hz as shown in Figure 2.13. The antenna response from an earlier flight test

is overlaid to demonstrate the correlation between the acoustic levels and vibrational response.

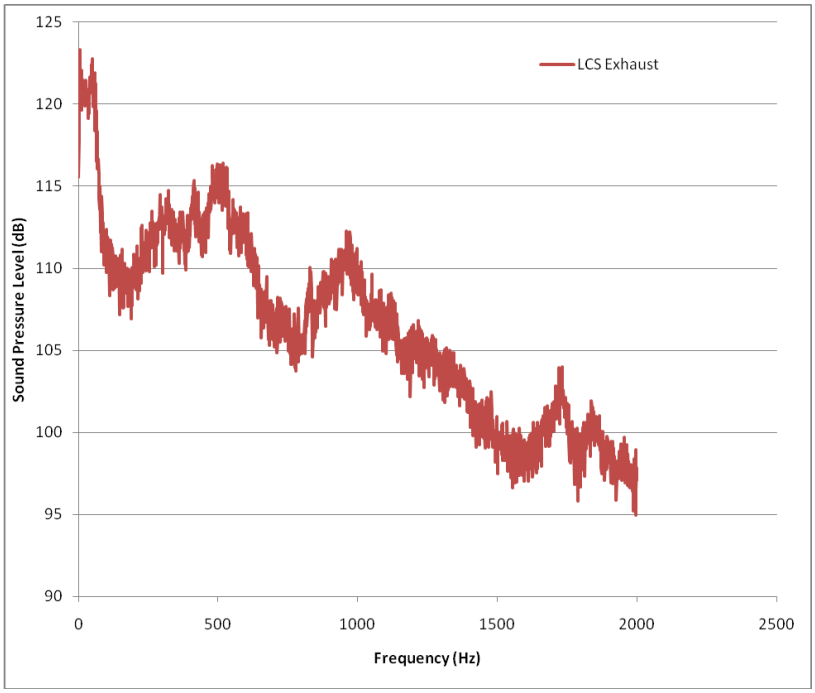


Figure 2.12: RC-135V/W exhaust noise with louvers removed [8]

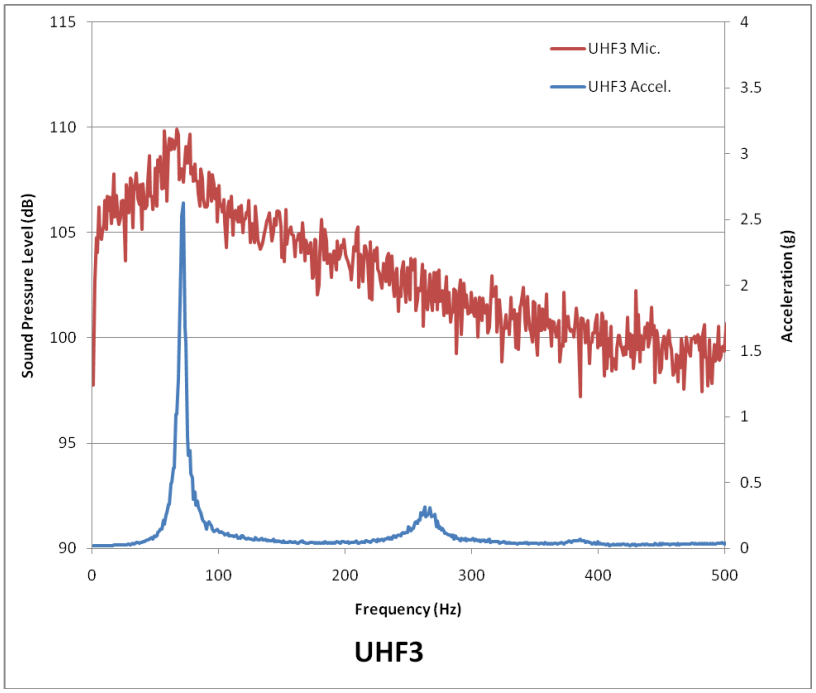


Figure 2.13: RC-135V/W noise environment at the UHF3 position with both antenna and louver removed [8]

# III. Methodology

CFD analysis is performed using the Kestrel v2.1.2 solver in order to characterize the differences in external fuselage aerodynamics between the Rivet Joint and Combat Sent variants of the RC-135 family of aircraft. The baseline case is chosen to be Mach 0.76 at an altitude of 30,000 feet and an angle of attack of four degrees in order to simulate a typical maximum range cruise scenario. The configuration of each aircraft is modified such that flow through the LCS is simulated or not and the antennas along the top of the fuselage are included or not. Two angles of attack are compared and three additional LCS mass flow rates are simulated and compared against the set of baseline cases. In addition, a time step and grid refinement sensitivity study is performed for verification and the Rivet Joint is compared against flight test data for validation.

Simulations are to be run on the AFRL DOD Supercomputing Resource Center's (DSRC) Raptor supercomputer. Raptor is a Cray XE6 with 2,732 compute nodes with two 2.4-GHz AMD Opteron 64-bit 8-core processors each. This results in a total of 43,712 computational cores available with each node having 30 GB of user-accessible shared memory. Each simulation will be run using 1,024 cores or 64 nodes. Raptor's peak performance is rated at 34.379 HABUs and 410.04 peak TFLOPS and as of November 2011 it was ranked as the 30th fastest computer in the world by Top500. [30, 31] A HABU is a HPCMP unit of measurement comparing solution time when running a standard application test case to that of the DOD standard system's baseline time for a targeted number of processor. The first DOD standard system is the Habu, which is an IBM Power3 formerly located at the US Naval Oceanographic Office (NAVO) Major Shared Resource Center. One HABU is the performance of 1,024 system processors compared to 1,024 Habu processors. [32] One TFLOP is equivalent to $10^{12}$ floating-point operations per second.

### *3.1 Grid Generation*

There are eight different aircraft configurations chosen to be compared as shown in Table 3.1. This means that eight grids must be constructed to represent each individual configuration. CAD models are provided by L-3 Communications via Big Safari which must be cleaned up and repaired before grid generation can begin. This is a typical issue with grid generation as varying precision with building models on different systems and formatting errors present in different software results in gaps between surfaces and even missing surfaces in the transferred model. A water-tight model is required before grid generation can be performed. This process can be

Table 3.1: RC-135 model configurations

| Configuration | Variant | Antennas | LCS |
|---|---|---|---|
| 1 | Rivet Joint | No | No |
| 2 | Rivet Joint | No | Yes |
| 3 | Rivet Joint | Yes | No |
| 4 | Rivet Joint | Yes | Yes |
| 5 | Combat Sent | No | No |
| 6 | Combat Sent | No | Yes |
| 7 | Combat Sent | Yes | No |
| 8 | Combat Sent | Yes | Yes |

quite difficult and time consuming. For example, the original CAD model did not represent the geometry of the Combat Sent "chin" radome accurately (Figure 3.1a). Representation of the cockpit is another issue that was addressed, wherein the angular geometry of the windscreen (Figure 3.1b) was smoothed over in the initial model. Part of the problem is that these aircraft were designed well before CAD was utilized by the industry and only recently are CAD models being built for these aircraft.

Currently, the existing models seem to have more of an emphasis on structural design and antenna placement as opposed to providing an accurate representation of the external skin geometry such as is needed for CFD analysis. L-3 Communications is currently working on building better CAD models for these aircraft along with improved antenna representation that should provide a better model for future research. In the mean time, the Rivet Joint model provided has the best representation

(a) (b)

Figure 3.1: Combat Sent forward fuselage geometry (a) "chin" radome (b) cockpit

of the geometry so it was chosen as the baseline model to work from. The engines were removed along with all antennas except for those along the upper fuselage. The antenna configuration is representative of that on the Baseline 9 version of the Rivet Joint.

For the Combat Sent, a model of the forward fuselage was provided by L3 Communications that represents the radome geometry with a reasonable amount of accuracy although some modifications are desired before extensive analysis on the lower fuselage aft of the "chin" should be undertaken. This forward fuselage was then mated with the existing Rivet Joint model in order to produce the Combat Sent model. All of this manipulation was performed within ANSYS ICEM CFD in preparation for grid generation.

With the geometry cleaned up the grid generation process can begin. The following methodology was followed for all grids created:

1. Compute volume and surface mesh using the Octree method in order to provide a good quality patch independent surface mesh.
2. Delete volume mesh and smooth surface mesh with alternating Laplace method on/off (10 on, 10 off, 10 on, 10 off).
3. Recompute volume mesh using the Delaunay advancing front method.

4. Compute prism cells for the boundary layer.

Between each major step the grid is checked for errors and smoothed in preparation for the next step. The Octree method is a "top-down" approach, wherein a "root" tetrahedron is created over the entire domain and subdivided until it matches all grid spacing requirements. The Delaunay advancing front method is a "bottom-up" approach that works from an existing surface mesh and gradually grows the tetrahedral mesh out from this boundary, providing a smoother transition into the volume than the Octree method. [33]

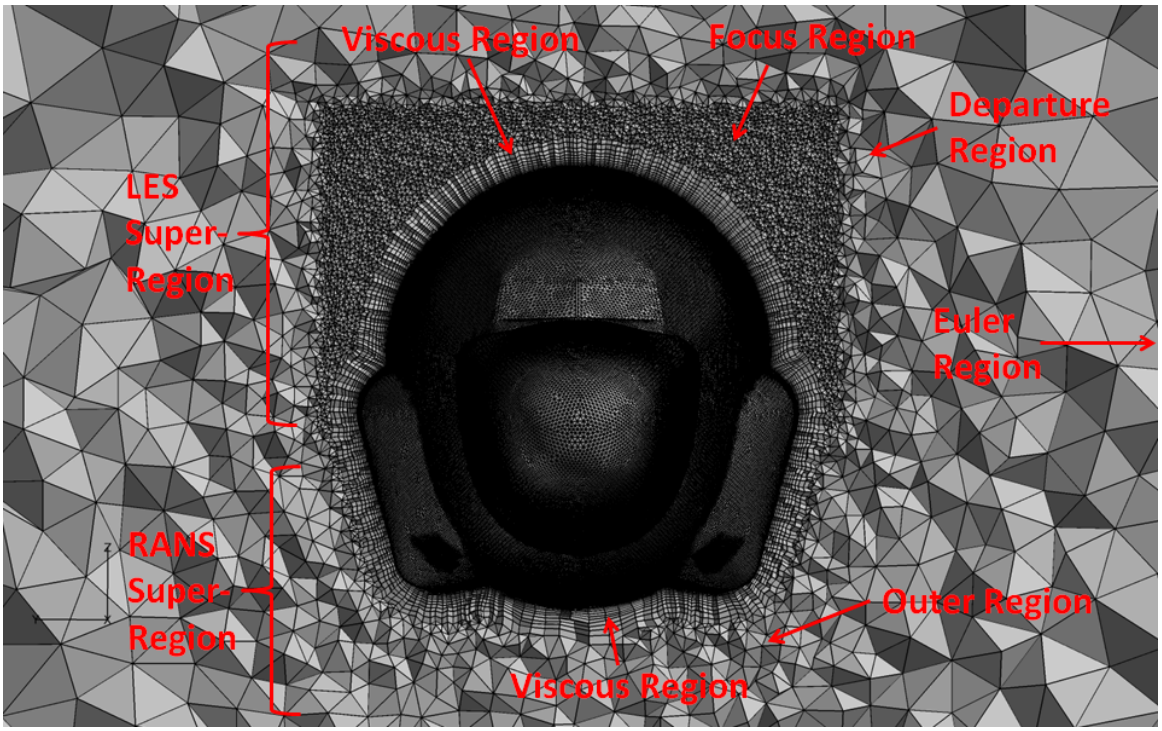


Figure 3.2: Frontal view of the spatial discretization for the Rivet Joint with LCS highlighting the different regions of the grid

When creating a grid for the application of DDES, there are three regions that must be accounted for and modeled independently including the Euler Region (ER), RANS Region (RR), and LES Region (LR). These regions are considered "super-regions" and are further broken down into the viscous (VR) and outer (OR) regions for the RR and the viscous (VR), focus (FR), and departure (DR) regions for the LR. The same equations will be applied to all regions while necessitating different approaches

to grid generation. The different regions as they apply to the grids generated for this study are shown in Figure 3.2. [34]

The ER contains the majority of the control volume extending upstream and to the sides of the geometry. The grid cells should exhibit fairly isotropic spacing in all directions and contain large cells extending out to the far field, thus making up the smallest number of cells. [34] The AIAA Drag Prediction Workshop guidelines call for the outer boundary to be at least 100 reference chord lengths away from the body in all directions so as to minimize the effect the far field will have on the aircraft. This does not necessarily add many cells to the domain as the spacing is so large in this region. [6]

The VR is the region within the RANS super-region wherein the standard viscous sublayer, buffer layer, and log layer are modeled. The grid generation methodology is the same as would be for a typical RANS application wherein the initial grid spacing should be at an average $y^+ = 2$ or less for an S-A model in order to accurately capture the viscous sublayer and with a growth ratio of $\Delta y_{j+1}/\Delta y_j = 1.25$ or less in order to accurately model the log layer. Ultimately, an average $y^+ = 1$ and $\Delta y_{j+1}/\Delta y_j = 1.2$ is desired as little is gained by lowering these parameters further. In the wall-parallel direction the grid spacing is dictated by the geometrical requirements more than actual flow considerations and is typically much larger than the wall normal spacing. The required initial wall normal spacing can be estimated by [35]:

$$\Delta = L\frac{(13.1463y^+_{ave})^{0.875}}{Re_L^{0.90}} \tag{3.1}$$

Thus, for this study the grid is originally generated for the baseline case at Mach 0.76 and 35,000 feet ($Re_L = 3.65 \times 10^7$) resulting in an estimated initial spacing of $\Delta = 3.59 \times 10^{-4}$ inches. The boundary layer thickness can also be estimated using Prandtl's power-law formula for a flat plate turbulent boundary layer [15]:

$$\delta = \frac{0.37L}{Re_L^{1/5}} \tag{3.2}$$

resulting in an estimated boundary layer thickness of $\delta = 2.74$ inches. This value is only an initial guess at the thickness and will obviously vary depending on location on the geometry and since separation is expected for this flow field the boundary layer is expected to be much thicker in certain areas. This is important when examining the outer layers of the viscous region as this is where the solver will switch between DES and RANS with each respective application having different grid requirements.

In practice, it is better to over-estimate the boundary layer thickness and often the OR will extend into the ER and thus a total of 49 prism layers is chosen. The total prism layer height based on an exponential growth rate can be calculated from [33]:

$$H_n = \Delta \frac{(1 - (\Delta y_{j+1}/\Delta y_j)^n)}{(1 - (\Delta y_{j+1}/\Delta y_j))} \tag{3.3}$$

where $n$ is the number of layers resulting in a total prism layer thickness of $H_{49} = 13.57$ inches. [34]

The LES super-region is the portion of the domain wherein the vorticity and turbulence is desired to be captured using DES. The VR in this region has the same requirements as the VR of the RR wherein the boundary layer will still be modeled using a RANS model. The FR is the region close to the body wherein the turbulence inherent to the flow must be well resolved. In this region, a target grid spacing $\Delta_0$ is chosen as the primary measure of spatial resolution. The DR is more of a transition region wherein the grid spacing will blend into the ER and will far exceed $\Delta_0$. In this case, the FR is chosen to encompass the forward fuselage including the nose region and LCS inlet/outlet as well as the entire upper fuselage extending back to the leading edge root of the vertical tail. In this region a grid spacing of $\Delta_0 = 2$ inches is chosen such that it is refined enough to capture the largest turbulent scales without overburdening the DSRC computers. The FR is created using two density boxes extending from the nose of each aircraft to $X = 317$ inches, $Y = +/-100$ inches in the lateral direction off of the longitudinal axis, and $Z = -100$ to $Z = 125$ inches in the vertical direction whereas the second box extends along the upper fuselage above

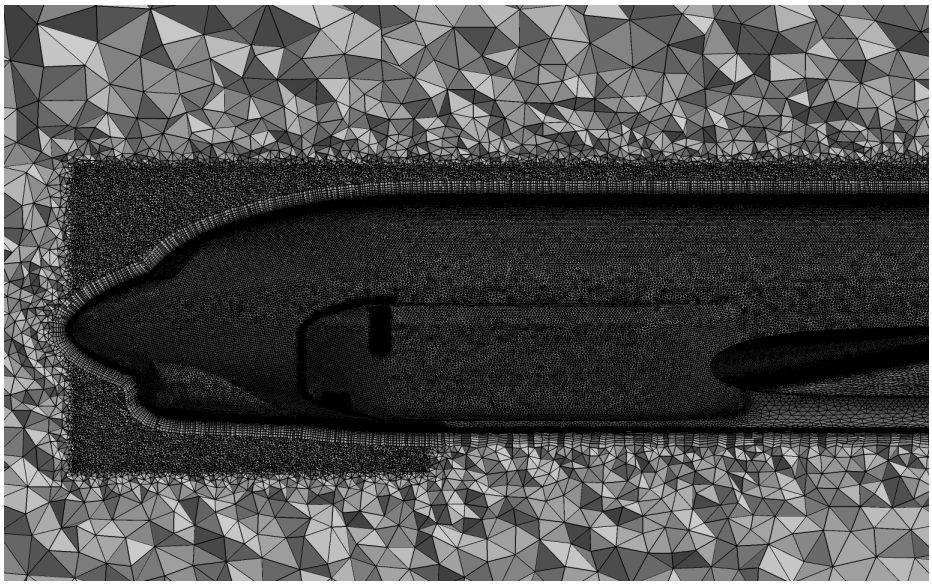

Figure 3.3: Side views of spatial discretization of the Combat Sent forward fuselage

the longitudinal axis back to $X = 1269.15$ inches. This is shown in Figure 3.3. It is important that this region encompasses both the region where data collection will take place as well as any possible sources of turbulent flow ensuring that the FR is continuous between the nose and LCS exhaust to where the antennas are located. [34]

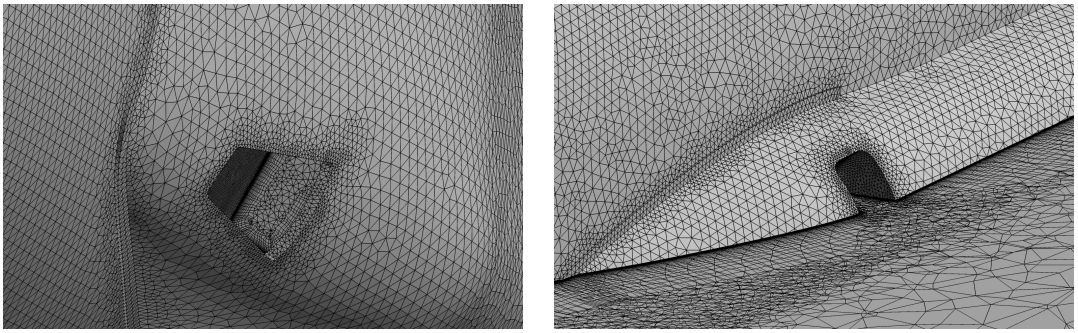

(a) (b)

Figure 3.4: Spatial discretization of the LCS (a) inlet (b) exhaust

Flow through the LCS is modeled using a mass flow rate source and sink boundary condition on surfaces placed internal to the ducting. It is difficult to accurately model the flow through the LCS as there is a radiator in the middle of the duct

through which air flows over in flight. Since the radiator itself is difficult to model, allowing flow to go straight through the ducting may not be the most accurate method of modeling this flow. Thus, for this study the flow is modeled by sinking surfaces below the fairing surface within the ducting and setting a mass flow rate perpendicular to this surface. For stability, the initial few wall cell layers around the exhaust are set to slip wall and then switched to no slip through the remainder of the ducting. The viscous region is also smaller in the ducting so to avoid collision problems with the prism extrusion in ICEM CFD, therefore only 38 layers are extruded at a total height of $H_{38} = 1.83$ inches. Discretization of these features is shown in Figure 3.4.

The maximum surface spacing in the FR is set to two inches which is also the spacing for the wing and empennage root, tip, leading and trailing edges. This spacing extends along the cheek fairings but is refined to 1" along the leading edge of the cheeks in order to capture the fairing fasteners as well as for the walls of the LCS ducting. A coarser spacing of 8" is used along the wing, empennage, and lower fuselage surfaces as well as any other remaining surface regions outside of the FR.

### *3.2 Solver Settings*

The Navier-Stokes equations are applied with second order accuracy in both space and time. The DDES turbulence model is utilized along with a global specified time step in order to accurately capture the inherent unsteadiness in the flow. The time step is set to $\Delta t = 2.0 \times 10^{-4}$ seconds ($\Delta t^* = 0.007516$) as this allows for adequate solver stability and is refined enough to capture the flow features of interest at the current level of spatial discretization as will be discussed in Section 3.4. Four Newton subiterations are applied for all cases and an effort is made to minimize the temporal damping coefficients approaching an advective damping of 0.3 and a diffusive damping of 1/10 of this value at all times. Stability is very much an issue with these simulations and great effort is taken to arrive at a statistically stationary point void of all transients before initiating data collection runs. The methodology for running all of the cases is similar and obeys the following procedure:

1. Minimum of 4000 startup iterations including at least 1000 iterations of CFL and boundary condition ramping (NS with S-A and local time stepping)
2. Switch to NS with DDES and global specified time step with same temporal damping
3. Reduce temporal damping and repeat Step 2 until temporal damping of 0.3 is achieved
4. Perform data collection (1.8 seconds or 9000 iterations)

The time period of 1.8 seconds is chosen such that three samples of 0.9 seconds each with a 50% overlap is collected. This is selected such that spectral analysis can be performed utilizing Welch's method along with a Hamming window. By the Nyquist sampling rate, the minimum frequency that this sampling period allows to be captured is approximately 2.2 Hz while the time step limits the maximum frequency to 2500 Hz. This allows for 45 cycles of 50 Hz and 90 cycles of 100 Hz which should be more than enough to capture the frequencies of interest to this study. The only guidance is that which has been demonstrated by flight testing suggesting that the frequency band of interest is well inside of the spectrum captured using this methodology.

Boundary conditions for all solid wall boundaries are set to Adiabatic No Slip. The far-field is modeled using a Modified-Riemann-Invariants boundary condition. The LCS inlet and outlet are modeled using specified mass flow rate Sink and Source boundary conditions. The Source boundary condition requires that total pressure and temperature be specified and are set equivalent to free-stream conditions. This is obviously not the case, but there is no available data to justify different settings and is not expected to have a significant effect on the flow. Additionally, directionality must be specified for each outlet and is set to be the normal unit vector to the boundary face and to address stability concerns, the first couple inches of solid wall encountered around the outlet are specified as Slip boundary conditions.

### *3.3 Tap Locations*

Time accurate pressure data is recorded at 294 locations along the upper fuselage and upper cheeks as summarized in Table 3.2. Every antenna location on the upper fuselage is accounted for in the time pressure histories. Tap placement on a typical "blade" antenna is shown in Figure 3.5. Three rows of three taps are place on each

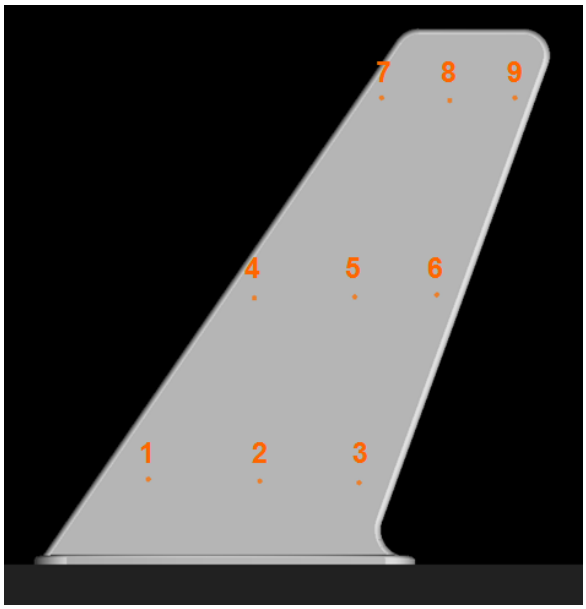


Figure 3.5: Placement of taps on a typical "blade" antenna

side with the numbering convention increasing from leading to trailing edge and root to tip resulting in a total of 18 taps on each blade antenna. The SATCOM antennas followed a similar methodology with the addition of extra taps along the horizontal dish. Taps 288-291 are set such that they are close to the locations of microphones 1-4 from flight testing as shown in Figure 2.8. The additional taps are placed along the fuselage above the cheek. This is shown in Figure 3.6.

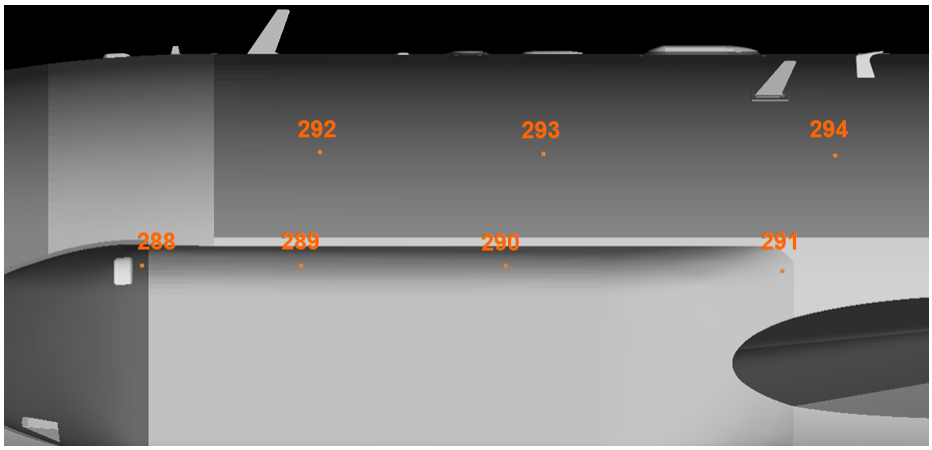


Figure 3.6: Placement of taps on the cheeks and fuselage

Table 3.2: Tap locations

| **Antenna** | **Taps** | **Antenna** | **Taps** |
|---|---|---|---|
| VHF/UHF FD2 | 1-17 | TCAS | 273 |
| UHF3/FD3 | 19-36 | IFF | 274-275 |
| UHF5 | 37-54 | INS2 GPS | 276 |
| VHF UNILINK and FD4/UHF7 | 55-72 | FMS GPS | 277-278 |
| UHF9 | 73-90 | GPS | 279 |
| FD1 | 91-108 | ADF | 280-281 |
| FD3 Unit 3323 | 109-126 | FD7 | 282-283 |
| FD4/UHF10 SATCOM | 127-153 | L-Band SATCOM Unit 5567 | 284 |
| JTT SATCOM | 154-180 | L-Band SATCOM Unit 5559 | 285 |
| UHF6 SATCOM | 181-207 | Unit 8874 | 286 |
| UHF8 SATCOM | 208-234 | Unit 8872 | 287 |
| SATCOM BF Unit 7421 | 235-253 | Cheeks/Fuselage | 288-294 |
| SATCOM BF Unit 7424 | 254-272 | | |

### *3.4 Grid Resolution and Time Step Sensitivity Study*

When modeling complex flows with large regions of separated unsteady flow, it is difficult to find the combination of settings that will produce an adequate answer and further to verify that the results are accurate and reliable is quite challenging. Since unsteady DDES is being used to model this flow field the traditional approaches, such as performing a grid independence study, do not necessarily apply. Due to the nature of DDES, as discussed in Section 2.2, as the grid is refined smaller length scales are continuously being resolved and the fundamental nature of the solution is changing. This applies equally to the chosen time step as smaller time steps will just lead to smaller turbulent temporal scales being resolved. In order to adequately model time dependent flows, an understanding of the physical nature of the flow of interest is key. One must choose the features of interest and converge on some parameter describing that flow feature.

The general "rule of thumb" is that "the time step should be determined by the temporal aspects of the flow feature(s) of interest in the computation." [9] Therefore, by applying the Nyquist rule, the sampling rate should be at least twice that of the frequency of interest. So the question becomes, what is the frequency of interest? Since there is no real precedent for this particular flow scenario, the flow exiting the LCS can best be likened to the vortical flow over delta wings. This type of flow is characterized by helical mode instabilities, shear layer instabilities, vortex shedding and breakdown as shown in Figure 3.7. The flow field of interest to this study may not

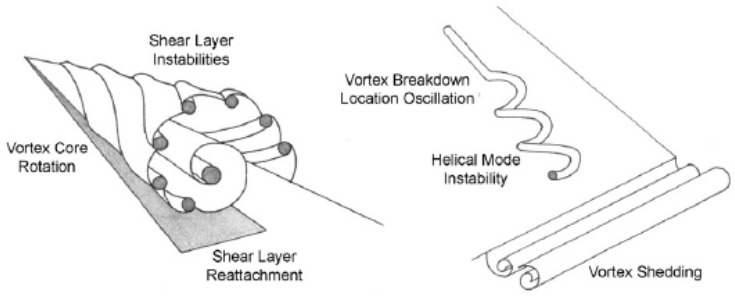


Figure 3.7: Types of unsteadiness in delta wing flow [9]

necessarily have the same well defined vortex cores or helical mode instabilities but it will certainly exhibit the same features inherent to shear layer instabilities wherein Strouhal numbers ($St \equiv fl/U_\infty$) approaching twenty could be expected. This does not necessarily mean that the shear layer instabilities are the primary flow feature of interest but previous research by Cumming et al. has shown that the lower Strouhal number features are often dependent upon the higher frequency features and thus must be modeled. A non-dimensional time step $\Delta t^* = \Delta t U_\infty / l$ is introduced to provide some physical guidance on the choice of time step that when rearranged in terms of Strouhal number using the Nyquist sampling rate becomes $\Delta t^* = 1/(2St)$. This suggests that a non-dimensional time step of $\Delta t^* = 0.025$ is necessary. In general, Cumming et al. have found that picking a non-dimensional time step $\Delta t^* \leq 0.01$ is a good starting point for unsteady flows of this nature. [9]

In order to provide verification of the choice of time step and grid refinement level, a joint grid resolution and time step sensitivity study should be performed. Three levels of grid refinement are utilized for this study (coarse, medium, fine) with the grid spacing altered by a factor of $\sqrt{2}$ in all directions in the focus region. The CS in a clean configuration with LCS for the baseline case is chosen to perform the comparison with 32.286M, 44.066M, and 118.019M cell grids. The fine grid is pushing the limits of the available computational resources and will be used for error predictions alone. [9]

Ideally, a time step study would be performed on each grid in order to see the combined impact that time step and grid refinement has on the results but this can be rather computationally expensive. Therefore, a "steepest descent" method is applied wherein six different time steps are applied across the three levels of refinement. With this method, each grid will be run with two time steps wherein decreasing time step is coupled with higher levels of refinement. The time-steps are chosen such that they vary by a factor of two from the starting value. This results in a minimum of six points wherein points 1 and 2 are the largest time steps run on the coarse grid, with points 3 and 4 corresponding to decreasing time steps on the medium grid and

points 5 and 6 representing the smallest time steps on the fine grid as demonstrated in Table 3.3. Since capturing the unsteady nature of the flow around the fuselage is the primary focus of this study, spectral analysis is performed in order to provide comparison between the different cases. The dominant frequency at a chosen tap location is extracted and compared for convergence. [9]

Table 3.3: "Steepest descent" methodology for the grid resolution and time step sensitivity study

| | **Time Step (seconds)** | | | | | |
|---|---|---|---|---|---|---|
| **Grid** | $1.6 \times 10^{-3}$ | $8.0 \times 10^{-4}$ | $4.0 \times 10^{-4}$ | $2.0 \times 10^{-4}$ | $1.0 \times 10^{-4}$ | $5.0 \times 10^{-5}$ |
| Coarse | P1 | P2 | P3C | P4C | P5C | P6C |
| Medium | P1M | P2M | P3 | P4 | P5M | P6M |
| Fine | P1F | P2F | P3F | P4F | P5 | P6 |

### *3.5 Comparison to Flight Test*

Flight test data was provided by L3 Communications out of Greenville, TX courtesy of Big Safari as discussed in Section 2.6. Vibrations data was provided for both the Rivet Joint and Combat Sent, but short of running aero-elastic simulations, it is difficult to compare to this type of data. Acoustics data is provided for the Rivet Joint that provides a possible avenue of validation for this model. The flight test condition chosen to compare against is set using an atmospheric static pressure of 4.59 atm, static temperature of $-33.8°$F, and Mach 0.67 which is equivalent to approximately 28,900 ft. The aircraft gross weight is approximately 199,300 lb resulting in an angle-of-attack of approximately 2.5°. The LCS mass flow rate for this flight test was determined to be 174.4 $lb_m/min$.

### *3.6 Baseline Comparison*

A baseline case is chosen to be consistent among all configurations that is representative of typical maximum range cruise conditions. Altitude is chosen to be 30,000 feet and the flight speed is chosen to be on the upper limits of the envelope set at

Mach 0.76. The angle of attack is dependent on the instantaneous weight of the aircraft and is chosen to represent a fairly full weight aircraft at $\alpha = 4°$. The mass flow rate of 190 $lb_m/min$ is determined by comparing the chosen conditions to flight test derived flow rates and providing an estimation of a reasonable rate consistent with both variants without any exhaust covering. All configurations are compared at these conditions and the results are used as comparison for the following studies.

### *3.7 Mass Flow Rate Sensitivity Study*

This study intends to examine the effects of altering LCS mass flow rates while keeping all other variables constant. This is accomplished utilizing all configurations that include the LCS and altering the specified mass flow rates for the appropriate boundary conditions. Three additional mass flow rates are compared to the baseline with low ($-15\%$ or 161.5 $lb_m/min$), high ($+30\%$ or 247 $lb_m/min$), and very high ($+84.2\%$ or 350 $lb_m/min$) cases.

### *3.8 Angle of Attack Sensitivity Study*

This study intends to isolate the effects of altering aircraft gross weight and therefore angle-of-attack while keeping all other variables constant. Simulations are performed with all configurations at a higher angle-of-attack of $\alpha = 8°$ simulating a banked turn at cruise conditions and again compared against the baseline.

# IV. Results

In order to examine the unsteady nature of the flow-field about the RC-135 family of aircraft, CFD simulations were run as discussed in Chapter III. Unfortunately, stability became a major concern with the four antenna configurations. For most cases, a temporal damping of 0.3 was achieved and thus was kept consistent between all cases in order to provide direct comparison. For the antenna configurations, stability could not be achieved even when lowering the CFL below 100 and raising the initial temporal damping to 1.0. The interval of CFL and boundary condition ramping was also altered, among other things, and stability was never achieved. Perhaps lowering the CFL below 1.0 would produce a stable solution, although this would increase the number of iterations required to remove transients in the flow, significantly increasing the computational expense of this study. In order to provide some comparison for these configurations, Euler solutions were computed for the baseline and high angle-of-attack cases without flow through the LCS. This was achieved using modified versions of the original grids after removing the viscous layers, as even the Euler equations would become unstable and diverge on the original grid. This seems to be a software deficiency and the problem tends to be very grid dependent, as will be discussed in Section 4.1. The CREATE-AV group is aware of the problem and it should not be as much of an issue in the next version.

## *4.1 Grid Resolution and Time Step Sensitivity Study*

Three levels of grid refinement and six different time steps were compared using the "steepest descent" method as discussed in Section 3.4. Stability was an issue with the coarse grid and thus lower time steps were not achievable with this grid although, surprisingly, they were achievable with the medium grid. Since the results from this one time step on the coarse grid demonstrate that there would be unacceptable error in the solution, further simulations on this grid were not pursued. Table 4.1 gives a summary of the cases completed for this study. Points 1-6 were the desired simulations to be run per the "steepest descent" method, but since there was so much trouble

Table 4.1: Summary of cases run for the grid resolution and time step sensitivity study with successful cases highlighted in green

| | **Time Step (seconds)** | | | | | |
|---|---|---|---|---|---|---|
| **Grid** | $1.6 \times 10^{-3}$ | $8.0 \times 10^{-4}$ | $4.0 \times 10^{-4}$ | $2.0 \times 10^{-4}$ | $1.0 \times 10^{-4}$ | $5.0 \times 10^{-5}$ |
| Coarse | P1 | P2 | P3C | P4C | P5C | P6C |
| Medium | P1M | P2M | P3 | P4 | P5M | P6M |
| Fine | P1F | P2F | P3F | P4F | P5 | P6 |

with the coarse and fine grids, only Point 3C and Point 5 were completed on these grids. Two additional time steps were then compared on the medium grid with Points 1M and 2M completed.

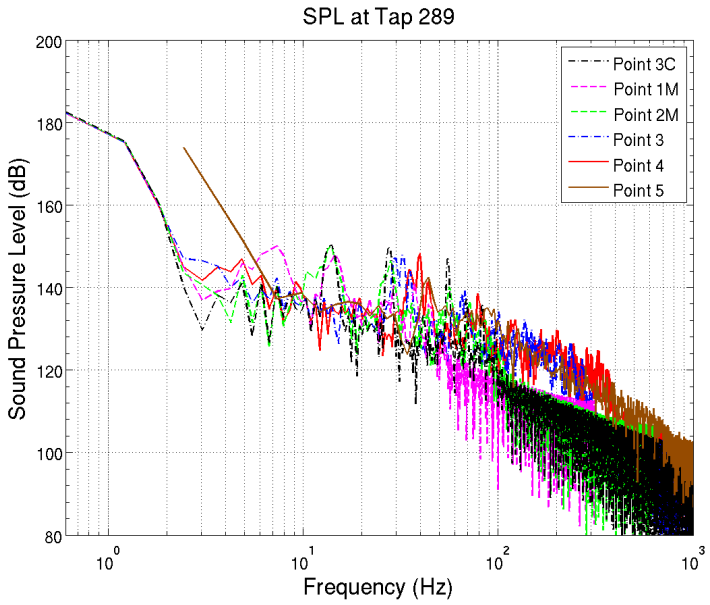


Figure 4.1: Combat Sent with LCS – acoustic spectrum extracted at Tap 289 for different grid refinement levels and time steps

The acoustic spectrum was calculated along the top of the cheek of the Combat Sent variant just aft of the cooling system exhaust (Tap 289) as shown in Figure 4.1. The dominant frequencies were then determined from this spectrum and converted to wave numbers in order to provide comparison between non-dimensional time steps as shown in Figure 4.2. The results shown in this figure demonstrate sufficient convergence with non-dimensional time steps less than approximately 0.01. This provides

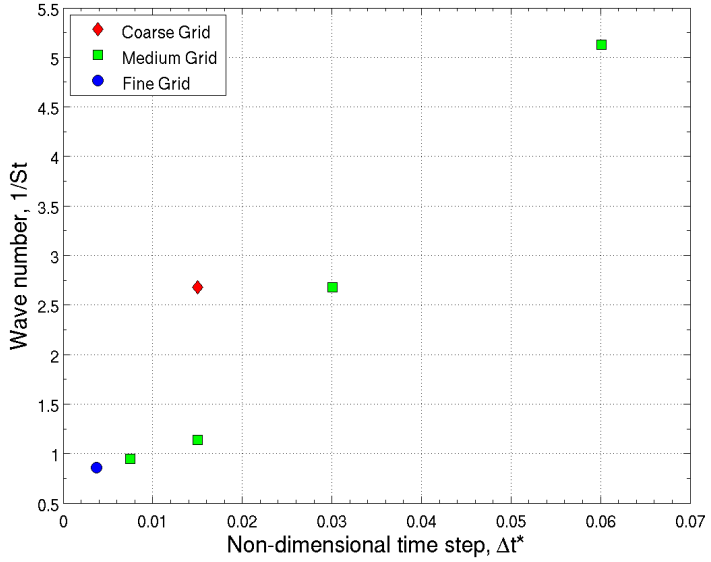


Figure 4.2: Combat Sent with LCS – dominant frequencies observed at Tap 289 for different grid refinement levels and time steps

justification for utilization of the chosen time step of $2.0 \times 10^{-4}$ seconds on the medium grid.

The computational expense of running on the medium grid is in the range of 50,000 to 100,000 CPU-hours in order to complete one simulation. The computational expense of completing one simulation on the fine grid (with a corresponding decrease in time step) approaches 500,000 CPU-hours. Average time per iteration increases from the range of 10-20 seconds per iteration to the range of 30-40 seconds per iteration. In addition, the memory requirements for the fine grid are such that twice as many processors must be requested (2,048 cores) than those actually being used by the solver (1,024 cores) due to memory limitations of the nodes on Raptor. These numbers suggest that it would be very difficult to meet the data collection goals of this investigation while using the fine grid.

Stability was a concern with all of the simulations run, but especially so with the coarse and fine grids. It would almost be expected on the coarse grid with the larger time steps, but even when the time step was decreased the same problems appeared. In most of the simulations run in the course of this research, the instabilities seemed

to manifest themselves in average $y^+$ values. Figure 4.3 provides an example of the experienced stability issues displaying $y^+$ and "NONLINP", which is a measure of the residual within Kestrel. Notice how the residual spikes periodically and how $y^+$

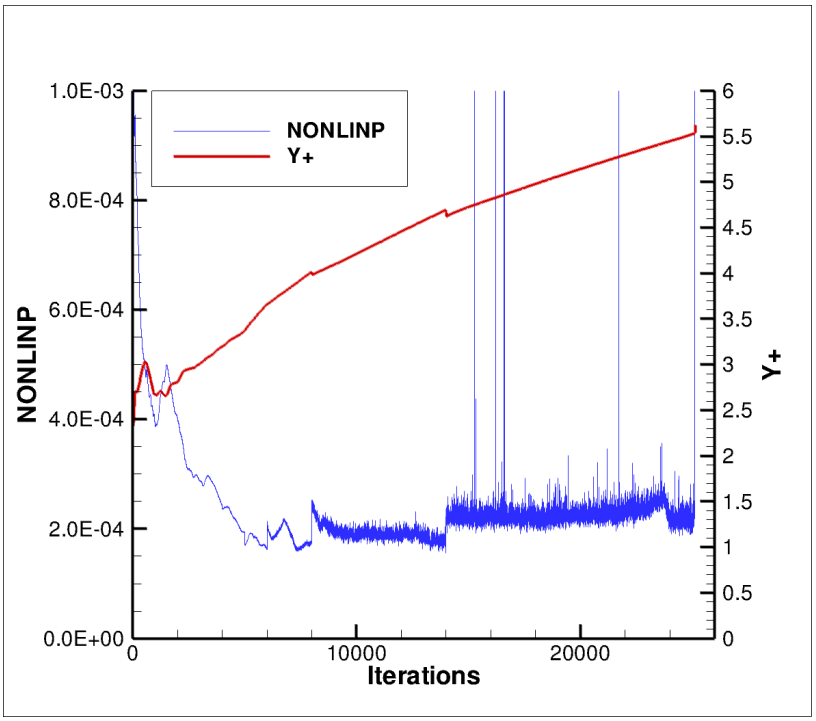


Figure 4.3: Examining Point 5 of the "steepest descent" method showing the residual and $y^+$ as a function of the number of iterations

continues to climb gradually. The "spikes" in the residual correspond to the limit on maximum number of sweeps being reached and is a definitive indication of an unstable solution. In this case, the solution diverged towards the end of the data collection window and thus still provided some usable data to compare to. Ideally, $y^+$ values of less than five are desired and, although some usable data was extracted, there would be some concern about accuracy if used for this investigation. The coarse grids displayed even larger values of $y^+$ on the order of $10^2$ which raises serious concerns about the accuracy of that data. This is curious, seeing as how the grids have the same viscous prism layers between all refinement levels. The only feature that changes is the surface grid spacing and the focus region spacing outside of the viscous region. Again, this problem seems to be very grid dependent and the instabilities encountered

with the coarse and fine grids is yet another reason why the medium grid should be used.

### *4.2 Comparison to Flight Test*

A comparison of computed data against flight test derived data was attempted. Unfortunately, due to software stability problems encountered, a solution for a configuration including antennas was never achieved, such as could better be compared against flight test. Euler solutions were computed for select antenna cases but since an acoustic comparison is warranted for validation, unsteady Navier-Stokes solutions are necessary and cannot be provided in this study. Despite this, some comparison can still be provided.

Acoustic spectral data is compared at locations along the top of the left cheek fairing aft of the LCS exhaust as shown in Figure 4.4. Comparing the acoustic spectrum, the dominant frequency of the simulation is not matched by the flight test data although the secondary frequency does coincide with the dominant frequency of the flight test as shown in Figure 4.5. The dominant frequency captured by the CFD simulation is 32.4 Hz with a secondary frequency of 64.7 Hz that is reasonably close the flight test derived dominant frequency of 63 Hz. As discussed in Section 2.6, flight tests were conducted on the Rivet Joint after removal of both the exhaust louvers and UHF3. This flight testing observed a shift in noise generated at the LCS exhaust of 40-45 Hz to 65-70 Hz at the location of UHF3. Unfortunately, this flight test data was not available in time to be able to run simulations at the corresponding flight conditions required for comparison, but it does suggest that the range of frequencies observed is reasonable.

Additionally, overall sound pressure levels (OASPL) can be compared at all of the relative microphone locations as shown in Figure 4.6. Note that the last microphone location corresponds to UHF3 and that antennas are not included in this computational model. With the antenna included in the flow and, furthermore, with the antenna exhibiting buffeting, sound pressure levels cannot be expected to match

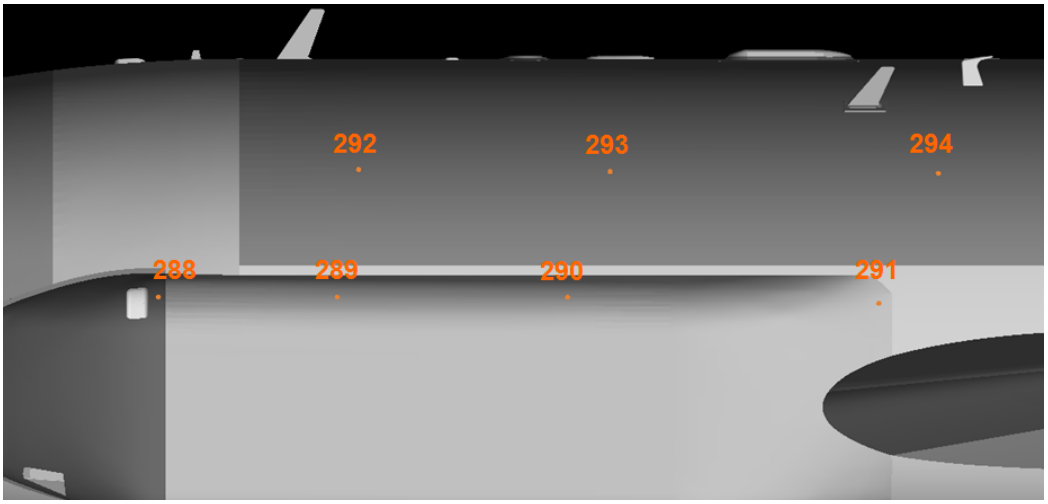


(a)

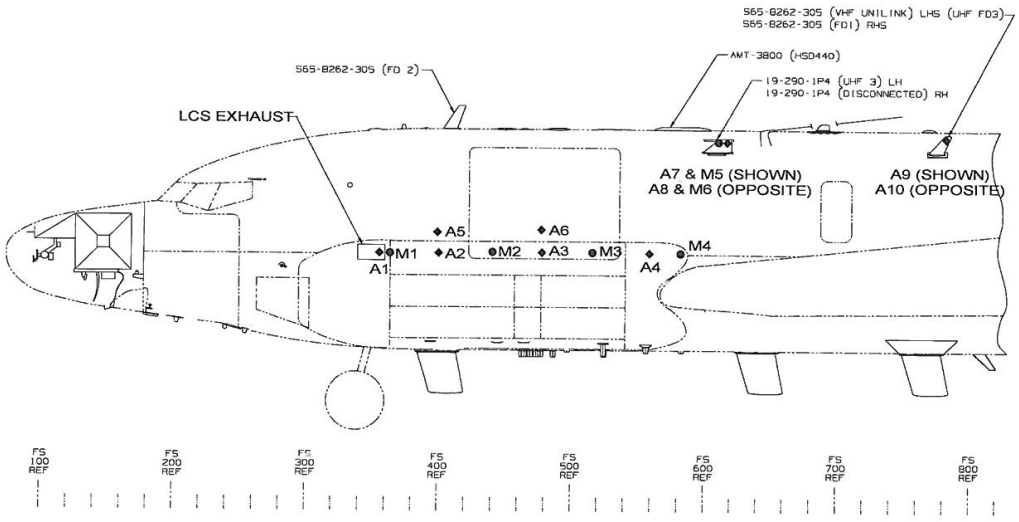


(b)

Figure 4.4: Comparison of (a) model tap locations to (b) flight test microphone locations

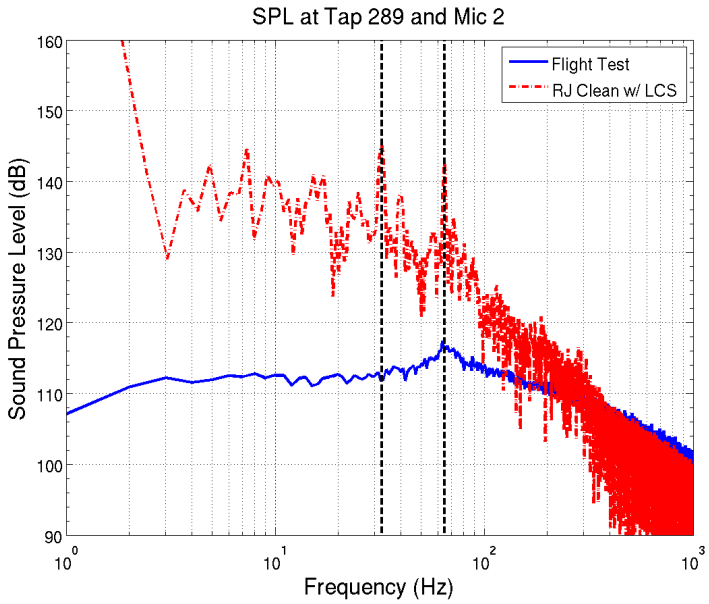


Figure 4.5: Comparison of computational and flight test derived acoustic spectrum

for this case. The second to last microphone/tap comparison is placed in the aft end of the cheek where there is a pocket of separated flow and since exact microphone placement could not be determined, the acoustics would be expected to vary depending on where it is located in relation to this pocket. Additionally, placement of microphone 1 proves tricky as well as there is a fair amount of variance depending on how close the tap is to the exhaust. The jet flow exiting the exhaust seems to initially provide a pocket of "sheltered" flow immediately aft of the exhaust that manifests in lower SPL's. Discounting the known error inherent to comparison with microphones 1, 4, and 5; the remaining two microphone locations exhibit similar acoustic trending despite under-predicting the OASPL by 9.7% and 13.4% respectfully. All in all, this is not completely unreasonable, but still does not provide adequate validation. This should be pursued further in any future research.

## *4.3 Baseline Comparison*

The baseline cases were run as planned for all configurations without antennas. As discussed previously, stability was a major problem with the antenna configurations

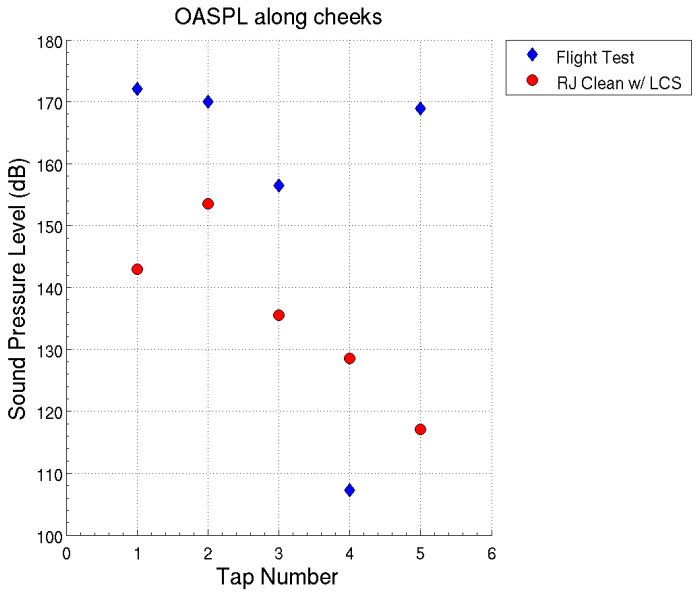


Figure 4.6: Comparison of computational and flight test derived sound pressure levels

and thus full unsteady Navier-Stokes with DDES simulations were not achieved. In order to provide some insight into the flow field around the antennas, Euler solutions were computed for the two antenna configurations without the LCS installed. Despite these problems, the configurations without antennas provide a great opportunity to learn more about the flow-field around the fuselage while discounting the effect of the antennas.

The flow features created by the addition of flow through the LCS are very similar between the two variants and thus will be examined as one. This flow is characterized by unsteady flow stemming from the LCS exhaust being drawn up and along the walls of the fuselage towards the centerline. The turbulent exhaust plume then breaks down and splits into two distinct regions with one being pulled down along the wings towards the lower sides of the fuselage and the other following the side of the top of the fuselage towards the horizontal tail. Figure 4.7 demonstrates an instantaneous solution for the Combat Sent with an iso-surface set at a vorticity of 100 Hz. Figure 4.8 shows iso-surfaces set at a Q-threshold of one. The Q-threshold variable better distinguishes the vortex cores while vorticity includes the larger turbulent

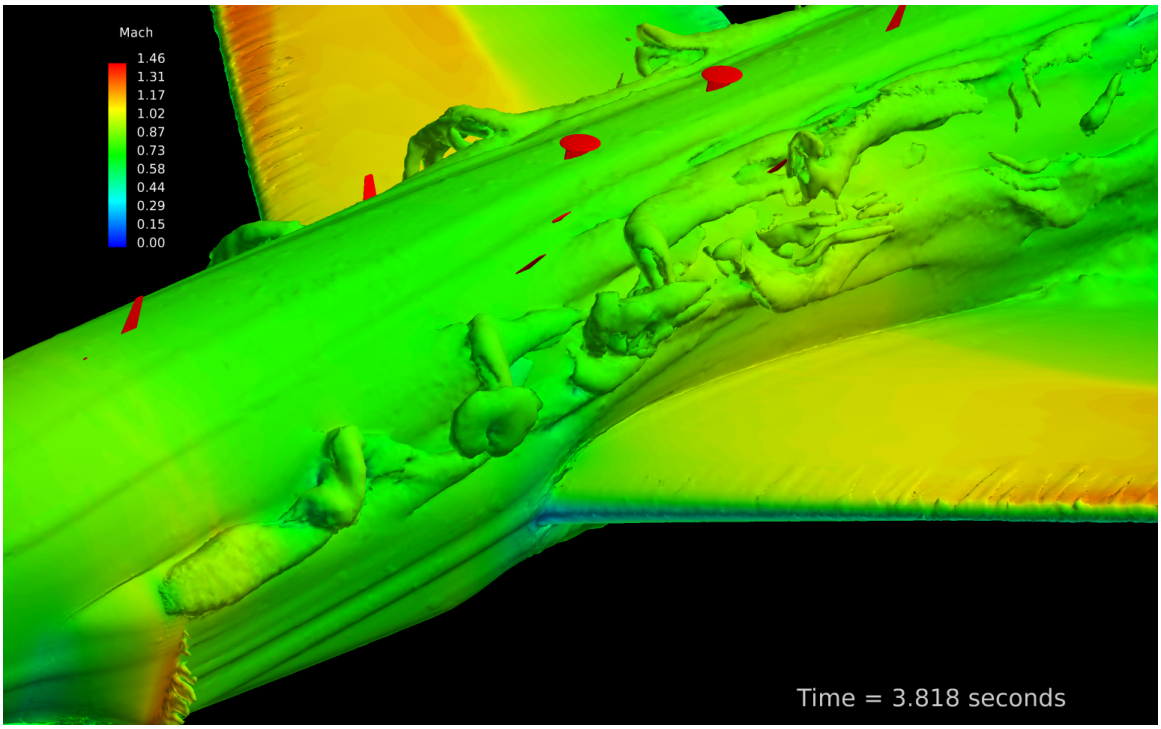


Figure 4.7: Combat Sent with LCS – vorticity of 100 Hz colored by Mach number for baseline comparisons (antennas colored by red shown for reference locations only – not included in solution)

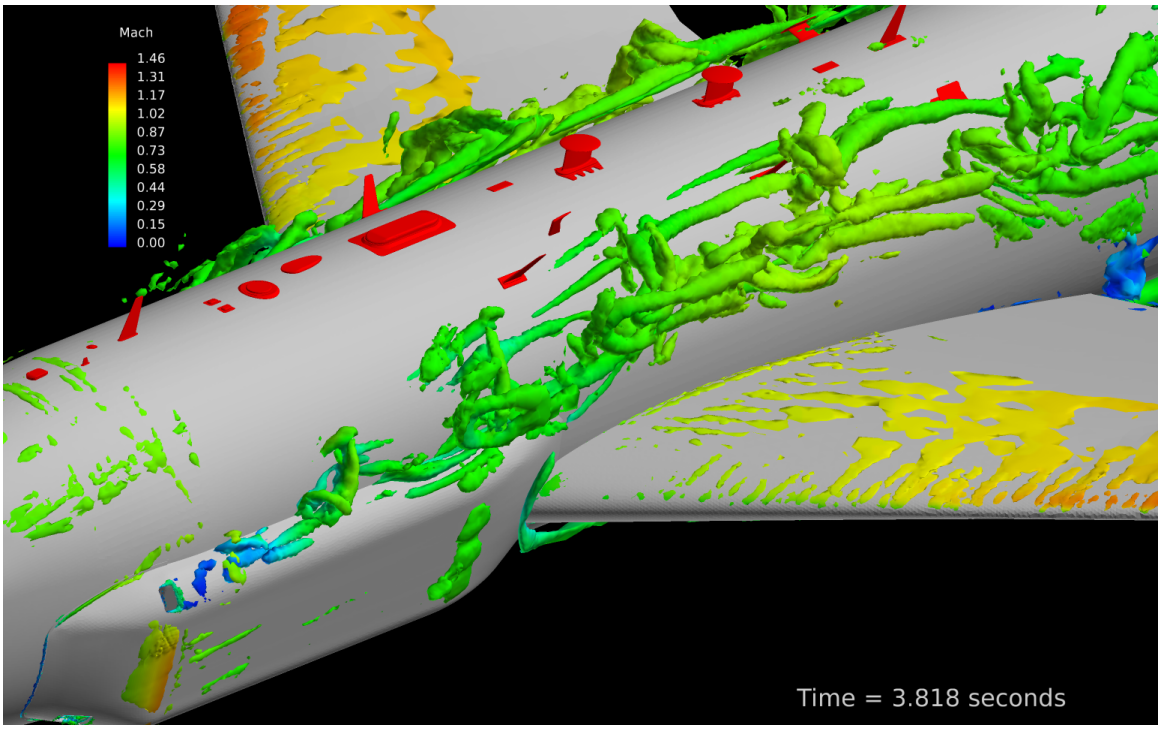


Figure 4.8: Combat Sent with LCS – Q-threshold of 1 colored by vorticity for baseline comparisons (antennas colored by red shown for reference locations only – not included in solution)

structures, including the turbulent boundary layer. The solution for the Rivet Joint is essentially the same and therefore only one or the other will be shown when talking about the fundamental flow features. Note how the exhaust plume just brushes past UHF3 and UHF5 while UHF7 is immersed in the vortex core. This is due, in part, to the low pressure region over the wings drawing the vortex core further up along the fuselage towards the centerline.

Figure 4.9 examines coordinate surfaces with vorticity contours for the Combat Sent, providing insight into the movement and location of the varying vortex cores. The vortex cores tend to build directly aft of the LCS exhaust and immediately move towards the fuselage wall, bouncing off, breaking down, and rotating along the fuselage wall moving up towards the location of UHF7. Aft of UHF7, the upper exhaust plume spreads and travels at approximately the same lateral station along the remainder of the fuselage.

In order to determine where the turbulent air flow affecting the antennas originates, streamlines were computed from seeds along an x-coordinate surface at the location of each antenna. Additionally, the exhaust boundary surface was seeded with points in order to compute streamlines and determine where the exhaust flow is routed. This is shown in Figure 4.10 for the Combat Sent with cooling system installed. Note how the streamlines originating at the LCS exhaust become turbulent immediately after exiting the cheek fairing, wherein the majority of flow travels up towards UHF7 with some of the flow traveling down along the side of the fuselage and over the wing. Most of the flow impacting UHF7 originates from the nose region and is perturbed by the LCS exhaust flow. The flow impacting UHF3 originates from the nose region and is perturbed along the outskirts of the LCS exhaust flow.

The acoustic spectrum extracted for the baseline cases along the top of the cheek fairing aft of the LCS exhaust (Tap 289) is shown in Figure 4.11. There isn't much to report in the frequency domain for the two variants without flow through the LCS, but with flow turned on, a dominant frequency of approximately 40 Hz presents

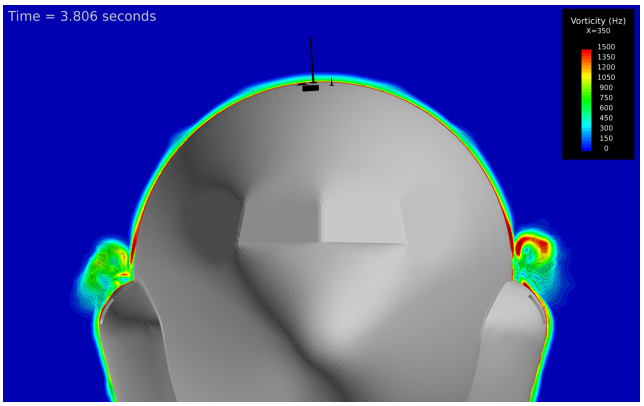


(a)

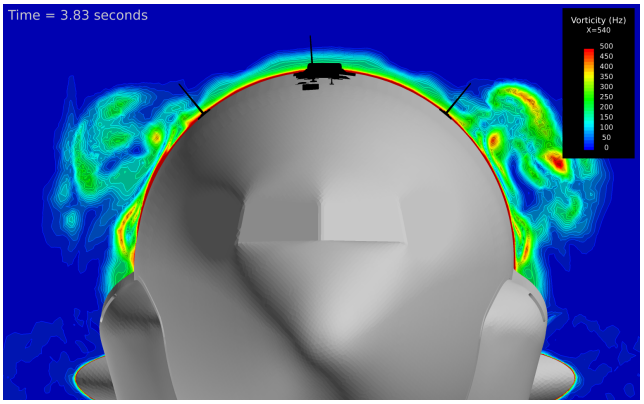


(b)

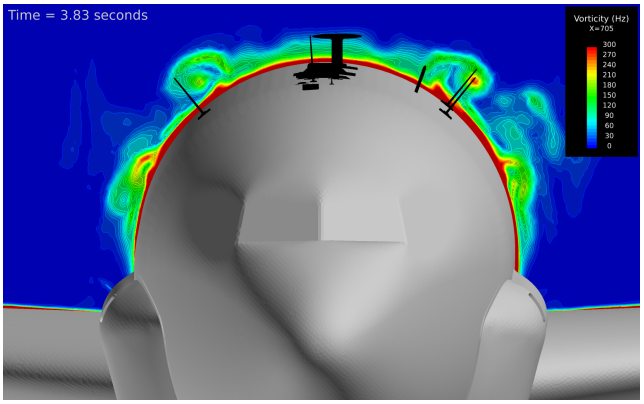


(c)

Figure 4.9: Combat Sent with LCS baseline case time-dependent vorticity structures at locations of (a) FD1 (b) UHF3 and UHF5 (c) UHF7 (antennas colored by black shown for reference locations only – not included in solution)

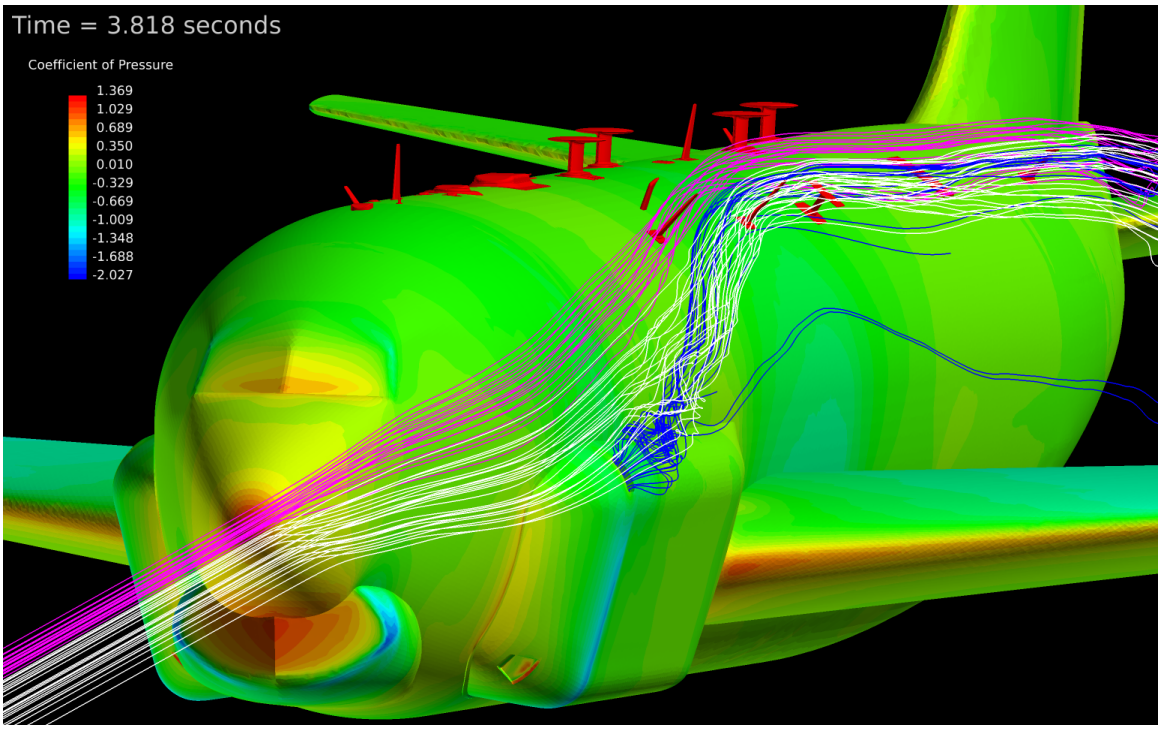


Figure 4.10: Combat Sent with LCS – fuselage surface colored by coefficient of pressure with antennas colors specified by: *blue* streamlines originating from LCS exhaust; *pink* streamlines originating from plane at location of UHF3; *white* streamlines originating from plane at location of UHF7 (antennas colored by red shown for reference locations only – not included in solution)

itself with a secondary frequency of 80 Hz for both cases. It is important to note that

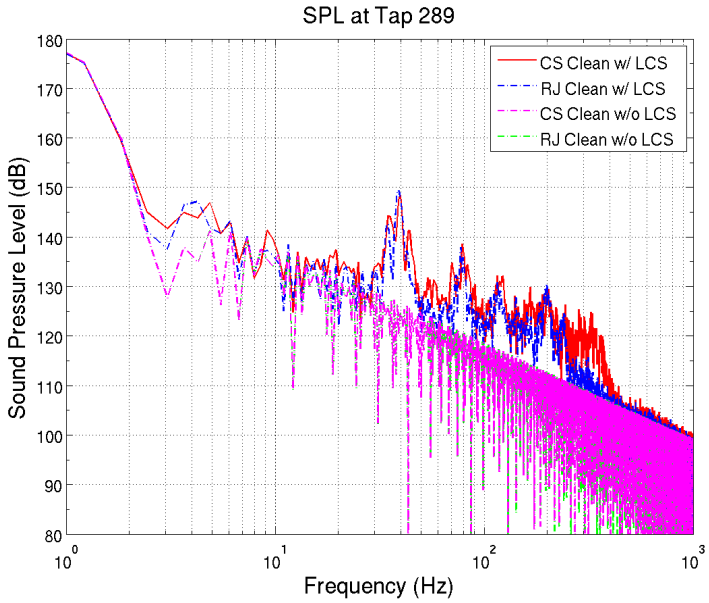


Figure 4.11: Comparison of acoustic spectrum for baseline cases extracted at Tap 289

this is consistent with the dominant acoustic frequency band of 40-45 Hz observed in flight testing as discussed in Section 2.6 [8]. In general, the majority of observed activity is at frequencies less than 500 Hz.

The acoustic spectrum is not always this pronounced at other locations on the aircraft, therefore in order to provide a good means of comparison, the overall sound pressure levels are calculated at all tap locations with results presented in Table 4.2. As expected there is a large increase in noise levels with flow through the LCS resulting in an average increase in OASPL at UHF3 and UHF5 of 27.5%, 19.0% at UHF7, and 7.7% at the two SATCOM BF units. These antennas are all along the side of the upper fuselage and are given in increasing longitudinal distance from the nose, demonstrating a decrease in noise levels with longitudinal distance from the source such as would be expected. There is also a significant increase in noise along the centerline of the fuselage with an average increase of 33.6% at FD2, 15.9% at FD4 and 5.2% at UHF9. Note that the largest increase here is not in the direct path of the exhaust plume, but rather along the centerline at FD2. This is not very far aft of the

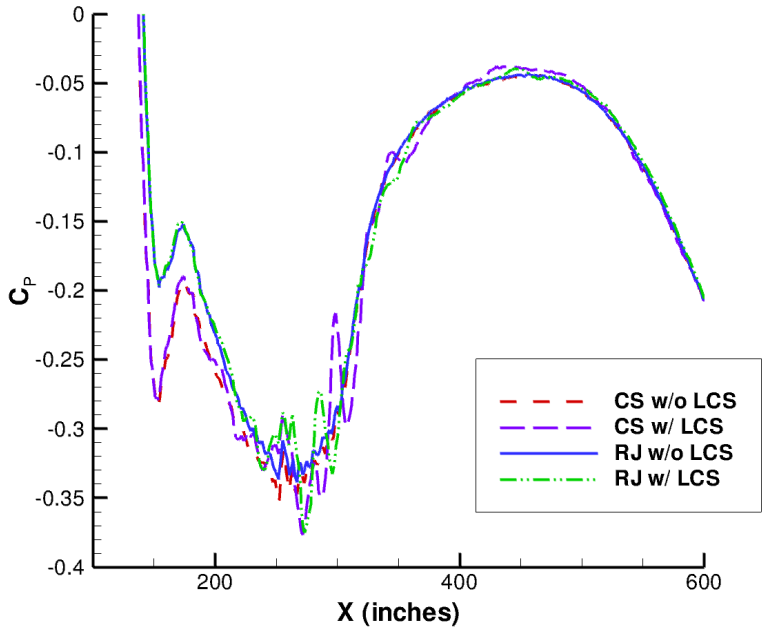


Figure 4.12: Comparison of coefficient of pressure along the fuselage centerline for baseline cases

LCS exhaust and demonstrates the large effect that this exhaust has on the overall flow-field. Figure 4.12 demonstrates this effect, showing coefficient of pressure along the centerline of the forward fuselage. This is just a snapshot in time, but notice the large longitudinal oscillations in pressure that are the source of the noise at the location of FD2.

Despite the increased noise levels at FD2, this does not necessarily mean that antenna buffeting would be expected at this location. Remember that there are three rows of three taps each located on each side of the antenna and that the increasing number corresponds to movement from leading to trailing edge and root to tip. Referring to Figure 4.13, note that sound pressure levels are largest at the root of the antenna and decrease gradually traveling upward towards the location of the blade tip. These pressure fluctuations could simply be a result of a fluctuating boundary layer due to the pressure oscillations pointed out in Figure 4.12.

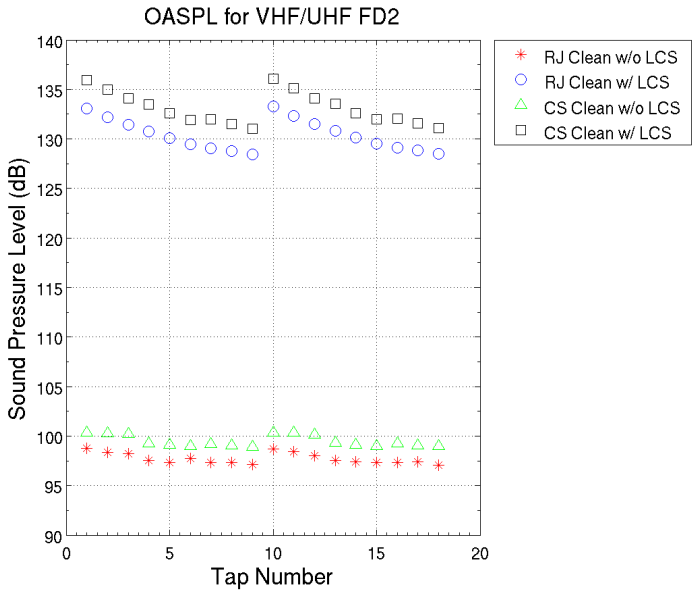


Figure 4.13: Comparison of overall sound pressure levels at location of FD2 for baseline cases

Now looking at the location of the UHF7 Unilink antenna, which is known to exhibit high vibrational loading, and there is a rapid increase in OASPL moving from root to tip as shown in Figure 4.14. Possibly, disturbances of this nature could be more prone to excitation of antenna buffeting than the boundary layer oriented unsteadiness apparent at the location of FD2. In order to distinguish this type of disturbance, examine the standard deviation of OASPL as shown in Table 4.2. Note the significantly higher standard deviation at UHF7 of 3.1376 dB for the Rivet Joint with LCS and 2.9360 dB for the Combat Sent with LCS. The combination of large standard deviation and increasing OASPL moving from location of antenna root to tip will be used as an indication of a possible problem region throughout the remainder of this investigation.

Between the two variants, the Combat Sent experiences slightly elevated noise levels without flow through the LCS with an increase of 1.4% at UHF3/UHF5, 4.0% at UHF7, and 3.5% at the two SATCOM BF units. While with flow through the LCS, the difference drops even more with an increase of 0.6% at UHF3/UHF5, 0.1% at UHF7, and 0.7% at the two SATCOM BF units. Along the centerline without flow,

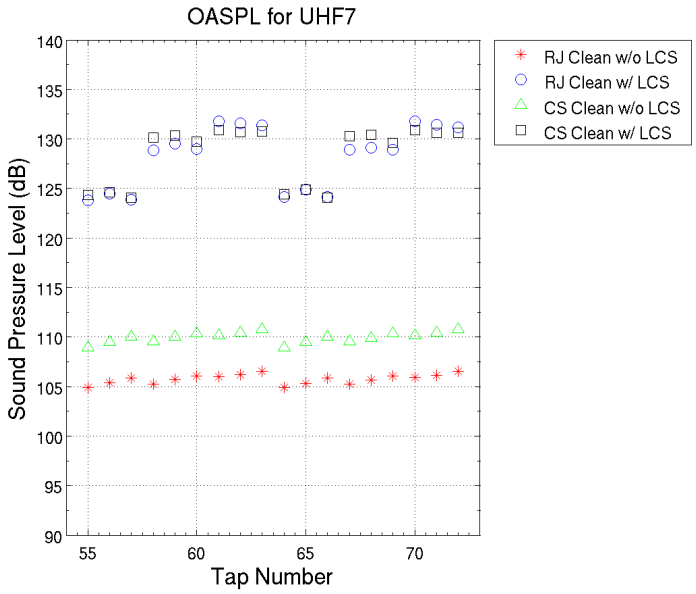


Figure 4.14: Comparison of overall sound pressure levels at location of UHF7 for baseline cases

the Combat Sent experiences an increase of 1.8% at FD2, 3.1% at FD4, and 4.1% at UHF9 over that of the Rivet Joint. Along the centerline with flow, the Combat Sent experiences an increase of 2.1% at FD2, 1.1% at FD4, and 0.1% at UHF9 over that of the Rivet Joint.

To provide further insight into how the flow-field is affected by antennas, Euler solutions were computed for the two antenna cases without flow through the LCS. Figure 4.15 shows shock wave locations with antennas installed. Note the presence of shock waves on the inside surfaces of UHF3 and UHF5 followed by a region of very low Mach number flow. This demonstrates the presence of shock induced separation on these antennas which is only exacerbated with the higher angle of attack as will be discussed in Section 4.5. Keep in mind, this is an Euler solution and thus will over-predict separation, although the extent of this separation means that it will probably still manifest itself on these antennas even with a viscous solution. It is also important to note that, in general, the larger the extent of the Mach=1 iso-surface, the weaker the shock. The shock present on UHF3 and UHF5 is a strong shock and thus spends little time right at Mach=1, while the shock over FD4 spends more time right around

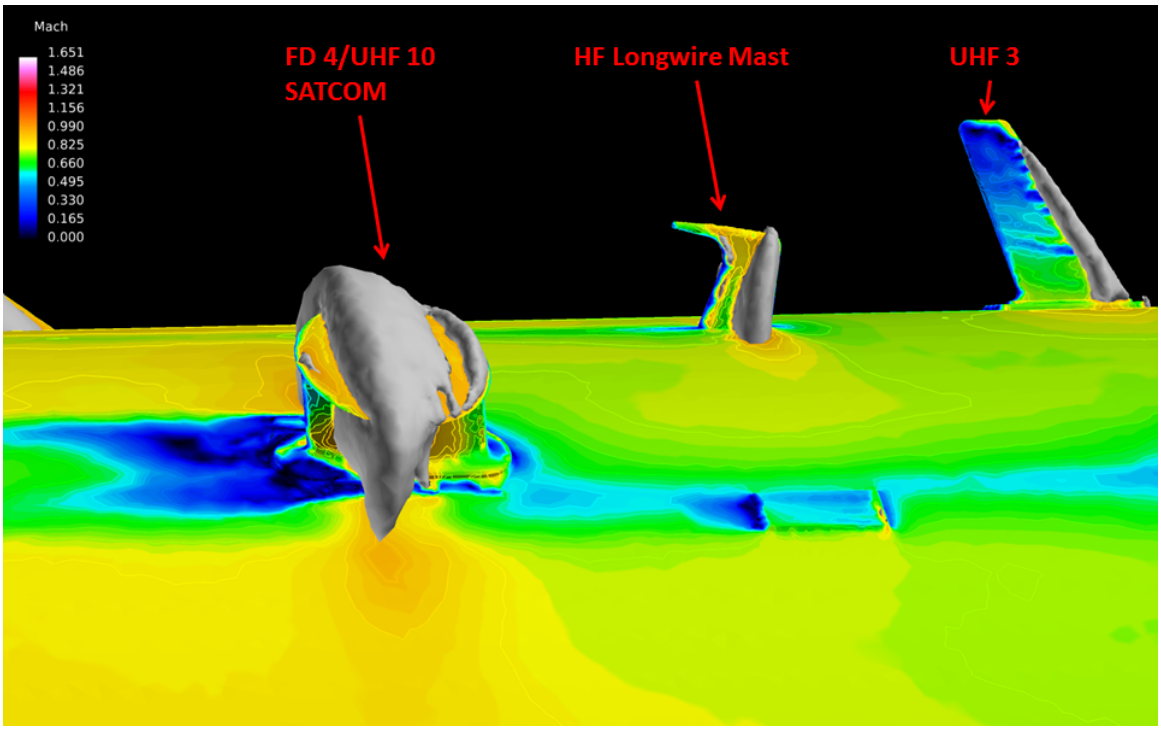


Figure 4.15: Combat Sent with antennas and without LCS – baseline case showing FD4/UHF10 SATCOM and UHF3; fuselage and antenna surfaces colored by Mach number with Mach=1 iso-surfaces shown in gray (flow is going from right to left)

Mach=1 and thus is weaker resulting in less flow separation. Figure 4.16 points out

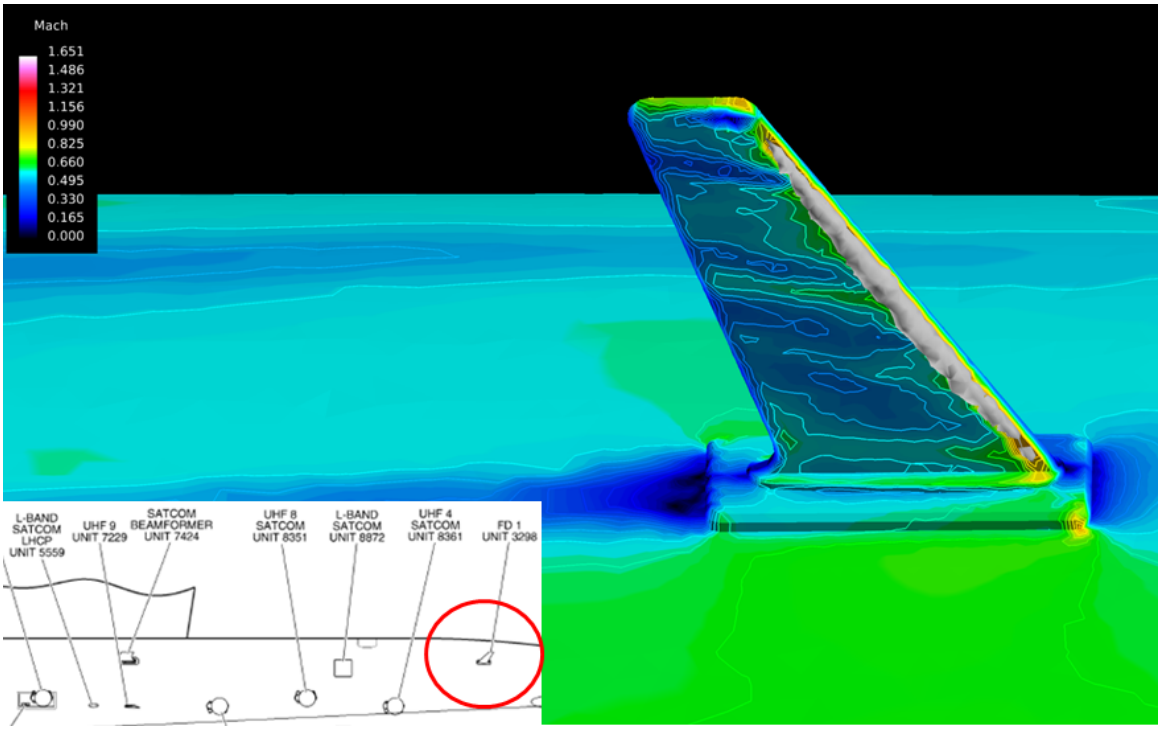


Figure 4.16: Combat Sent with antennas and without LCS – baseline case showing FD1; fuselage and antenna surfaces colored by Mach number with Mach=1 isosurfaces shown in gray (flow is going from right to left)

another location where shock-induced separation is a possible problem. In this case, the problem presents itself on FD1, which is located in the aft section of the fuselage on the same lateral offset as UHF5. Note that the separation occurs only on the outward facing surface of FD1.

Figure 4.17 provides a comparison of Mach number along the fuselage for the Rivet Joint and Combat Sent variants. Note that the Mach numbers stay fairly consistent between the two variants until the aft section of the fuselage is reached wherein the Rivet Joint exhibits slightly elevated numbers. This comparison is completed with antennas in the flow-field.

The acoustic analysis for the baseline cases provides some indication of possible problems at UHF7, but does not any indication about why UHF3 would be having more problems. The Euler solutions presented here point to the possibility that

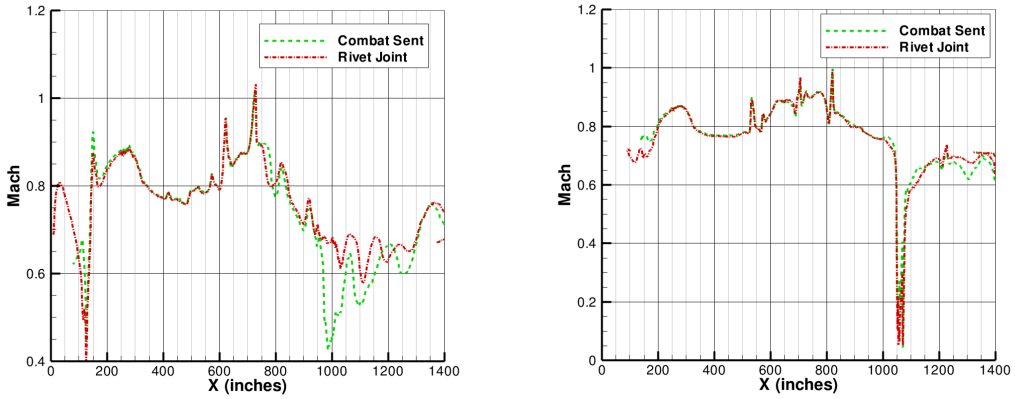


(a) (b)

Figure 4.17: Comparison of Mach number along fuselage for baseline case at (a) $Y = -20$" (b) $Y = -40$"

the increased velocities at the locations of UHF3 and UHF5 could excite buffeting due to shock induced separation. The increased noise levels at the locations of these antennas would only add to the problem. Although, viscous simulations should be run to confirm this assertion. Additionally, the noise levels are not very different between the two variants, although it is interesting to point out the increase in standard deviation at UHF7 of 6.7% from the Combat Sent to the Rivet Joint. This could be an indication of the increase in problems with that variant. Although, once again, more research is needed to back up this claim.

Table 4.2: Comparison of overall sound pressure levels at each antenna location for baseline cases

| Case | FD2 | | UHF3 | | UHF5 | |
|---|---|---|---|---|---|---|
| | $\overline{\mathbf{OASPL}}$ | $\sigma_{\mathbf{OASPL}}$ | $\overline{\mathbf{OASPL}}$ | $\sigma_{\mathbf{OASPL}}$ | $\overline{\mathbf{OASPL}}$ | $\sigma_{\mathbf{OASPL}}$ |
| RJ w/o LCS | 97.7222 | 0.5458 | 96.7519 | 0.2943 | 97.3516 | 0.3867 |
| RJ w/ LCS | 130.4130 | 1.5892 | 124.3813 | 0.5021 | 124.5753 | 0.4874 |
| CS w/o LCS | 99.4718 | 0.5778 | 97.9283 | 0.2888 | 98.9776 | 0.2755 |
| CS w/ LCS | 133.0935 | 1.6371 | 125.7313 | 0.6271 | 124.7049 | 0.7740 |
| **Case** | **UHF7** | | **UHF9** | | **FD1** | |
| | $\overline{\mathbf{OASPL}}$ | $\sigma_{\mathbf{OASPL}}$ | $\overline{\mathbf{OASPL}}$ | $\sigma_{\mathbf{OASPL}}$ | $\overline{\mathbf{OASPL}}$ | $\sigma_{\mathbf{OASPL}}$ |
| RJ w/o LCS | 105.7458 | 0.4922 | 112.1371 | 0.1488 | 106.4271 | 0.2398 |
| RJ w/ LCS | 128.2773 | 3.1376 | 120.4007 | 0.3920 | 124.5243 | 0.6708 |
| CS w/o LCS | 109.9546 | 0.5430 | 116.7263 | 0.1122 | 112.0272 | 0.2581 |
| CS w/ LCS | 128.4139 | 2.9360 | 120.3070 | 0.5232 | 123.8806 | 0.5818 |
| **Case** | **FD3** | | **FD4** | | **JTT** | |
| | $\overline{\mathbf{OASPL}}$ | $\sigma_{\mathbf{OASPL}}$ | $\overline{\mathbf{OASPL}}$ | $\sigma_{\mathbf{OASPL}}$ | $\overline{\mathbf{OASPL}}$ | $\sigma_{\mathbf{OASPL}}$ |
| RJ w/o LCS | 105.7182 | 0.2619 | 99.4128 | 0.3896 | 108.5129 | 0.8598 |
| RJ w/ LCS | 124.5579 | 1.1737 | 116.3119 | 0.5445 | 118.5252 | 0.4647 |
| CS w/o LCS | 112.8744 | 0.1453 | 102.4512 | 0.4349 | 113.4059 | 0.7915 |
| CS w/ LCS | 124.2033 | 0.6710 | 117.5622 | 0.5009 | 118.4125 | 0.4853 |
| **Case** | **UHF6** | | **UHF8** | | **BF7421** | |
| | $\overline{\mathbf{OASPL}}$ | $\sigma_{\mathbf{OASPL}}$ | $\overline{\mathbf{OASPL}}$ | $\sigma_{\mathbf{OASPL}}$ | $\overline{\mathbf{OASPL}}$ | $\sigma_{\mathbf{OASPL}}$ |
| RJ w/o LCS | 108.3679 | 0.1957 | 107.2458 | 0.1416 | 115.0891 | 0.3328 |
| RJ w/ LCS | 116.7187 | 0.4746 | 115.5929 | 0.5673 | 127.9741 | 0.5829 |
| CS w/o LCS | 113.0693 | 0.1557 | 112.1709 | 0.0820 | 118.9913 | 0.3024 |
| CS w/ LCS | 118.1720 | 0.6739 | 118.0898 | 0.6207 | 126.9883 | 0.6064 |
| **Case** | **BF7424** | | | | | |
| | $\overline{\mathbf{OASPL}}$ | $\sigma_{\mathbf{OASPL}}$ | | | | |
| RJ w/o LCS | 115.1489 | 0.4120 | | | | |
| RJ w/ LCS | 125.1631 | 0.3123 | | | | |
| CS w/o LCS | 119.3995 | 0.3103 | | | | |
| CS w/ LCS | 124.4288 | 0.5395 | | | | |

### *4.4 Mass Flow Rate Sensitivity Study*

Three additional mass flow rates through the LCS were simulated and compared against the baseline flow rate for both variants. Figures 4.18 and 4.19 show streamlines originating on the LCS exhaust boundary plane for all mass flow rates. Note how the streamlines for the Rivet Joint are much more focused over the two distinct regions. A portion of the exhaust plume branches off, being pulled along the wing onto the lower side of the fuselage. For the Rivet Joint, the two branches of the plume are much more distinct, suggesting a more focused plume. The exhaust plume of the Combat Sent is more spread out between the two regions, although, in this case, the plume seems to drift more towards UHF7, explaining the higher noise levels. With higher mass flow rate, the exhaust plume pulls lower along the fuselage but is not necessarily more focused. Also, with the higher the mass flow rate, less streamlines join the lower branch with more of a focus on the upper fuselage.

It is difficult to determine what is the root cause of this difference in exhaust plume between the two variants. The Rivet Joint certainly has a more focused plume and, as discussed in Section 4.3, the Rivet Joint does exhibit slightly higher velocities along the upper fuselage, with the differences increasing towards the aft of the fuselage as shown in Figure 4.17. The lower velocities observed with the Combat Sent could allow for an increased spreading rate for the exhaust plume.

There was not a large difference in experienced noise levels with changes to flow rate but there are some interesting effects that should be examined. At the location of UHF3 and UHF5, there was an average increase in noise levels with the transition from low to baseline to high mass flow rate cases of 1.2% and 1.8% for the Rivet Joint. For this same variant when transitioning from high to very high, the noise level dropped 1.9% while the standard deviation increased by 48.2%. The Combat Sent experienced the typical increasing trend with the exception of the transition from baseline to high on UHF5 where the noise level dropped 1.3% while standard deviation increased by 95.3% before dropping back down to values consistent with the

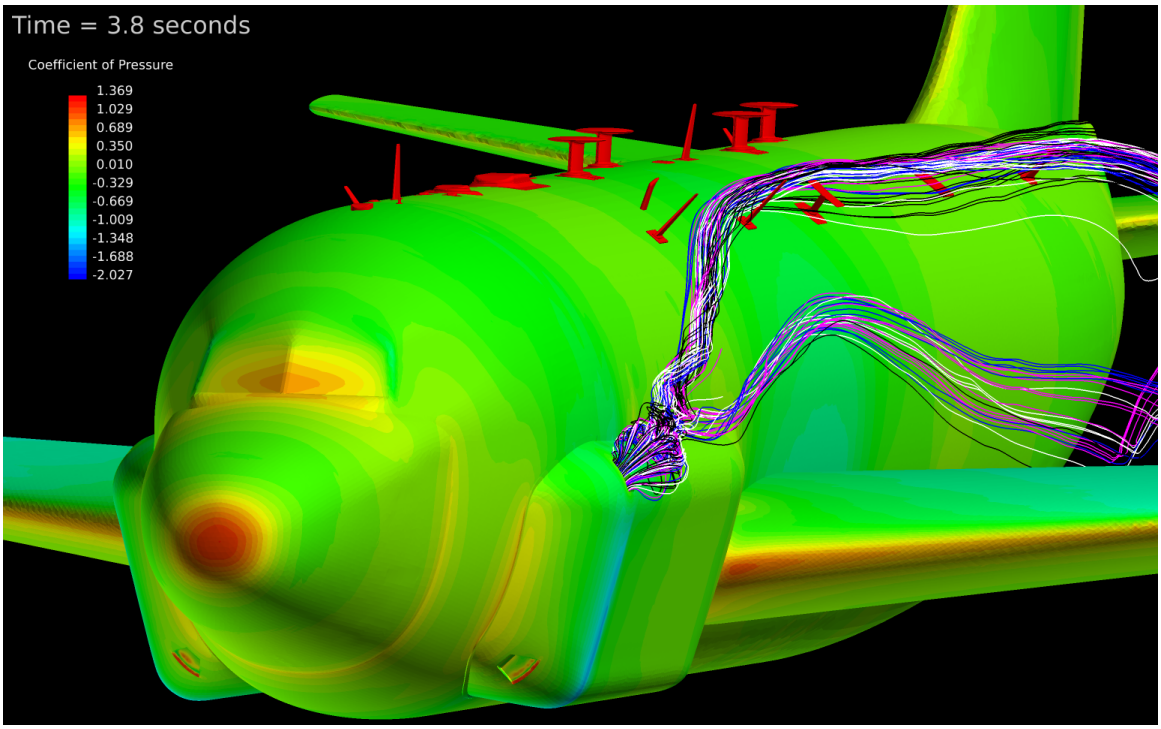


Figure 4.18: Rivet Joint with LCS – streamlines originating at LCS exhaust with *blue* 161 lbm/min; *pink* 190 lbm/min; *white* 247 lbm/min; *black* 350 lbm/min (antennas colored by red shown for reference locations only – not included in solution)

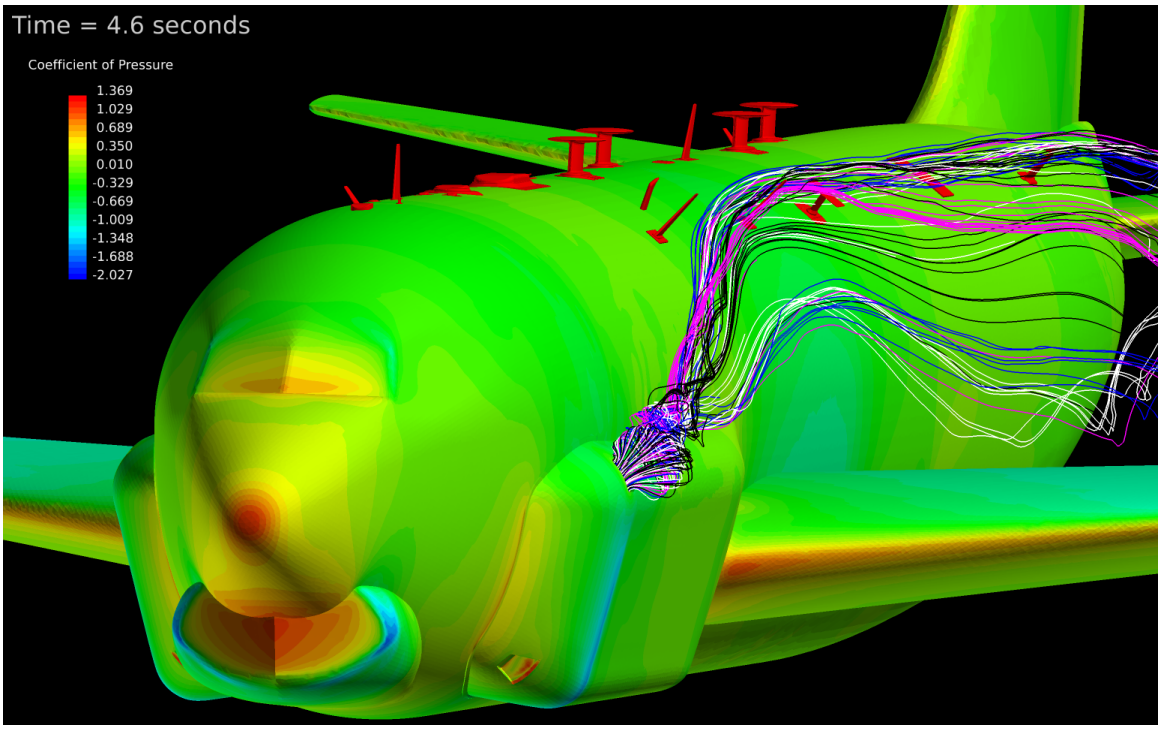


Figure 4.19: Combat Sent with LCS – streamlines originating at LCS exhaust with *blue* 161 lbm/min; *pink* 190 lbm/min; *white* 247 lbm/min; *black* 350 lbm/min (antennas colored by red shown for reference locations only – not included in solution)

baseline rate. These seems to indicate that there may be a "sweet" spot wherein if the correct mass flow rate is chosen, antenna excitation may occur. This is illustrated in Figure 4.20 showing how mean and standard deviation change with varying mass flow rates.

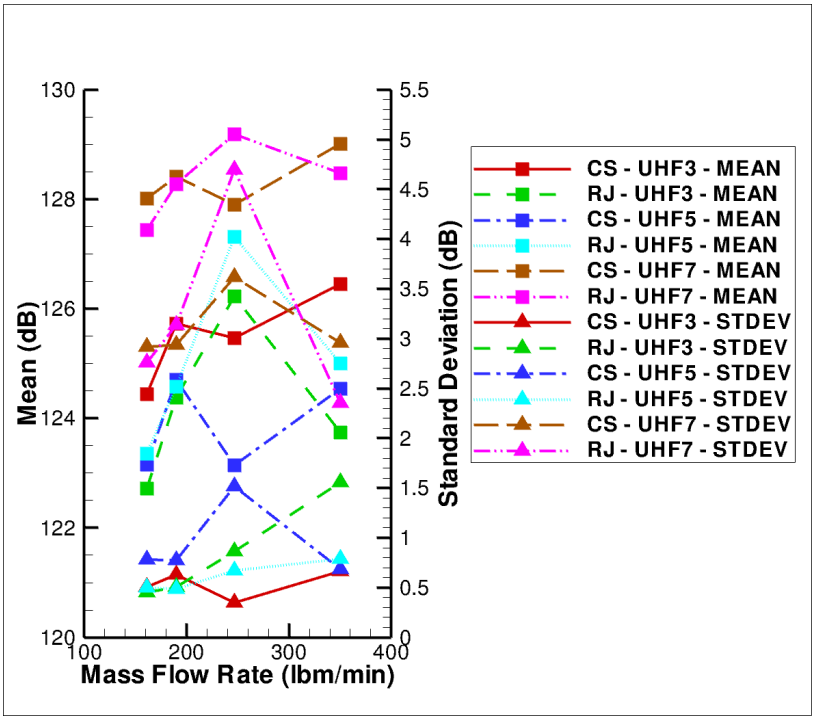


Figure 4.20: Comparison of overall sound pressure level statistics at the locations of UHF3, UHF5, and UHF7 for mass flow rate sensitivity study

Again, the correlation to high standard deviation must correspond to an increase in noise levels moving from root to tip at the location of the antenna. Figure 4.21 demonstrates this effect at the location of UHF7 for all mass flow rates, although, for the low mass flow rate cases, there is a drop in noise levels at the location of the antenna tip. Figure 4.22 shows that this effect is not as pronounced the UHF3 and UHF5 locations, although, for some mass flow rates, there is a slight increase in noise levels moving from root to tip, such as with the very high mass flow rate case for the RJ and, to a lesser extent, the high mass flow rate case for the CS.

Ultimately, the variation in mass flow rate does not seem to impact the solution significantly. Since the turbulent exhaust from the cooling system is not directly

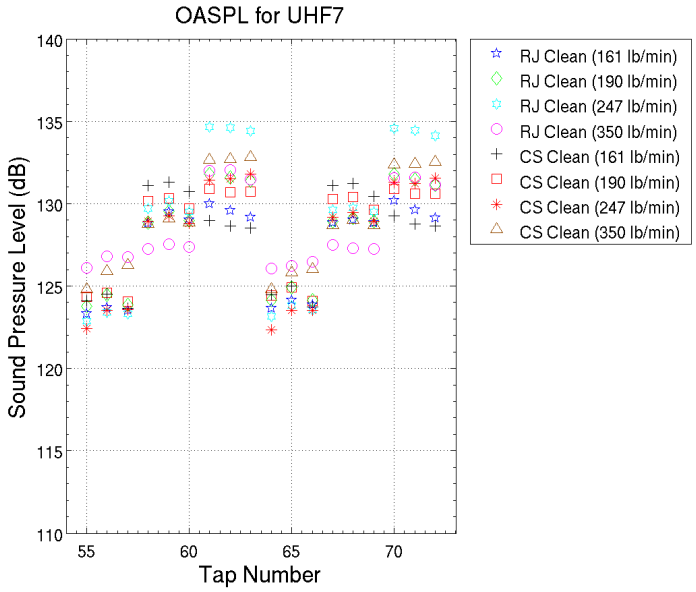


Figure 4.21: Comparison of overall sound pressure levels at the location of UHF7 for mass flow rate sensitivity study

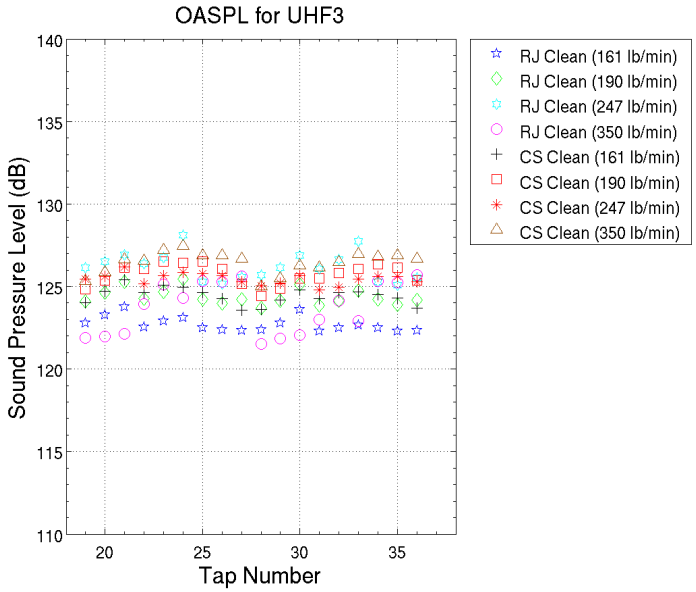


Figure 4.22: Comparison of overall sound pressure levels at the location of UHF3 for mass flow rate sensitivity study

impacting the locations of the UHF3 and UHF5 antennas, the mass flow rate seems to have more of an impact at these locations, as the exhaust plume is slightly shifted from the baseline position. It would be interesting to see what effect mass flow rate has with the antennas present in the flow-field, which could be an area of future research.

Table 4.3: Comparison of overall sound pressure levels at each antenna location for LCS mass flow rate sensitivity study - Rivet Joint

| Case | FD2 | | UHF3 | | UHF5 | |
|---|---|---|---|---|---|---|
| | $\overline{\mathbf{OASPL}}$ | $\sigma_{\mathbf{OASPL}}$ | $\overline{\mathbf{OASPL}}$ | $\sigma_{\mathbf{OASPL}}$ | $\overline{\mathbf{OASPL}}$ | $\sigma_{\mathbf{OASPL}}$ |
| RJ (161 lbm/min) | 131.8792 | 1.5435 | 122.7215 | 0.4505 | 123.3550 | 0.4985 |
| RJ (190 lbm/min) | 130.4130 | 1.5892 | 124.3813 | 0.5021 | 124.5753 | 0.4874 |
| RJ (247 lbm/min) | 133.1549 | 1.4678 | 126.2234 | 0.8645 | 127.3113 | 0.6721 |
| RJ (350 lbm/min) | 131.4765 | 1.5307 | 123.7424 | 1.5530 | 125.0002 | 0.7851 |
| **Case** | **UHF7** | | **UHF9** | | **FD1** | |
| | $\overline{\mathbf{OASPL}}$ | $\sigma_{\mathbf{OASPL}}$ | $\overline{\mathbf{OASPL}}$ | $\sigma_{\mathbf{OASPL}}$ | $\overline{\mathbf{OASPL}}$ | $\sigma_{\mathbf{OASPL}}$ |
| RJ (161 lbm/min) | 127.4391 | 2.7549 | 121.3999 | 0.4462 | 123.6871 | 0.8021 |
| RJ (190 lbm/min) | 128.2773 | 3.1376 | 120.4007 | 0.3920 | 124.5243 | 0.6708 |
| RJ (247 lbm/min) | 129.1804 | 4.6938 | 122.3949 | 0.5129 | 124.9308 | 0.6090 |
| RJ (350 lbm/min) | 128.4709 | 2.3552 | 122.4040 | 0.3676 | 124.6472 | 1.0067 |
| **Case** | **FD3** | | **FD4** | | **JTT** | |
| | $\overline{\mathbf{OASPL}}$ | $\sigma_{\mathbf{OASPL}}$ | $\overline{\mathbf{OASPL}}$ | $\sigma_{\mathbf{OASPL}}$ | $\overline{\mathbf{OASPL}}$ | $\sigma_{\mathbf{OASPL}}$ |
| RJ (161 lbm/min) | 124.6692 | 1.6398 | 115.9360 | 0.4073 | 119.1853 | 0.4073 |
| RJ (190 lbm/min) | 124.5579 | 1.1737 | 116.3119 | 0.5445 | 118.5252 | 0.4647 |
| RJ (247 lbm/min) | 125.1199 | 0.9941 | 118.2572 | 0.5008 | 119.2788 | 0.4177 |
| RJ (350 lbm/min) | 122.6301 | 1.4341 | 116.1376 | 0.5400 | 120.0217 | 0.5661 |
| **Case** | **UHF6** | | **UHF8** | | **BF7421** | |
| | $\overline{\mathbf{OASPL}}$ | $\sigma_{\mathbf{OASPL}}$ | $\overline{\mathbf{OASPL}}$ | $\sigma_{\mathbf{OASPL}}$ | $\overline{\mathbf{OASPL}}$ | $\sigma_{\mathbf{OASPL}}$ |
| RJ (161 lbm/min) | 117.0466 | 0.5021 | 116.0003 | 0.5247 | 127.6468 | 0.5247 |
| RJ (190 lbm/min) | 116.7187 | 0.4746 | 115.5929 | 0.5673 | 127.9741 | 0.5673 |
| RJ (247 lbm/min) | 118.5529 | 0.4221 | 117.5019 | 0.4849 | 127.9416 | 0.4849 |
| RJ (350 lbm/min) | 118.1266 | 0.7004 | 115.9776 | 0.7073 | 127.7040 | 0.7073 |
| **Case** | **BF7424** | | | | | |
| | $\overline{\mathbf{OASPL}}$ | $\sigma_{\mathbf{OASPL}}$ | | | | |
| RJ (161 lbm/min) | 125.4639 | 0.7465 | | | | |
| RJ (190 lbm/min) | 125.1631 | 0.3123 | | | | |
| RJ (247 lbm/min) | 125.6877 | 0.5014 | | | | |
| RJ (350 lbm/min) | 124.3383 | 0.4069 | | | | |

Table 4.4: Comparison of overall sound pressure levels at each antenna location for LCS mass flow rate sensitivity study - Combat Sent

| Case | FD2 | | UHF3 | | UHF5 | |
|---|---|---|---|---|---|---|
| | $\overline{\mathbf{OASPL}}$ | $\sigma_{\mathbf{OASPL}}$ | $\overline{\mathbf{OASPL}}$ | $\sigma_{\mathbf{OASPL}}$ | $\overline{\mathbf{OASPL}}$ | $\sigma_{\mathbf{OASPL}}$ |
| CS (161 lbm/min) | 132.7371 | 1.5566 | 124.4442 | 0.5073 | 123.1538 | 0.7808 |
| CS (190 lbm/min) | 133.0935 | 1.6371 | 125.7313 | 0.6271 | 124.7049 | 0.7740 |
| CS (247 lbm/min) | 131.2582 | 2.2169 | 125.4595 | 0.3483 | 123.1437 | 1.5118 |
| CS (350 lbm/min) | 135.4051 | 2.2624 | 126.4509 | 0.6626 | 124.5357 | 0.6820 |
| **Case** | **UHF7** | | **UHF9** | | **FD1** | |
| | $\overline{\mathbf{OASPL}}$ | $\sigma_{\mathbf{OASPL}}$ | $\overline{\mathbf{OASPL}}$ | $\sigma_{\mathbf{OASPL}}$ | $\overline{\mathbf{OASPL}}$ | $\sigma_{\mathbf{OASPL}}$ |
| CS (161 lbm/min) | 128.0104 | 2.9146 | 120.7688 | 0.4506 | 123.4444 | 0.7945 |
| CS (190 lbm/min) | 128.4139 | 2.9360 | 120.3070 | 0.5232 | 123.8806 | 0.5818 |
| CS (247 lbm/min) | 127.9041 | 3.6183 | 122.0081 | 0.3351 | 125.4968 | 0.9717 |
| CS (350 lbm/min) | 129.0137 | 2.9552 | 121.6295 | 0.4307 | 122.7371 | 1.0521 |
| **Case** | **FD3** | | **FD4** | | **JTT** | |
| | $\overline{\mathbf{OASPL}}$ | $\sigma_{\mathbf{OASPL}}$ | $\overline{\mathbf{OASPL}}$ | $\sigma_{\mathbf{OASPL}}$ | $\overline{\mathbf{OASPL}}$ | $\sigma_{\mathbf{OASPL}}$ |
| CS (161 lbm/min) | 123.6830 | 0.9031 | 115.9034 | 0.4110 | 118.1291 | 0.5230 |
| CS (190 lbm/min) | 124.2033 | 0.6710 | 117.5622 | 0.5009 | 118.4125 | 0.4853 |
| CS (247 lbm/min) | 124.2080 | 0.5072 | 117.3685 | 0.6099 | 120.2032 | 0.4809 |
| CS (350 lbm/min) | 124.5478 | 0.9523 | 118.6533 | 0.6643 | 121.2515 | 0.7048 |
| **Case** | **UHF6** | | **UHF8** | | **BF7421** | |
| | $\overline{\mathbf{OASPL}}$ | $\sigma_{\mathbf{OASPL}}$ | $\overline{\mathbf{OASPL}}$ | $\sigma_{\mathbf{OASPL}}$ | $\overline{\mathbf{OASPL}}$ | $\sigma_{\mathbf{OASPL}}$ |
| CS (161 lbm/min) | 117.6771 | 0.6900 | 117.2395 | 0.6810 | 127.6659 | 0.5251 |
| CS (190 lbm/min) | 118.1720 | 0.6739 | 118.0898 | 0.6207 | 126.9883 | 0.6064 |
| CS (247 lbm/min) | 118.3188 | 0.3717 | 117.2827 | 0.4924 | 127.7094 | 0.4746 |
| CS (350 lbm/min) | 119.8702 | 0.5797 | 118.8941 | 0.6009 | 126.8723 | 0.5635 |
| **Case** | **BF7424** | | | | | |
| | $\overline{\mathbf{OASPL}}$ | $\sigma_{\mathbf{OASPL}}$ | | | | |
| CS (161 lbm/min) | 124.3383 | 0.4803 | | | | |
| CS (190 lbm/min) | 124.4288 | 0.5395 | | | | |
| CS (247 lbm/min) | 122.8272 | 0.8671 | | | | |
| CS (350 lbm/min) | 123.1839 | 0.6735 | | | | |

### *4.5 Angle of Attack Sensitivity Study*

For the angle of attack sensitivity study, all configurations without antennas were simulated at a higher angle of attack of 8 degrees and compared to the baseline cases at an angle of attack of 4 degrees. Euler solutions were computed for the two configurations with antennas and without flow through the LCS.

Figure 4.23 shows iso-surfaces at a vorticity of 100 Hz colored by Mach number. Again, the exhaust plume structures emanating from the cooling system are clearly shown being drawn up towards the locations of UHF3/UHF5 and UHF7. Although, for the higher angle of attack, the plume is pulled further up towards centerline and impacts UHF3 and UHF5 directly. Figure 4.24 shows a different view of the upper fuselage showing shear layers separating off of the fuselage at the lateral stations of UHF3 and UHF5. Notice how the turbulent structures are offset more from the surface of the fuselage. The exhaust structures rise up and away from the aircraft where the unsteadiness is damped out as the grid coarsens outside of the focus region. Figure 4.25 shows the finer structures inherent to the turbulent flow, distinguishing the vortex cores from the shear layers. This view really shows how the exhaust structures lift up and away from the aircraft breaking down and spreading out. The structures that disappear in the vorticity iso-surface due to the grid coarsening reappear and really highlight the structures as they break down. Also, note how this figure confirms the impact of the LCS exhaust on the location of UHF3, UHF5, and UHF7.

Figure 4.26 displays coordinate surfaces colored by vorticity at the locations of FD1, UHF3/UHF5, and UHF7. This is an instantaneous solution, but this provides further insight into the vortical structures inherent to this flow. As with the baseline cases, the vortex structures form aft of the exhaust rotating and bouncing off of the side of the fuselage before traveling aft as they are drawn up along the fuselage. The region of movement grows and there are multiple cores observed as the longitudinal distance grows. With the higher angle of attack, there is a definite region of vorticity directly at the location of UHF3 and UHF5. Again, vortex cores are seen moving

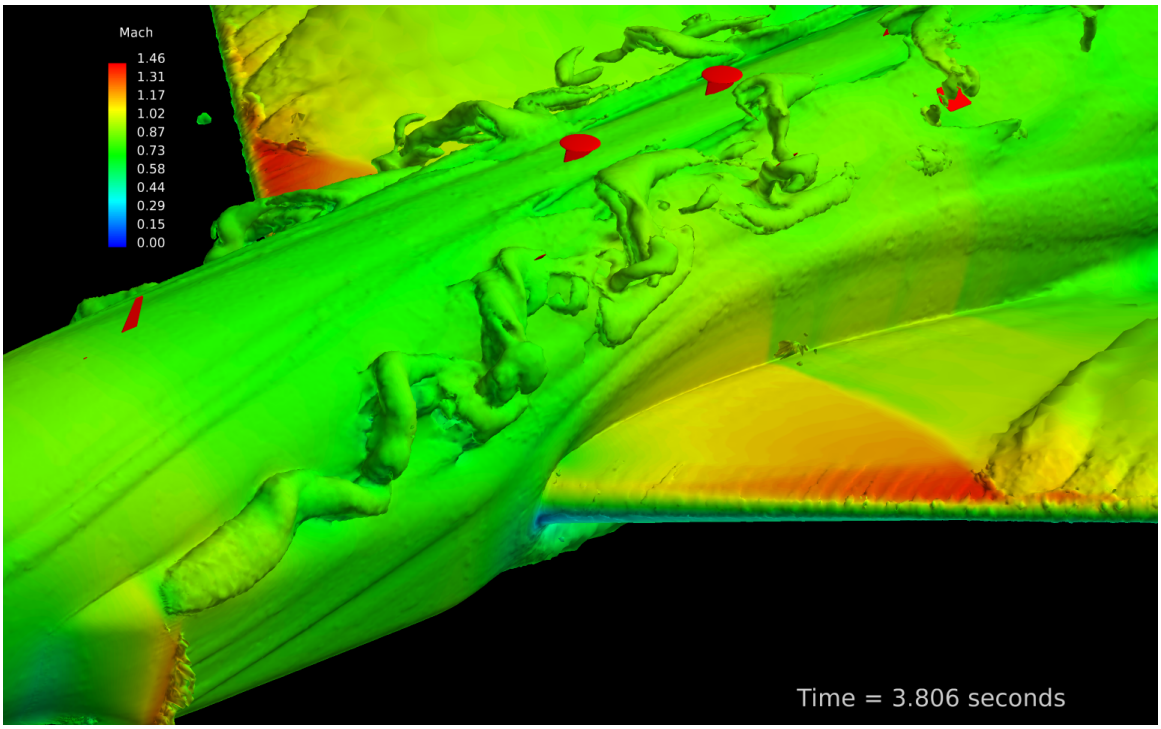


Figure 4.23: Rivet Joint with LCS (AoA = 8°) – vorticity of 100 Hz colored by Mach number for high angle of attack study (antennas colored by red shown for reference locations only – not included in solution)

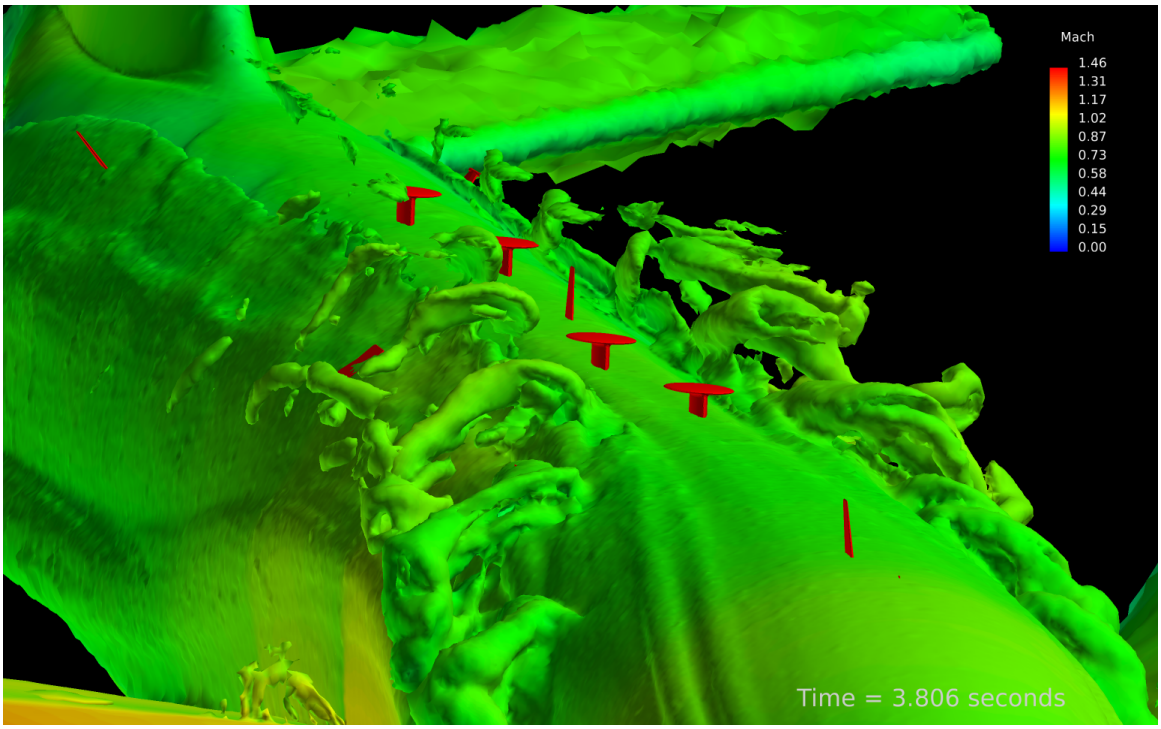


Figure 4.24: Rivet Joint with LCS (AoA = 8°) – vorticity of 100 Hz colored by Mach number for high angle of attack study (antennas colored by red shown for reference locations only – not included in solution)

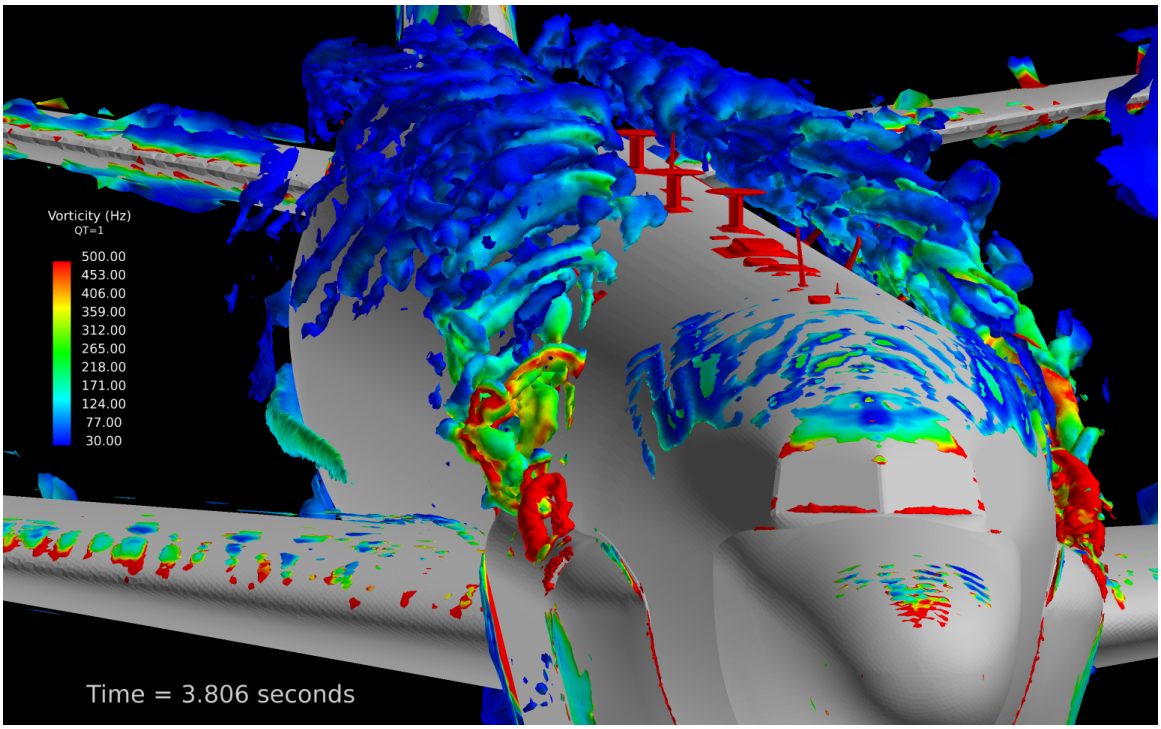


Figure 4.25: Rivet Joint with LCS (AoA = 8°) – Q-threshold of 1 colored by vorticity for high angle of attack study (antennas colored by red shown for reference locations only – not included in solution)

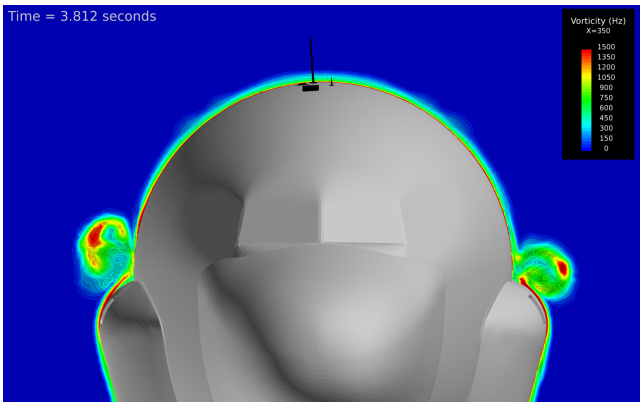


(a)

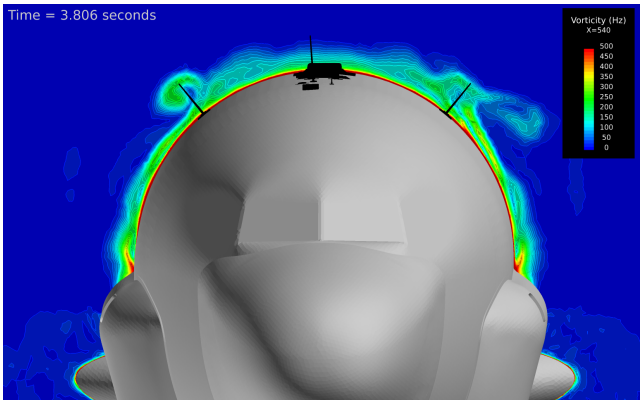


(b)

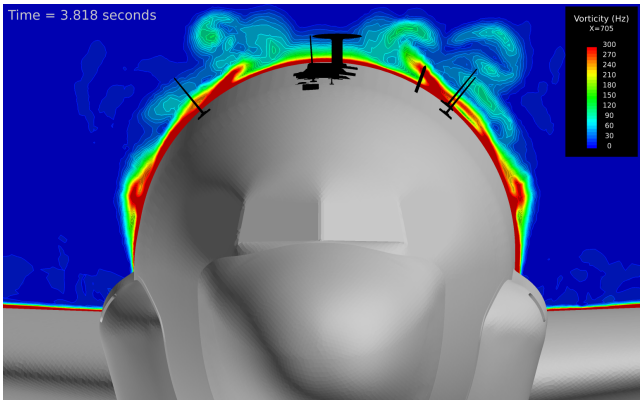


(c)

Figure 4.26: Rivet Joint with LCS (AoA = 8°) – time-dependent vortex structures for high angle of attack study at locations of (a) FD1 (b) UHF3 and UHF5 (c) UHF7 (antennas colored by black shown for reference locations only – not included in solution)

around UHF7 and this region has spread further towards the centerline. Additionally, the shear layers separating from the fuselage can now be seen in this region.

Examining the flow-field at high angle-of-attack, without the effect of the LCS exhaust, highlights some subtle differences between the Rivet Joint and Combat Sent. Figure 4.27 shows iso-surfaces of vorticity set at 100 Hz for the Rivet Joint while Figure 4.28 shows the same view of the Combat Sent. The extent of the separated shear layer is slightly larger for the Combat Sent than that of the Rivet Joint extending further towards the centerline. Also, it is difficult to see this in the given figures, but the separated shear layer is an unsteady phenomenon and travels laterally, shifting slightly back and forth.

Figures 4.29 and 4.30 display the streamlines originating from the LCS exhaust. Additionally, the origins of the streamlines impacting UHF3 and UHF7 are highlighted. Note how the streamlines for the Rivet Joint originating at the LCS exhaust are more focused on the location of UHF3 while for the Combat Sent, the streamlines are spread more between UHF3 and UHF7. It is difficult to determine if this is solely an artifact of extracting a snapshot from a time dependent flow or if the Rivet Joint has a tendency to draw the flow slightly closer towards the centerline than the Combat Sent. Also, note how the streamlines affecting the two antennas for the Combat Sent originate from the lower nose and traverse the region around the "chin" radome. This could account for some of these slight differences, but again it is difficult to confirm.

Once again, acoustic analysis was performed for the higher angle of attack cases with the resulting overall sound pressure level statistics recorded in Tables 4.5 and 4.6. As was seen with flight testing, these simulations confirmed the large dependency on angle of attack exhibited by the flow unsteadiness at the antenna locations. Without flow through the LCS, noise levels increased an average of 26.0% at the locations of UHF3/UHF5, 35.8% at UHF7, and 22.9% at the two SATCOM BF units with increasing angle of attack. Along the centerline of the fuselage, without flow through the LCS, noise levels increased an average of 21.5% at FD2, 32.6% at FD4, and 24.2%

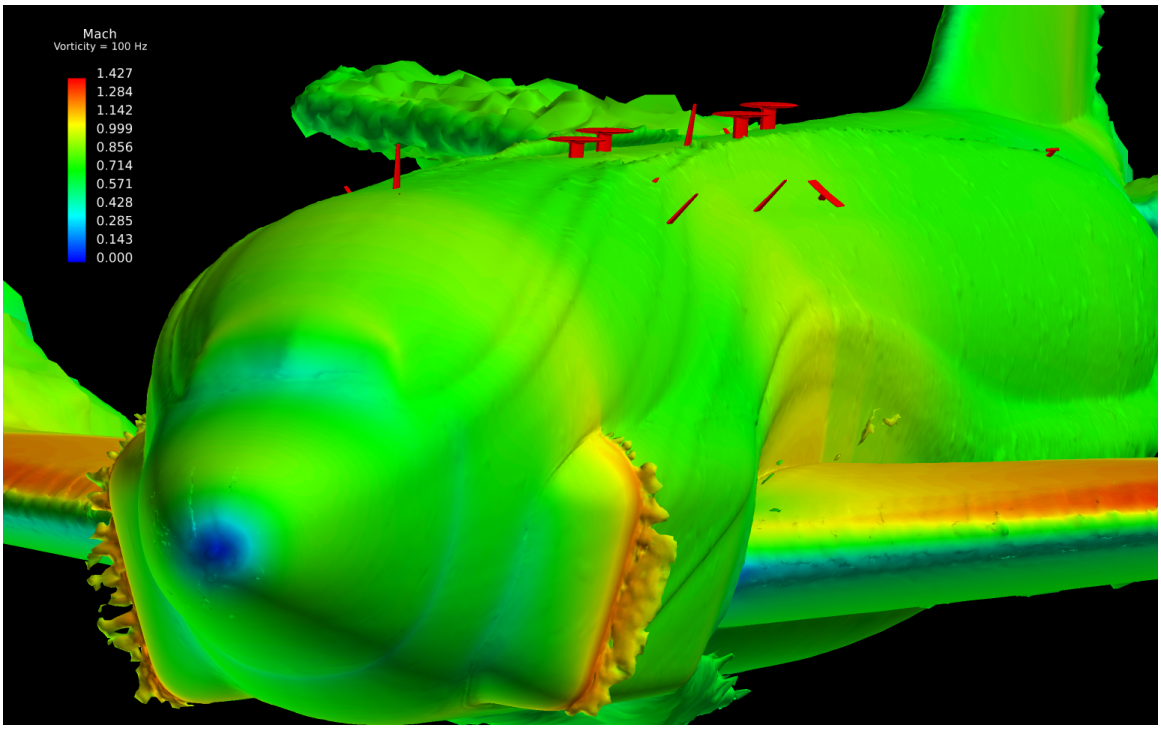


Figure 4.27: Rivet Joint without LCS (AoA = 8°) – vorticity of 100 Hz colored by Mach number for high angle of attack study (antennas colored by red shown for reference locations only – not included in solution)

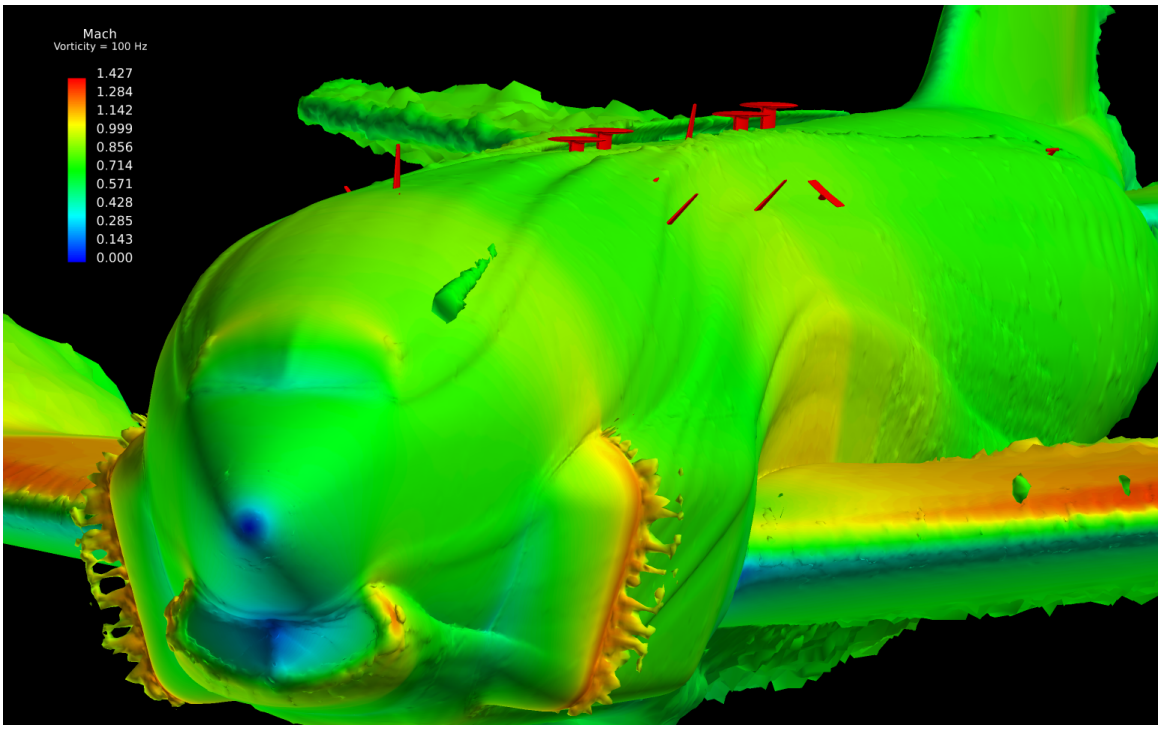


Figure 4.28: Combat Sent without LCS (AoA = 8°) – vorticity of 100 Hz colored by Mach number for high angle of attack study (antennas colored by red shown for reference locations only – not included in solution)

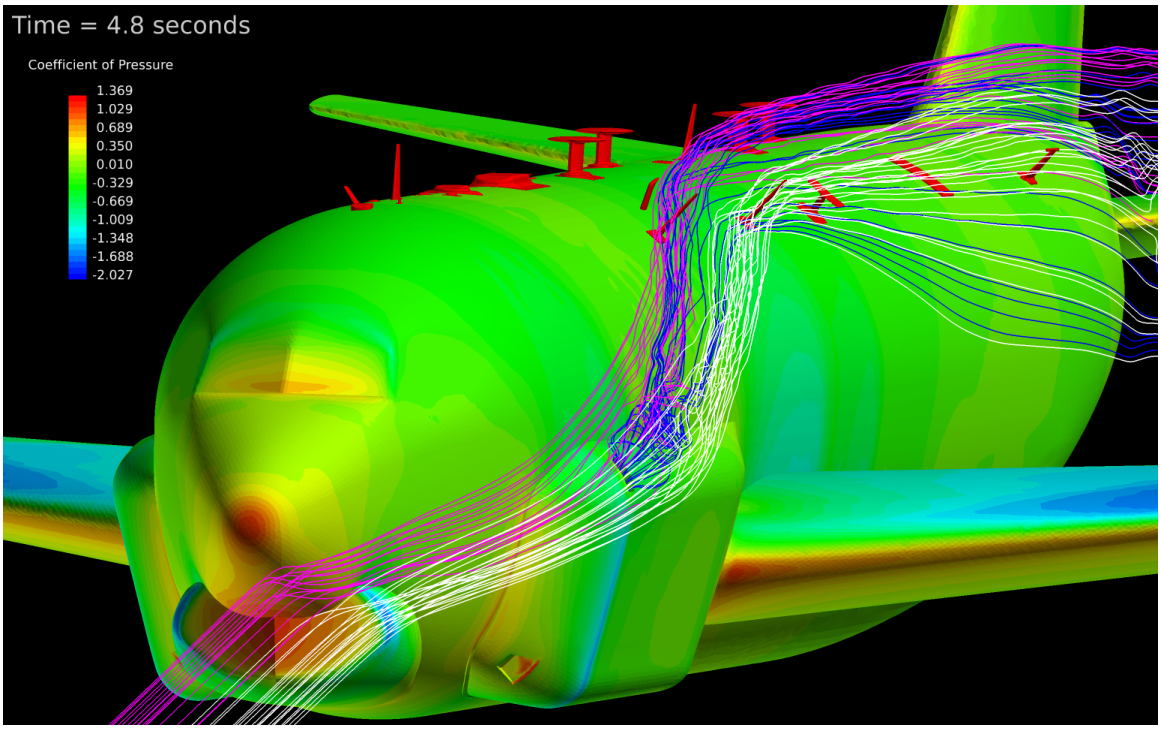


Figure 4.29: Combat Sent with LCS (AoA of 8°) – fuselage surface colored by coefficient of pressure with antennas colors specified by: *blue* streamlines originating from LCS exhaust; *pink* streamlines originating from plane at location of UHF3; *white* streamlines originating from plane at location of UHF7 (antennas colored by red shown for reference locations only – not included in solution)

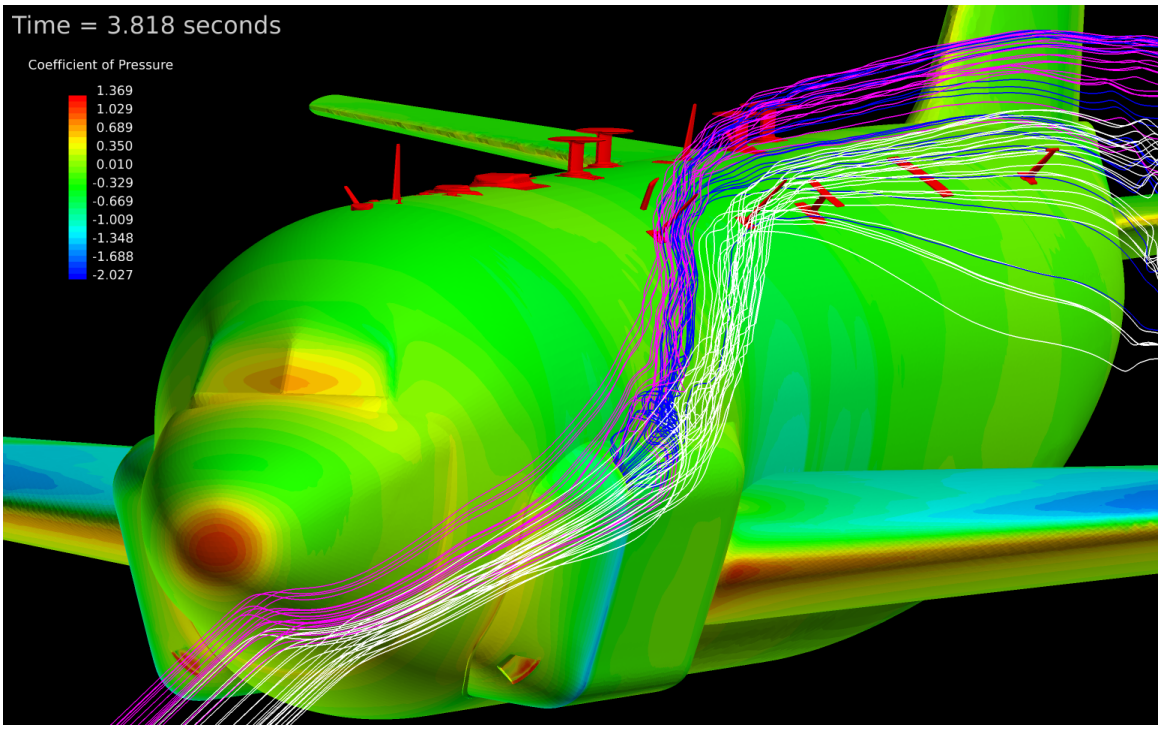


Figure 4.30: Rivet Joint with LCS (AoA of 8°) – fuselage surface colored by coefficient of pressure with antennas colors specified by: *blue* streamlines originating from LCS exhaust; *pink* streamlines originating from plane at location of UHF3; *white* streamlines originating from plane at location of UHF7 (antennas colored by red shown for reference locations only – not included in solution)

at UHF9 with increasing angle of attack. With flow through the cheeks, noise levels increased an average of 7.2% at UHF3/UHF5, 11.9% at UHF7, and 14.5% at the two SATCOM BF units with increasing angle of attack. Along the centerline of the fuselage, with flow through the LCS, noise levels actually decreased slightly at the location of FD2 by an average of 0.6%. While further along the fuselage, the noise levels increased by an average of 11.7% at FD4 and 18.6% at UHF9.

The UHF7 antenna location once again has higher mean OASPL values than observed at the locations of UHF3 and UHF5, but the standard deviation of OASPL at UHF7 drops drastically to 0.1166 dB at an AoA of 8 degrees from 2.9360 dB at an AoA of 4 degrees for the Combat Sent. A similar drop of 3.1376 dB to 0.3450 dB is observed for the Rivet Joint. This is reflected in Fig. 4.31 where the OASPL, although elevated, shows little variation with location along the antenna. This is

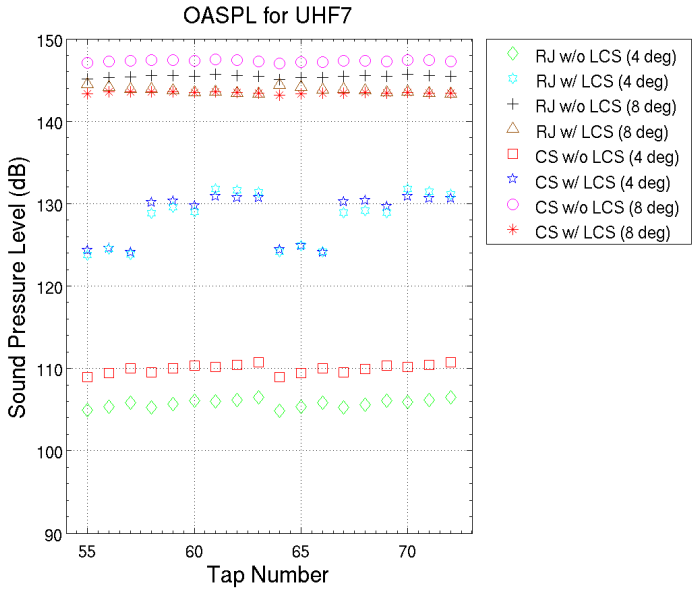


Figure 4.31: Comparison of overall sound pressure levels at location of UHF7 for angle of attack sensitivity study

reverse of what is observed at UHF3 and UHF5 where there is an average increase in standard deviation from 0.7006 dB to 2.7505 dB for the Combat Sent and from 0.4948 dB to 3.0088 dB for the Rivet Joint. This is illustrated in Figure 4.32. The decrease in standard deviation at the location of UHF7 could be due to the sheet of separated

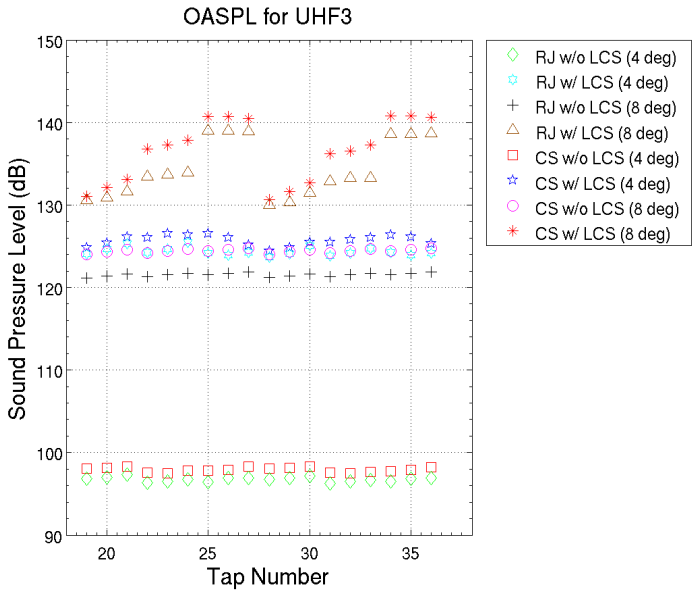


Figure 4.32: Comparison of overall sound pressure levels at location of UHF3 for angle of attack sensitivity study

flow raising the overall noise levels towards the root of the antenna. The exhaust structure is still impacting this area and thus the overall noise levels would still be expected to be high but the addition of the shear layer makes interpretation of this increased noise more complicated. The increase in standard deviation at the locations of UHF3 and UHF5 reflects the shift in the exhaust structure to this location further up along the fuselage.

Once again, stability problems were encountered when running the full unsteady N-S with DDES and solutions were not achieved with the configurations including antennas. In order to provide comparison, Euler solutions were computed for the configurations without flow through the LCS. Figure 4.33 shows the location of shock waves over the Combat Sent variant at an angle of attack of 8°. The higher angle of attack has increased both the strength and extent of the shock waves located on the central fuselage over the wings. The shock wave over the wing seems to be extended over the fuselage due to the presence of the JTT SATCOM antenna along the centerline as well as at UHF7 and the two SATCOM Beamformer units offset along the upper sides. There is a large region affected but it is important to point

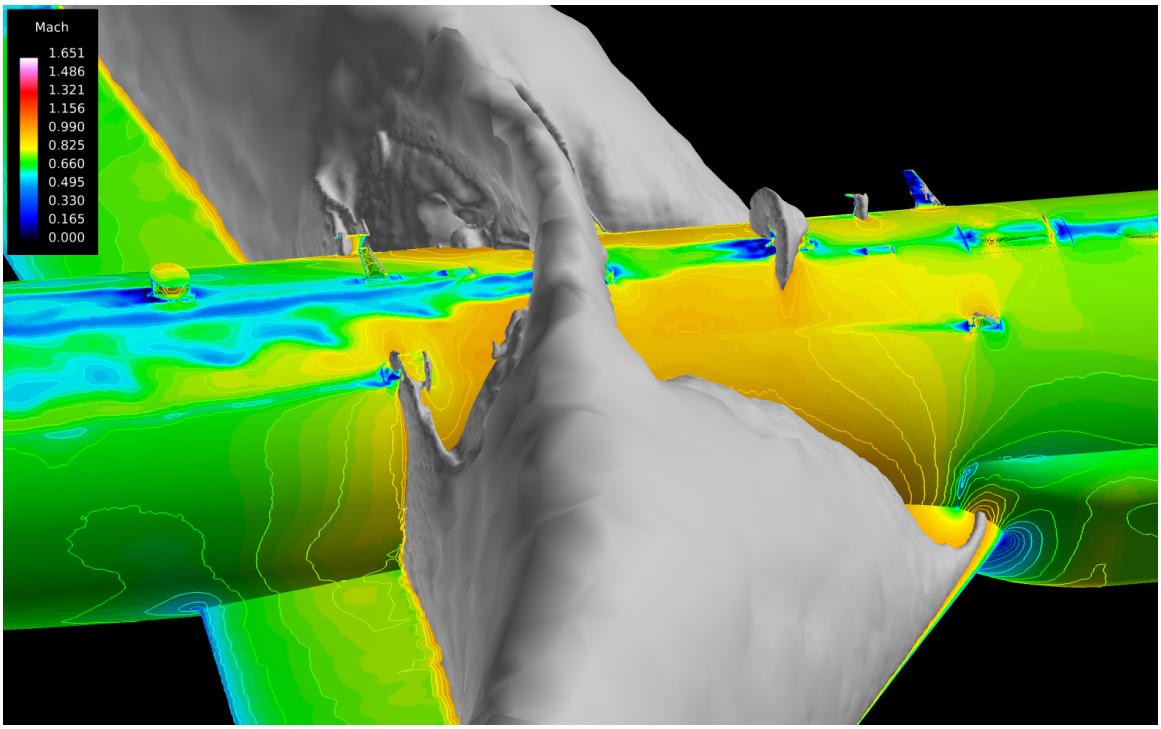


Figure 4.33: Combat Sent with antennas and without LCS – high angle of attack case showing central fuselage; fuselage and antenna surfaces colored by Mach number with Mach=1 iso-surfaces shown in gray (flow is going from right to left)

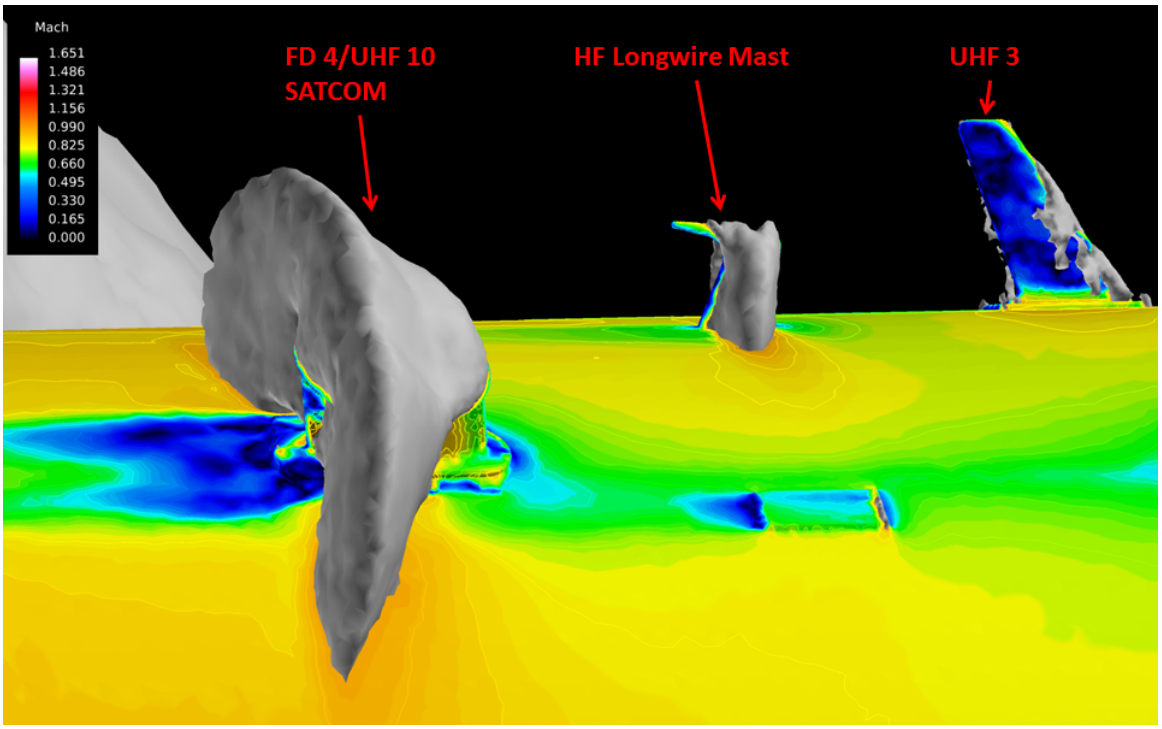


Figure 4.34: Combat Sent with antennas and without LCS – high angle of attack case showing FD4/UHF10 SATCOM and UHF3; fuselage and antenna surfaces colored by Mach number with Mach=1 iso-surfaces shown in gray (flow is going from right to left)

out that this shock wave is not very strong and thus does not cause significant flow separation. This is not the case forward of this location at UHF3 and UHF5 where strong shocks are encountered, causing significant amounts of flow separation on the inward facing surfaces as shown on Figure 4.34. This is also the case once again along the aft portion of the fuselage for the outward facing surface of FD1 as shown in Figure 4.35.

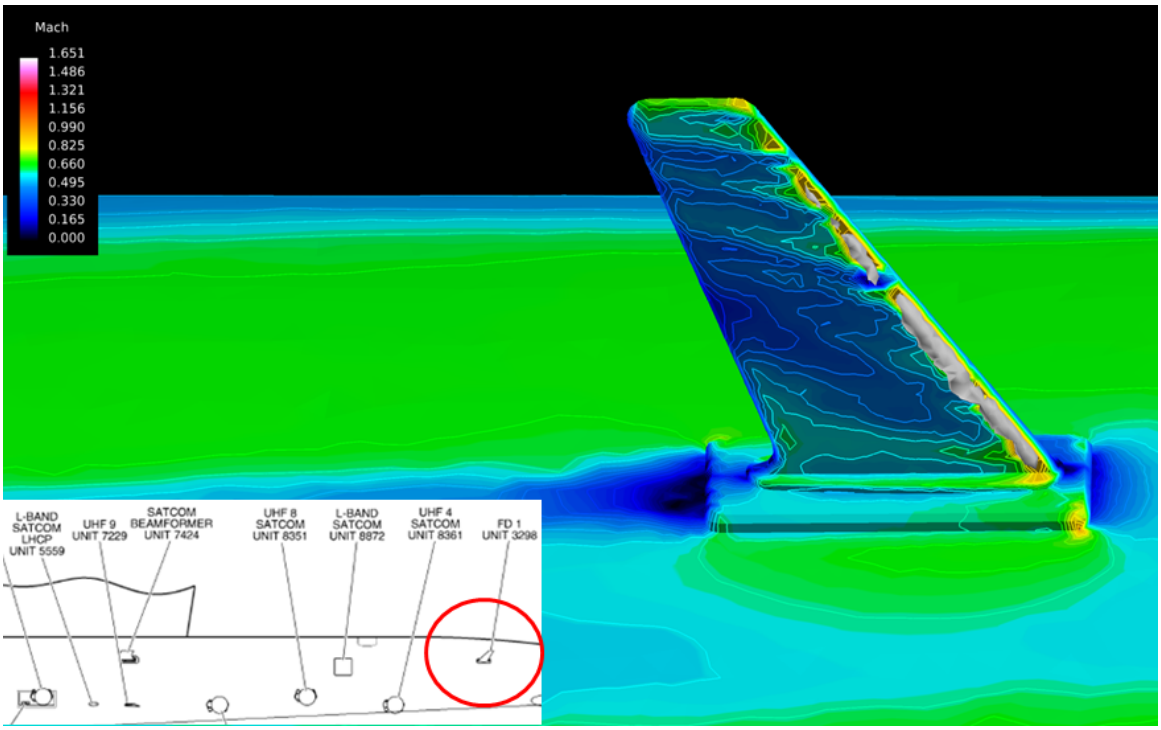


Figure 4.35: Combat Sent with antennas and without LCS – high angle of attack case showing FD1; fuselage and antenna surfaces colored by Mach number with Mach=1 iso-surfaces shown in gray (flow is going from right to left)

Figure 4.36 shows Mach number along the top of the fuselage for the two Euler solutions with antennas. Even with the higher angle of attack, there is not a very large difference here, although, there are certainly differences in the aft portion of the fuselage that should be investigated further.

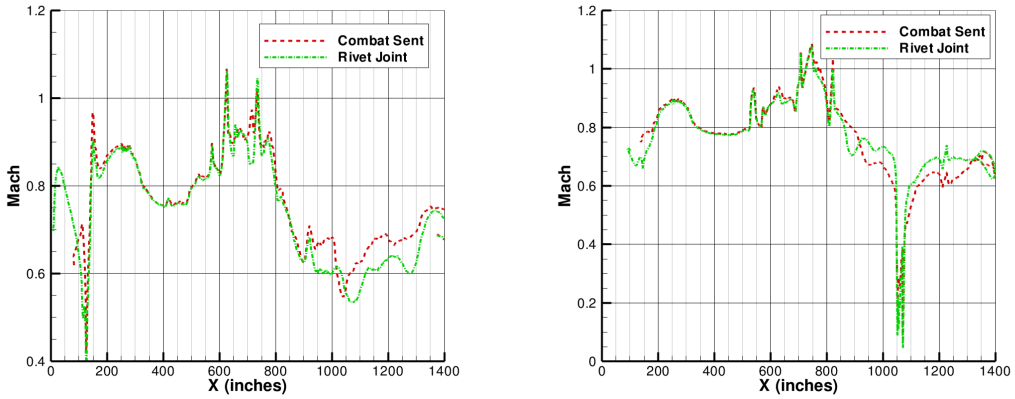


(a) (b)

Figure 4.36: Comparison of Mach number along fuselage for high angle of attack at (a) $Y = -20$" (b) $Y = -40$"

Table 4.5: Comparison of overall sound pressure levels at each antenna location for angle of attack sensitivity study - Rivet Joint

| Case | FD2 | | UHF3 | | UHF5 | |
|---|---|---|---|---|---|---|
| | $\overline{\text{OASPL}}$ | $\sigma_{\text{OASPL}}$ | $\overline{\text{OASPL}}$ | $\sigma_{\text{OASPL}}$ | $\overline{\text{OASPL}}$ | $\sigma_{\text{OASPL}}$ |
| RJ w/o LCS ($\alpha = 4°$) | 97.7222 | 0.5458 | 96.7519 | 0.2943 | 97.3516 | 0.3867 |
| RJ w/ LCS ($\alpha = 4°$) | 130.4130 | 1.5892 | 124.3813 | 0.5021 | 124.5753 | 0.4874 |
| RJ w/o LCS ($\alpha = 8°$) | 119.7014 | 0.0994 | 121.5563 | 0.2167 | 121.9208 | 0.2239 |
| RJ w/ LCS ($\alpha = 8°$) | 130.2674 | 0.9451 | 134.3416 | 3.4480 | 135.1807 | 2.5696 |
| **Case** | **UHF7** | | **UHF9** | | **FD1** | |
| | $\overline{\text{OASPL}}$ | $\sigma_{\text{OASPL}}$ | $\overline{\text{OASPL}}$ | $\sigma_{\text{OASPL}}$ | $\overline{\text{OASPL}}$ | $\sigma_{\text{OASPL}}$ |
| RJ w/o LCS ($\alpha = 4°$) | 105.7458 | 0.4922 | 112.1371 | 0.1488 | 106.4271 | 0.2398 |
| RJ w/ LCS ($\alpha = 4°$) | 128.2773 | 3.1376 | 120.4007 | 0.3920 | 124.5243 | 0.6708 |
| RJ w/o LCS ($\alpha = 8°$) | 145.4349 | 0.1729 | 142.7007 | 0.1039 | 130.0249 | 0.3608 |
| RJ w/ LCS ($\alpha = 8°$) | 143.7697 | 0.3450 | 143.9964 | 0.1669 | 132.7351 | 0.6339 |
| **Case** | **FD3** | | **FD4** | | **JTT** | |
| | $\overline{\text{OASPL}}$ | $\sigma_{\text{OASPL}}$ | $\overline{\text{OASPL}}$ | $\sigma_{\text{OASPL}}$ | $\overline{\text{OASPL}}$ | $\sigma_{\text{OASPL}}$ |
| RJ w/o LCS ($\alpha = 4°$) | 105.7182 | 0.2619 | 99.4128 | 0.3896 | 108.5129 | 0.8598 |
| RJ w/ LCS ($\alpha = 4°$) | 124.5579 | 1.1737 | 116.3119 | 0.5445 | 118.5252 | 0.4647 |
| RJ w/o LCS ($\alpha = 8°$) | 129.2534 | 0.2785 | 132.7907 | 1.1272 | 144.1172 | 0.0805 |
| RJ w/ LCS ($\alpha = 8°$) | 132.7751 | 0.4076 | 135.6693 | 0.9409 | 143.1126 | 0.0538 |
| **Case** | **UHF6** | | **UHF8** | | **BF7421** | |
| | $\overline{\text{OASPL}}$ | $\sigma_{\text{OASPL}}$ | $\overline{\text{OASPL}}$ | $\sigma_{\text{OASPL}}$ | $\overline{\text{OASPL}}$ | $\sigma_{\text{OASPL}}$ |
| RJ w/o LCS ($\alpha = 4°$) | 108.3679 | 0.1957 | 107.2458 | 0.1416 | 115.0891 | 0.3328 |
| RJ w/ LCS ($\alpha = 4°$) | 116.7187 | 0.4746 | 115.5929 | 0.5673 | 127.9741 | 0.5829 |
| RJ w/o LCS ($\alpha = 8°$) | 139.0597 | 0.3320 | 134.4895 | 0.3487 | 142.1399 | 0.2406 |
| RJ w/ LCS ($\alpha = 8°$) | 141.6091 | 0.3429 | 136.7965 | 0.3646 | 144.1675 | 0.2535 |
| **Case** | **BF7424** | | | | | |
| | $\overline{\text{OASPL}}$ | $\sigma_{\text{OASPL}}$ | | | | |
| RJ w/o LCS ($\alpha = 4°$) | 115.1489 | 0.4120 | | | | |
| RJ w/ LCS ($\alpha = 4°$) | 125.1631 | 0.3123 | | | | |
| RJ w/o LCS ($\alpha = 8°$) | 146.2291 | 0.2396 | | | | |
| RJ w/ LCS ($\alpha = 8°$) | 147.2532 | 0.2707 | | | | |

Table 4.6: Comparison of overall sound pressure levels at each antenna location for angle of attack sensitivity study - Combat Sent

| **Case** | **FD2** | | **UHF3** | | **UHF5** | |
|---|---|---|---|---|---|---|
| | $\overline{\textbf{OASPL}}$ | $\sigma_{\textbf{OASPL}}$ | $\overline{\textbf{OASPL}}$ | $\sigma_{\textbf{OASPL}}$ | $\overline{\textbf{OASPL}}$ | $\sigma_{\textbf{OASPL}}$ |
| CS w/o LCS ($\alpha = 4°$) | 99.4718 | 0.5778 | 97.9283 | 0.2888 | 98.9776 | 0.2755 |
| CS w/ LCS ($\alpha = 4°$) | 133.0935 | 1.6371 | 125.7313 | 0.6271 | 124.7049 | 0.7740 |
| CS w/o LCS ($\alpha = 8°$) | 119.8875 | 0.0454 | 124.4439 | 0.2293 | 124.8502 | 0.2902 |
| CS w/ LCS ($\alpha = 8°$) | 131.6600 | 1.9763 | 136.5149 | 3.7607 | 129.4718 | 1.7402 |
| **Case** | **UHF7** | | **UHF9** | | **FD1** | |
| | $\overline{\textbf{OASPL}}$ | $\sigma_{\textbf{OASPL}}$ | $\overline{\textbf{OASPL}}$ | $\sigma_{\textbf{OASPL}}$ | $\overline{\textbf{OASPL}}$ | $\sigma_{\textbf{OASPL}}$ |
| CS w/o LCS ($\alpha = 4°$) | 109.9546 | 0.5430 | 116.7263 | 0.1122 | 112.0272 | 0.2581 |
| CS w/ LCS ($\alpha = 4°$) | 128.4139 | 2.9360 | 120.3070 | 0.5232 | 123.8806 | 0.5818 |
| CS w/o LCS ($\alpha = 8°$) | 147.3201 | 0.1254 | 141.3576 | 0.0661 | 129.4690 | 0.2568 |
| CS w/ LCS ($\alpha = 8°$) | 143.4452 | 0.1166 | 141.4374 | 0.2457 | 130.4475 | 1.0376 |
| **Case** | **FD3** | | **FD4** | | **JTT** | |
| | $\overline{\textbf{OASPL}}$ | $\sigma_{\textbf{OASPL}}$ | $\overline{\textbf{OASPL}}$ | $\sigma_{\textbf{OASPL}}$ | $\overline{\textbf{OASPL}}$ | $\sigma_{\textbf{OASPL}}$ |
| CS w/o LCS ($\alpha = 4°$) | 112.8744 | 0.1453 | 102.4512 | 0.4349 | 113.4059 | 0.7915 |
| CS w/ LCS ($\alpha = 4°$) | 124.2033 | 0.6710 | 117.5622 | 0.5009 | 118.4125 | 0.4853 |
| CS w/o LCS ($\alpha = 8°$) | 129.7881 | 0.2234 | 135.0259 | 0.9675 | 143.5146 | 0.0730 |
| CS w/ LCS ($\alpha = 8°$) | 129.7982 | 0.5283 | 125.5034 | 0.7512 | 138.4412 | 0.4859 |
| **Case** | **UHF6** | | **UHF8** | | **BF7421** | |
| | $\overline{\textbf{OASPL}}$ | $\sigma_{\textbf{OASPL}}$ | $\overline{\textbf{OASPL}}$ | $\sigma_{\textbf{OASPL}}$ | $\overline{\textbf{OASPL}}$ | $\sigma_{\textbf{OASPL}}$ |
| CS w/o LCS ($\alpha = 4°$) | 113.0693 | 0.1557 | 112.1709 | 0.0820 | 118.9913 | 0.3024 |
| CS w/ LCS ($\alpha = 4°$) | 118.1720 | 0.6739 | 118.0898 | 0.6207 | 126.9883 | 0.6064 |
| CS w/o LCS ($\alpha = 8°$) | 138.4543 | 0.2857 | 133.5607 | 0.3082 | 143.8958 | 0.2467 |
| CS w/ LCS ($\alpha = 8°$) | 137.2938 | 0.2512 | 134.3592 | 0.2919 | 144.0621 | 0.3209 |
| **Case** | **BF7424** | | | | | |
| | $\overline{\textbf{OASPL}}$ | $\sigma_{\textbf{OASPL}}$ | | | | |
| CS w/o LCS ($\alpha = 4°$) | 119.3995 | 0.3103 | | | | |
| CS w/ LCS ($\alpha = 4°$) | 124.4288 | 0.5395 | | | | |
| CS w/o LCS ($\alpha = 8°$) | 143.5671 | 0.2756 | | | | |
| CS w/ LCS ($\alpha = 8°$) | 142.1717 | 0.2226 | | | | |

# V. Conclusions

An investigation was undertaken using computational fluid dynamics analysis techniques assessing the external aerodynamics of two variants out of the RC-135 family of reconnaissance aircraft. The motivation behind this research stems from problems with the structural integrity of certain antennas on the RC-135V/W Rivet Joint that previous research has related back to the installation of a new cooling system in the cheek fairings of this aircraft. The RC-135U Combat Sent has been flying since the late 1990s with the same cooling system and no structural problems were encountered. The intention of this study was to better understand the external aerodynamic differences between these two variants and, furthermore, to better understand the complexities inherent to these highly modified aircraft.

In Chapter II, the complexities associated with highly turbulent and separated flow encountered in the transonic flow regime were discussed along with an overview of the analysis techniques necessary to perform this investigation. The previous research applied to the problems with the Rivet Joint has been limited to flight testing in addition to some on-going CFD investigations by AFRL. Analysis of flight test data confirmed the relationship between the LCS exhaust flow and antenna buffeting at UHF3, UHF5, and UHF7. Additionally, antenna buffeting was also observed with the Combat Sent variant and, therefore, more research was deemed necessary in order to understand why the Rivet Joint is encountering more problems.

The methodology applied to this research was presented in Chapter III. This chapter outlined the grid generation techniques, how the simulations were set up, as well as the individualized approach for each study. A grid refinement and time step sensitivity study was set up such that three different levels of grid refinement and six different time steps could be compared in order to provide verification of the choice of grid and time step used throughout the investigation. In order to provide validation, and since flight test data was available, a flight test condition was chosen to compare to using acoustic techniques. With verification and validation techniques laid out, the approach to performing the baseline comparisons was introduced with the intention

of comparing all configurations at typical maximum range cruise conditions. Two studies are then proposed, altering angle of attack and mass flow rate in order to determine the sensitivity to these parameters with all other variables constant. The results from the various studies were presented in Chapter IV.

Due to stability issues encountered on both the coarse and fine grids, the "steepest descent" approach to the grid resolution and time step sensitivity study had to be altered slightly. Only one solution was computed on each of the coarse and fine grids, while four different time steps were compared on the medium grid. Fortunately, these two solutions on the other grids confirmed that the choice of the medium grid would provide adequately accurate answers while making the most efficient use of the computational resources available.

The comparison against flight test data was inconclusive. A direct comparison was not possible due to stability problems encountered with the antenna configurations and thus only the models without antennas were available for comparison. Despite this, the configuration up to the location of UHF3 and UHF5 provides good comparison to flight test, especially in the region directly aft of the LCS exhaust, and thus acoustics could be compared along the upper cheek fairing with a reasonable degree of accuracy. Computed frequencies in the vicinity of the cooling system exhaust were in the same range as those observed in flight test, although the overall sound pressure levels were under predicted. This could be a function of differences in the means of calculating SPL between that of flight test and that of the computational analysis. Further investigation into OASPL as a means of validation is needed, but relative comparison can still be made between the different cases presented in this study.

The flow structure of the cooling system exhaust plume was examined in depth, with highly turbulent structures observed traveling along the fuselage wall up towards the locations of UHF3/UHF5 and UHF7. For the baseline cases, the exhaust plume directly impacted UHF7 resulting in higher experienced noise levels than that seen at

UHF3 or UHF5. Flow impacting these antennas originated along the side of the nose region traveling near or directly in the path of the exhaust plume and thus perturbing the flow before impacting the location of the antennas. Acoustic analysis confirmed the large increase in sound pressure levels at both UHF3/UHF5 and UHF7 and overall sound pressure level was found to decrease with distance from the exhaust plume source. Surprisingly, an even higher increase in sound pressure level was observed along the centerline at FD2 located just aft of the longitudinal station of the LCS exhaust outlet. It seems that flow through the LCS has more of a global effect on the flow-field than previously thought, causing pressure oscillations along the upper fuselage that affects the boundary layer and thus elevates the noise along the centerline of the fuselage. Despite this finding, this does not necessarily mean that this type of noise will excite antenna buffeting. In the baseline cases, the oscillations at UHF7 are much more likely to excite antenna buffeting with the higher noise levels at the location of the antenna tip being manifested as higher standard deviation among the taps at the location of the antenna. Additionally, it was found that there is very little acoustic difference between the two variants with the Combat Sent showing less than 5% increase in noise levels in most locations with no flow through the LCS and even less of a difference with flow turned on. Solutions computed using the Euler equations demonstrated shock-induced separation on UHF3 and UHF5. When combined with exhaust plume interaction, it is reasonable to expect increased levels of buffeting, although more research is needed in order to support this claim.

The flow-field proved to be fairly insensitive to varying mass flow rates, although, the mass flow rate did seem to shift the exhaust plume slightly as well as provide an enhanced focus with the higher mass flow rates. It seems that the mass flow rate could be used to fine tune the location of the plume, where changing the mass flow rate would significantly affect the noise levels as the plume shifts and impacts the antennas just right. Also, it was observed that the plume generated over the Rivet Joint was more focused with more of the energy traveling up the fuselage towards the antennas while the Combat Sent's exhaust plume was more spread out. The more focused

plume of the Rivet Joint did seem to miss the UHF7 antenna just slightly, which could account for the slightly lower noise levels observed in the computed cases. It is possible, if the right conditions are chosen, that the more focused plume impacting UHF3 and UHF5 could induce increased antenna buffeting for the Rivet Joint. In general, the mass flow does not have a very large effect on the location of the exhaust plume only shifting it slightly, wherein angle of attack had the largest effect on the flow structures.

The higher angle of attack cases demonstrated a strong correlation with the location of the turbulent flow structures. With increasing angle of attack, not only did the exhaust plume shift further up along the fuselage towards the centerline, but also resulted in a separated shear layer developing increasing noise levels along the sides of the top of the fuselage from the location of the wings aft to the vertical tail. The extent of this shear layer was greater on that of the Combat Sent than that of the Rivet Joint. In the cases examined, this allowed the exhaust plume to engulf both UHF3/UHF5 and UHF7 antennas increasing both mean and standard deviation of OASPL at UHF3 and UHF5. Additionally, Euler solutions confirmed the existence of shock waves forming over the upper fuselage and covering a larger region, including even stronger shocks on UHF3 and UHF5 causing the entire inner surface of each to separate. Additionally, streamlines impacting the antennas of interest originated from the lower nose region of both variants causing additional variation in the solution at each antenna. Acoustic analysis showed that standard deviation of OASPL increased drastically at UHF3 and UHF5, with the Rivet Joint encountering slightly higher levels than the Combat Sent.

The results gathered from this investigation provide validation of the flight test conclusions, confirming the high sensitivity to angle of attack and providing a direct link between observed acoustic levels and the cooling system exhaust. Much was learned about the flow-field and how it was affected by a turbulent disturbance such as that of the cooling system exhaust plume. Sensitivity to mass flow rate was tested and found that there is, in reality, little sensitivity to changes in mass flow rate.

This would have been difficult to determine from flight testing as there are too many variables in that environment. Other than subtle differences observed between the Rivet Joint and Combat Sent variants, there is not a significant difference in the flow-field along the upper fuselage between these two variants. It is possible that the increase in structural problems with the Rivet Joint over that of the Combat Sent could be due to differences in operational flight regimes, which should be considered in any future work.

### *5.1 Recommendations for Future Work*

This investigation started out with ambitious goals. Unsteady simulations utilizing DDES on a full aircraft of this size would not have been possible a couple years ago, let alone ten years ago, previous to the installation of the Raptor supercomputer by AFRL DSRC. With the results gathered, despite not reaching the goals originally set, much was learned about the flow features inherent to this type of a problem. There is not a lot of information available on simulations of this type, since this has only recently become possible, and the methodologies and data presented in this thesis lay the foundation for future endeavors of this nature.

Specifically, for the problem pertaining to the RC-135 family of aircraft, simulations need to be run with antennas included in the flow-field. The stability issues encountered in this investigation should not be as much of a problem in the next version of Kestrel. The current problems with Kestrel version 2.1.2 stem back to issues with the current version of kAVUS, relating, specifically, to the Jacobian terms, boundary conditions, and turbulence models. Steady state accuracy is not affected by these problems, but unsteady solution convergence is affected, with a strong dependence on the quality of the mesh and flow conditions. Version 2.2 will be released shortly addressing these issues and future work should include a re-evaluation of the cases presented here with the updated version of Kestrel. [36] If this does not prove to be the case, then one should attempt to run these simulations using the original AVUS solver as stability does not seem to be as much of a problem with that software.

Additionally, when running simulations with antennas in the flow-field, it would be good to be able to extract forces on these antennas and attempt a correlation to derived acoustic spectrum.

A more in depth grid resolution and time step sensitivity study should be undertaken. Stability was a major problem in this investigation and, although results were gathered on the coarse and fine grid, the solutions were unstable and may have affected the accuracy of the extracted data. Additionally, studies examining how the temporal damping and number of Newton sub-iterations affect the solution should be performed. This will determine if the unsteady nature of this flow-field is adequately being captured.

With the high sensitivity to angle of attack, it would be good to vary this angle of attack in smaller increments. Find the conditions that locate the exhaust plume directly in line with UHF3 and UHF5 and then do the same with UHF7. With this in mind, it would also be good to correlate to changes in flight conditions such as altitude and air speed. Is there a specific flight envelope where the problems are amplified? Does the more focused exhaust plume of the Rivet Joint translate to greater pressure fluctuations at the location of the antenna?

Ultimately, the goal is to create a tool that can be used by Big Safari and L-3 Communications to better understand how changes to the configuration affect the flow-field around the aircraft. This way, better decisions can be made regarding antenna placement and changes can be implemented before problems present themselves. This will require building a full configuration of the aircraft including all antennas on the top and bottom of the fuselage. Note that this will levy increasing computational demands as the configuration is made more complex. On the topic of configuration control and grid generation, it may be beneficial to increase the focus region such that a larger distance from the fuselage is covered. This will allow for the full extent of the exhaust plume to be examined and to determine is this has an effect on the immediate flow-field around the fuselage or not. There is still much to be done in

order to be able to provide a useful tool, but this research has laid the foundation that should be expanded upon with future research.

# *Appendix A. Summary of utilized computational resources*

This appendix provides a summary of the computational resources utilizes in the course of this investigation. All simulations were run on the AFRL DSRC's Cray XE6 "Raptor" supercomputer. Some of the computational cost statistics given are merely estimates, wherein statistics for partial cases may of been lost due to a simulation failing. Also, many of the cases, for the grid and time step sensitivity study specifically, were started from previously existing state and therefore do not provide the full run times. To indicate where this is the case a "+" is added to the estimate.

Additionally, for some of the simulations and specifically for some of the mass flow rate sensitivity study cases, a slightly different approach was taken, wherein the steady-state portion was extended while gradually lowering the temporal damping. This tended to increase stability while helping to reach a transient-free point quicker before switching to unsteady DDES and initializing the data collection portion.

The simulations reported below used a total of 2,124,944 CPU-hours. This amounts to a wall time of approximately 1,664 hours (≈69.3 days). This was only a part of the overall DSRC time used with a total of 3,393,639 CPU-hours expended. Many resources were spent attempting to stabilize the antenna configurations such that an unsteady DDES solution could be achieved, but the stability problems encountered prevented these cases from ultimately being usable. This is in addition to a number of hours expended in determining the correct set of parameters that will provide a stable and accurate answer for all of the other configurations.

Table A.1: Computational cost of baseline cases

| Case | Number of Cells | Number of Cores | Wall Time (hrs) | CPU Time (hrs) | Number of Iterations | Time per Iteration (sec) |
|---|---|---|---|---|---|---|
| RJ Clean w/o LCS | 45,643,478 | 1024 | 77.9 | 79,758 | 19,000 | 14.8 |
| RJ Clean w/ LCS | 46,381,570 | 1024 | 83.6 | 85,584 | 19,000 | 15.8 |
| RJ Antennas w/o LCS (Euler) | 31,294,089 | 1024 | 12.7 | 13,006 | 14,000 | 3.27 |
| CS Clean w/o LCS | 43,326,124 | 1024 | 73.4 | 75,152 | 19,000 | 13.9 |
| CS Clean w/ LCS | 44,065,743 | 1024 | 91.7 | 93,892 | 19,000 | 17.4 |
| CS Antennas w/o LCS (Euler) | 29,764,171 | 1024 | 12.2 | 12,488 | 14,000 | 3.14 |
| | | | 351.5 | 359,880 | | |

Table A.2: Computational cost of flight test comparison cases

| Case | Number of Cells | Number of Cores | Wall Time (hrs) | CPU Time (hrs) | Number of Iterations | Time per Iteration (sec) |
|---|---|---|---|---|---|---|
| RJ Clean w/o LCS | 45,643,478 | 1024 | 74.5 | 76,308 | 19,000 | 14.1 |
| RJ Clean w/ LCS | 46,381,570 | 1024 | 62.2 | 63,693 | 19,000 | 11.8 |
| | | | 136.7 | 140,001 | | |

Table A.3: Computational cost of mass flow sensitivity study cases

| Case | Number of Cells | Number of Cores | Wall Time (hrs) | CPU Time (hrs) | Number of Iterations | Time per Iteration (sec) |
|---|---|---|---|---|---|---|
| RJ (161 lbm/min) | 46,381,570 | 1024 | 72.2 | 73,946 | 19,000 | 13.7 |
| RJ (247 lbm/min) | 46,381,570 | 1024 | 61.1 | 62,588 | 23,000 | 9.56 |
| RJ (350 lbm/min) | 46,381,570 | 1024 | 49.6 | 50,805 | 23,000 | 7.77 |
| CS (161 lbm/min) | 44,065,743 | 1024 | 61.8 | 63,256 | 23,000 | 9.67 |
| CS (247 lbm/min) | 44,065,743 | 1024 | 67.1 | 68,710 | 23,000 | 10.5 |
| CS (350 lbm/min) | 44,065,743 | 1024 | 58.9 | 60,326 | 23,000 | 9.22 |
| | | | 370.7 | 379,631 | | |

Table A.4: Computational cost of high angle-of-attack cases

| Case | Number of Cells | Number of Cores | Wall Time (hrs) | CPU Time (hrs) | Number of Iterations | Time per Iteration (sec) |
|---|---|---|---|---|---|---|
| RJ Clean w/o LCS | 45,643,478 | 1,024 | 75.8 | 77,663 | 19,000 | 14.4 |
| RJ Clean w/ LCS | 46,381,570 | 1,024 | 76.1 | 77,971 | 20,000 | 13.7 |
| RJ Antennas w/o LCS (Euler) | 31,294,089 | 1024 | 13.1 | 13,437 | 14,000 | 3.37 |
| CS Clean w/o LCS | 43,326,124 | 1,024 | 72.5 | 74,240 | 19,000 | 13.7 |
| CS Clean w/ LCS | 44,065,743 | 1,024 | 63.0 | 64,532 | 21,000 | 10.8 |
| CS Antennas w/o LCS (Euler) | 29,764,171 | 1,024 | 12.2 | 12,477 | 14,000 | 3.14 |
| | | | 312.7 | 320,320 | | |

Table A.5: Computational cost of grid refinement and time step sensitivity study cases

| Case | Number of Cells | Number of Cores | Wall Time (hrs) | CPU Time (hrs) | Number of Iterations | Time per Iteration (sec) |
|---|---|---|---|---|---|---|
| P1M | 44,065,743 | 1,024 | 12.9+ | 13,185+ | 3,125 | 14.9 |
| P2M | 44,065,743 | 1,024 | 16.9+ | 17,268+ | 5,250 | 11.6 |
| P3C | 32,285,697 | 1,024 | 16.8+ | 17,170+ | 5,500 | 11.0 |
| P3M | 44,065,743 | 1,024 | 35.2+ | 36,007+ | 8,500 | 14.9 |
| P5F | 118,018,603 | 2,048 (1,024) | 230.7+ | 472,474+ | 21,130 | 39.3 |
| P6F | 118,018,603 | 2,048 (1,024) | 180.2+ | 369,008+ | 20,011 | 32.4 |
| | | | 492.7+ | 925,112+ | | |

# *Appendix B. Summary of solver settings*

This appendix provides a summary of the flow solver settings applied within Kestrel. Parameter settings are give for both the initialization phase and for the values that are transitioned into prior to the data collection phase.

Table B.1: kAVUS Inputs

| **Input Parameter** | **Initialization Setting** | **Data Collection Setting** |
|---|---|---|
| Equation Set | Turbulent N-S | |
| Inviscid Flux | Gottlieb and Groth | |
| Turbulence Model | Spalart-Allmaras | DDES |
| Turbulence Wall | No | |
| Spatial Accuracy | Second-Order | |
| Temporal Accuracy | First-Order | Second-Order |
| Fixed Sweeps | No | |
| Max Sweeps | 64-128 | |
| Sweeps Convergence Criteria | 1.0e-8 | |
| Temporal Damping Coeff (Adv) | 0.8-1.0 | 0.3-0.4 |
| Temporal Damping Coeff (Diff) | 1/10 of Temporal Damping Coeff (Adv) | |
| Subiterations | 2 | 4 |
| Matrix Scheme | Gauss-Seidel | |
| Limiter Type | Original AVUS | |
| Least Squares Type | Weighted | |
| Theta | 1.0 | |
| Gradient Type | Non-conservative | |
| Stencil Type | Original | |
| Wall Accuracy | Use spatial accuracy | |
| Enable Gravity | No | |
| Relaxation | 0.7 | |
| Solution Update | Limited | |
| Solution Average | No | |
| Time Stepping Scheme | Local | Global Specified |
| Ramp CFL | Yes | n/a |
| Ramp CFL Iterations | 500-2000 | n/a |
| Start CFL | 100 | n/a |
| CFL | 1,000,000 | n/a |

# *Appendix C. Sound pressure levels extracted at all tap locations*

This appendix contains the calculated overall sound pressure levels at all tap locations. The baseline study is presented in Figures C.1, C.2, and C.3; mass flow rate sensitivity study is presented in Figures C.4, C.5, and C.6; and the angle of attack sensitivity study is presented in Figures C.7, C.8, and C.9.

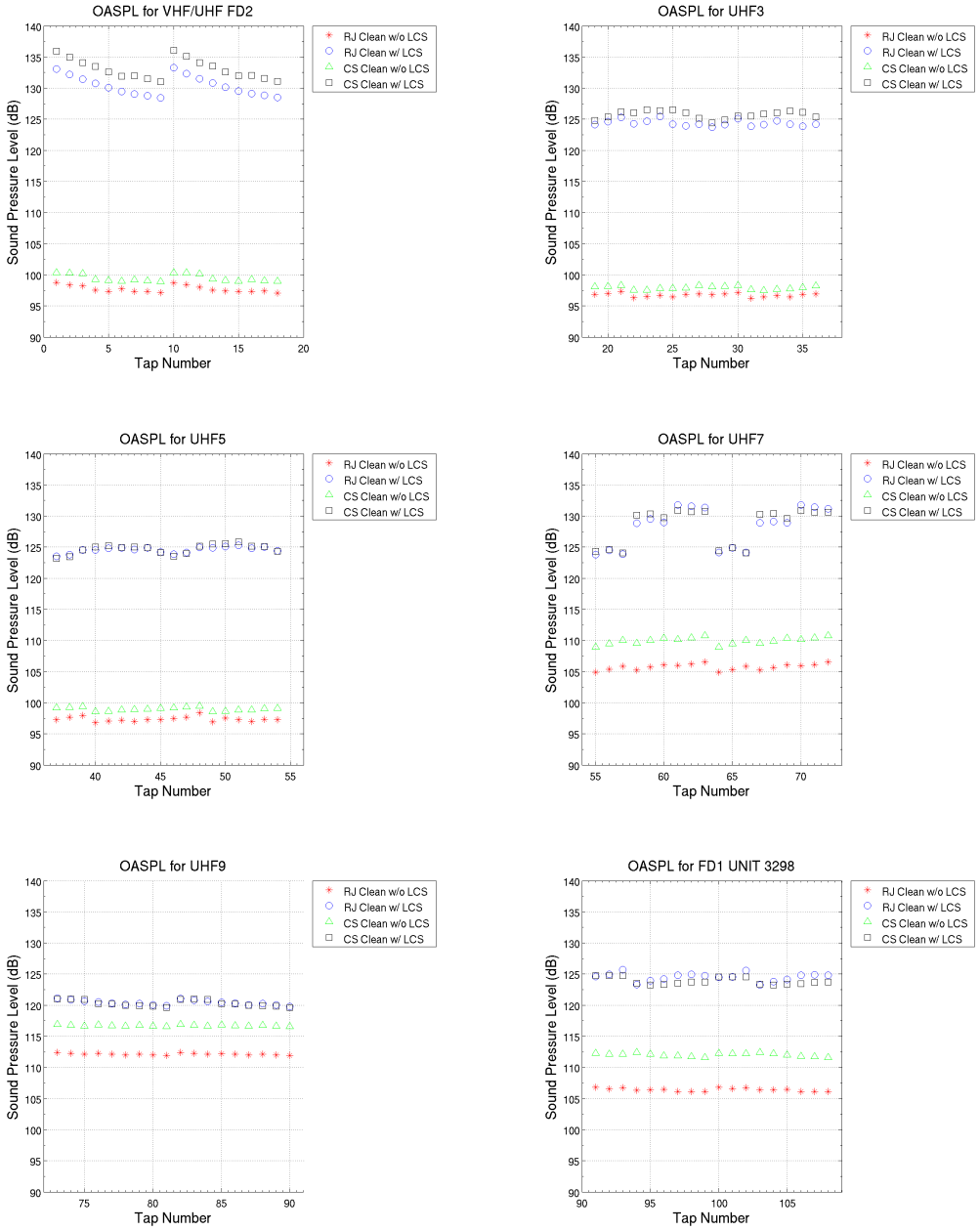


Figure C.1: Overall sound pressure levels at all tap locations for baseline study

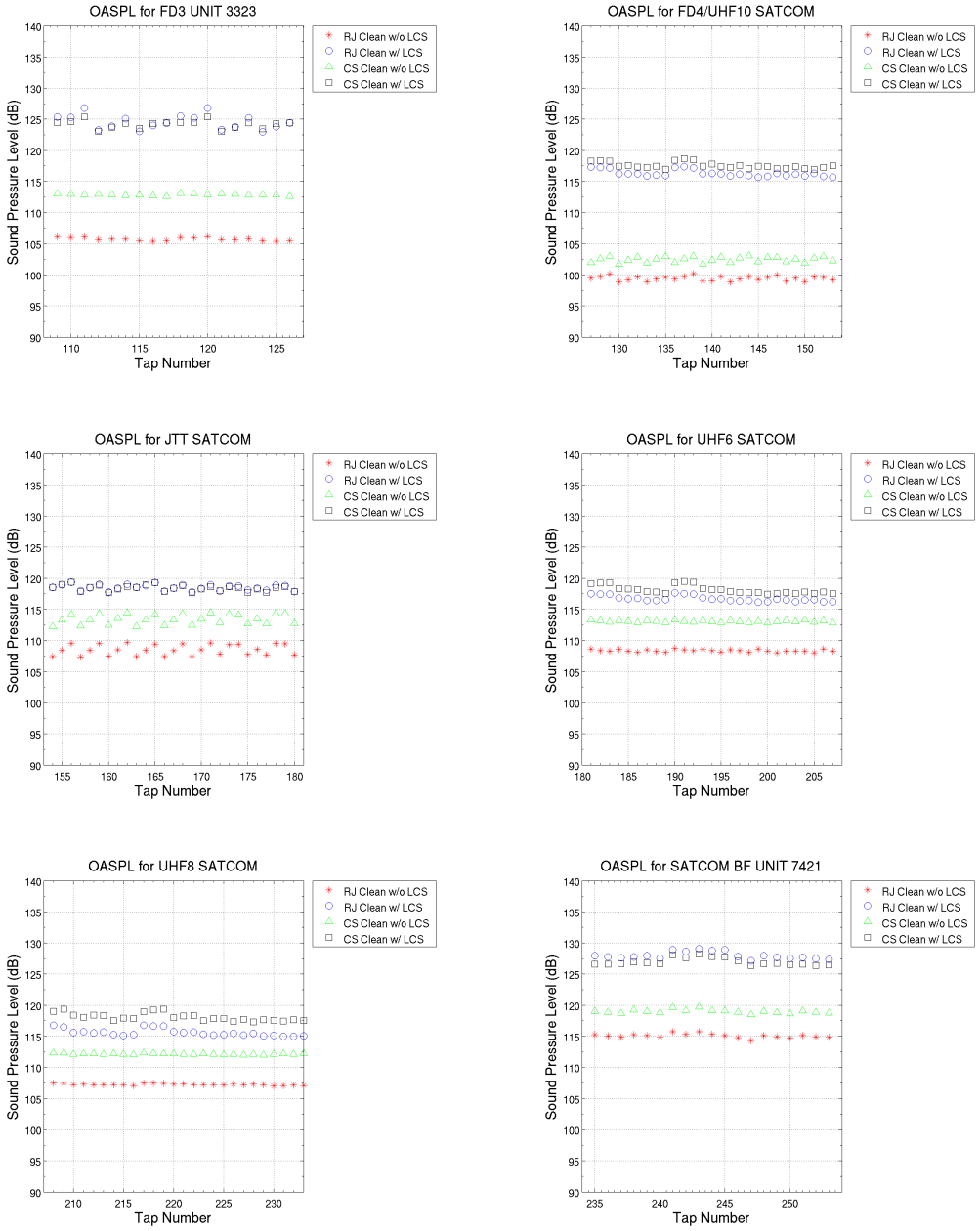


Figure C.2: Overall sound pressure levels at all tap locations for baseline study

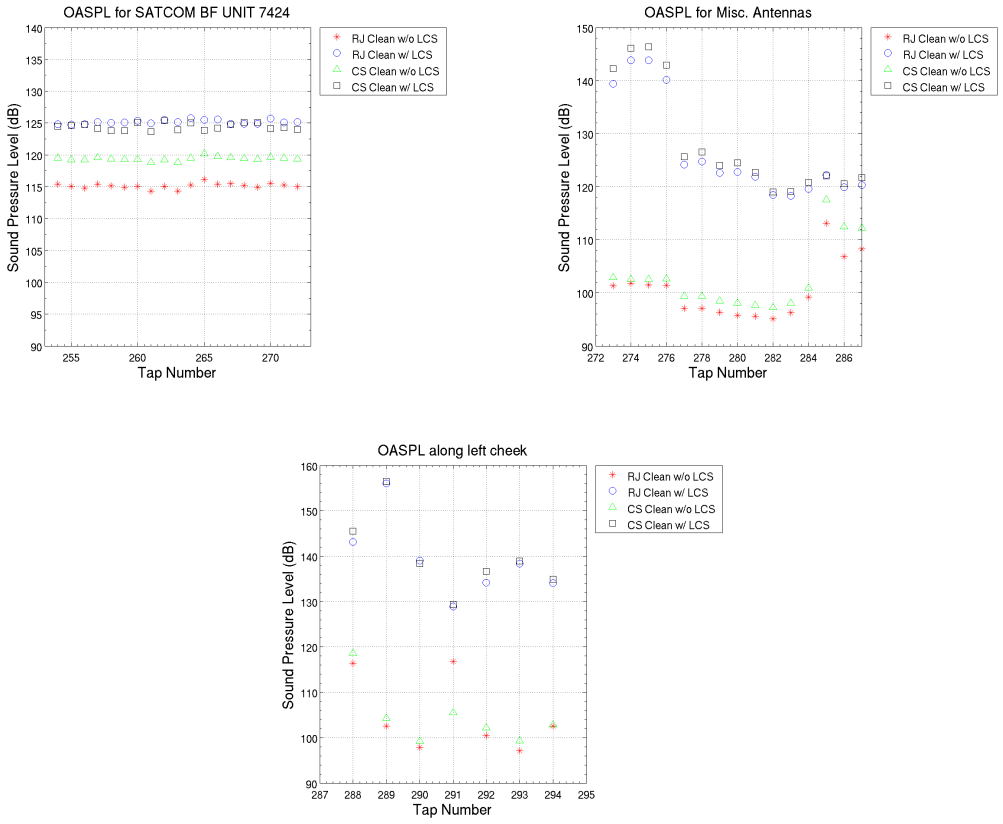


Figure C.3: Overall sound pressure levels at all tap locations for baseline study

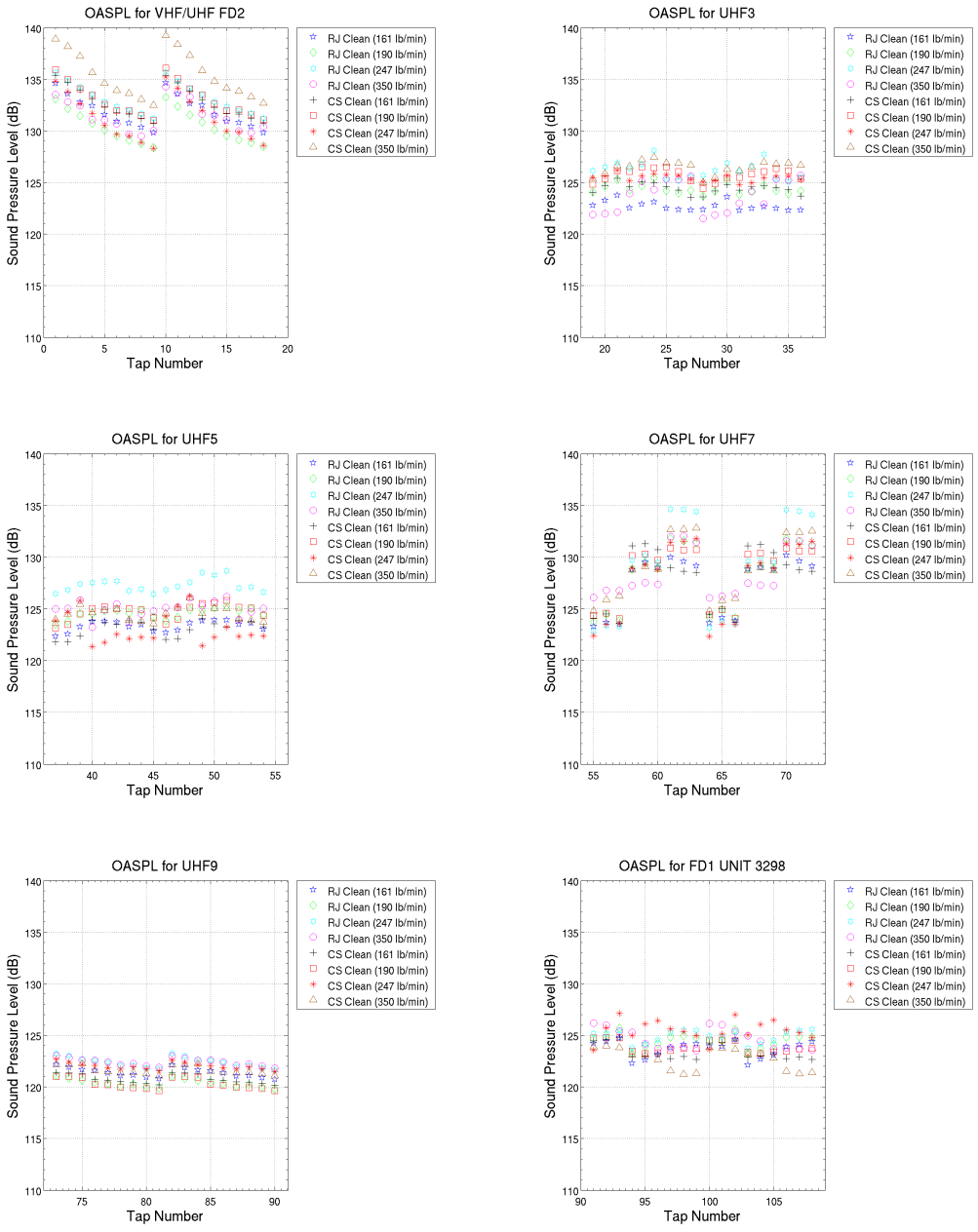


Figure C.4: Overall sound pressure levels at all tap locations for mass flow rate sensitivity study

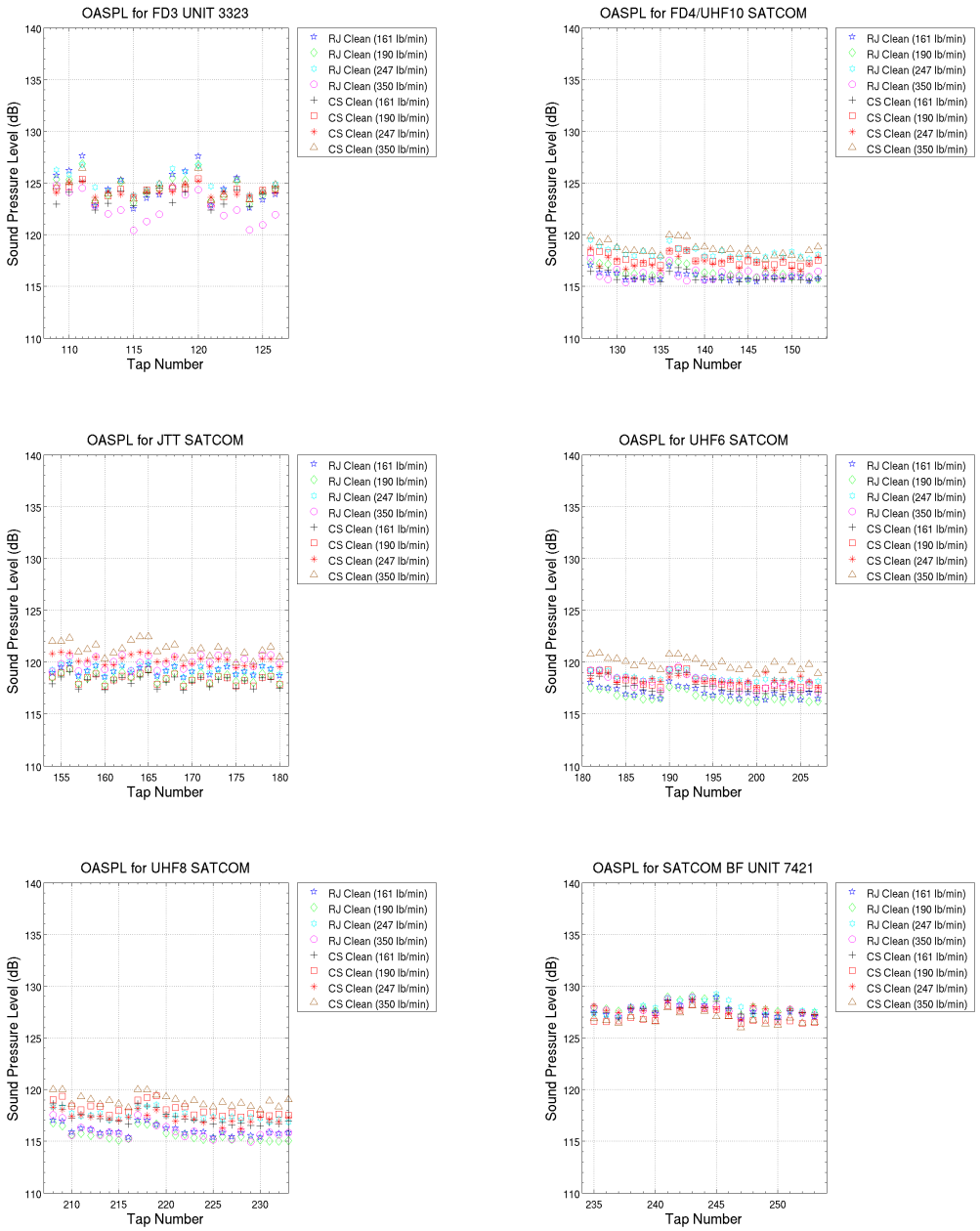


Figure C.5: Overall sound pressure levels at all tap locations for mass flow rate sensitivity study

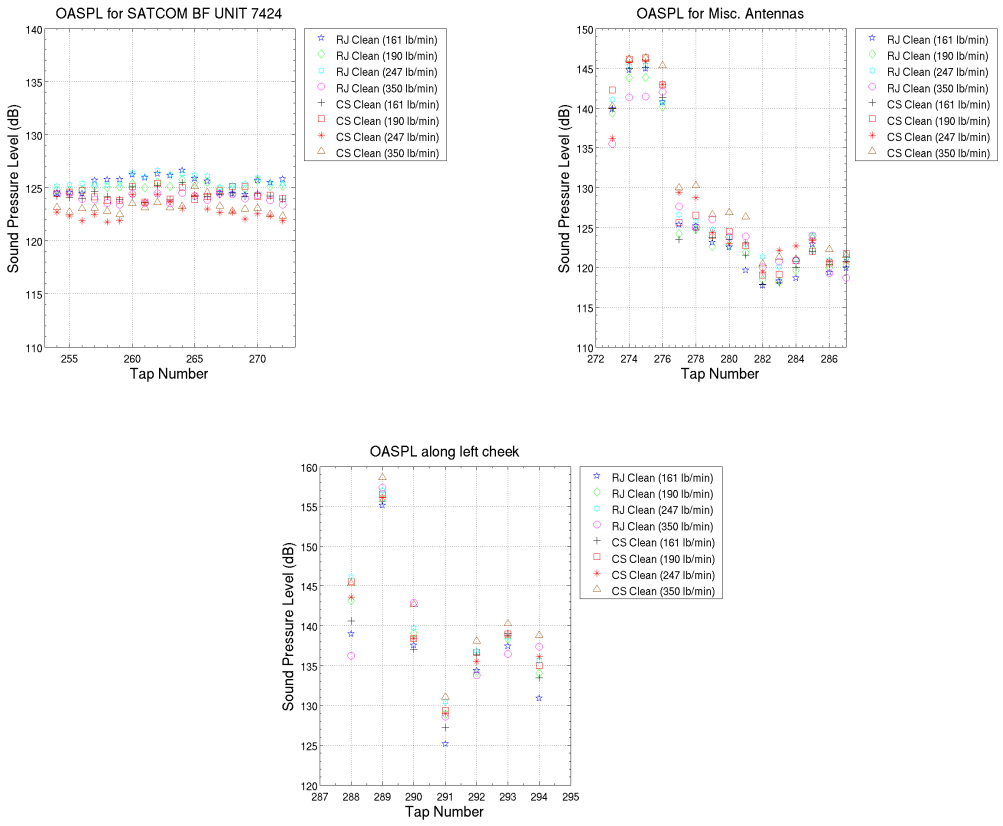


Figure C.6: Overall sound pressure levels at all tap locations for mass flow rate sensitivity study

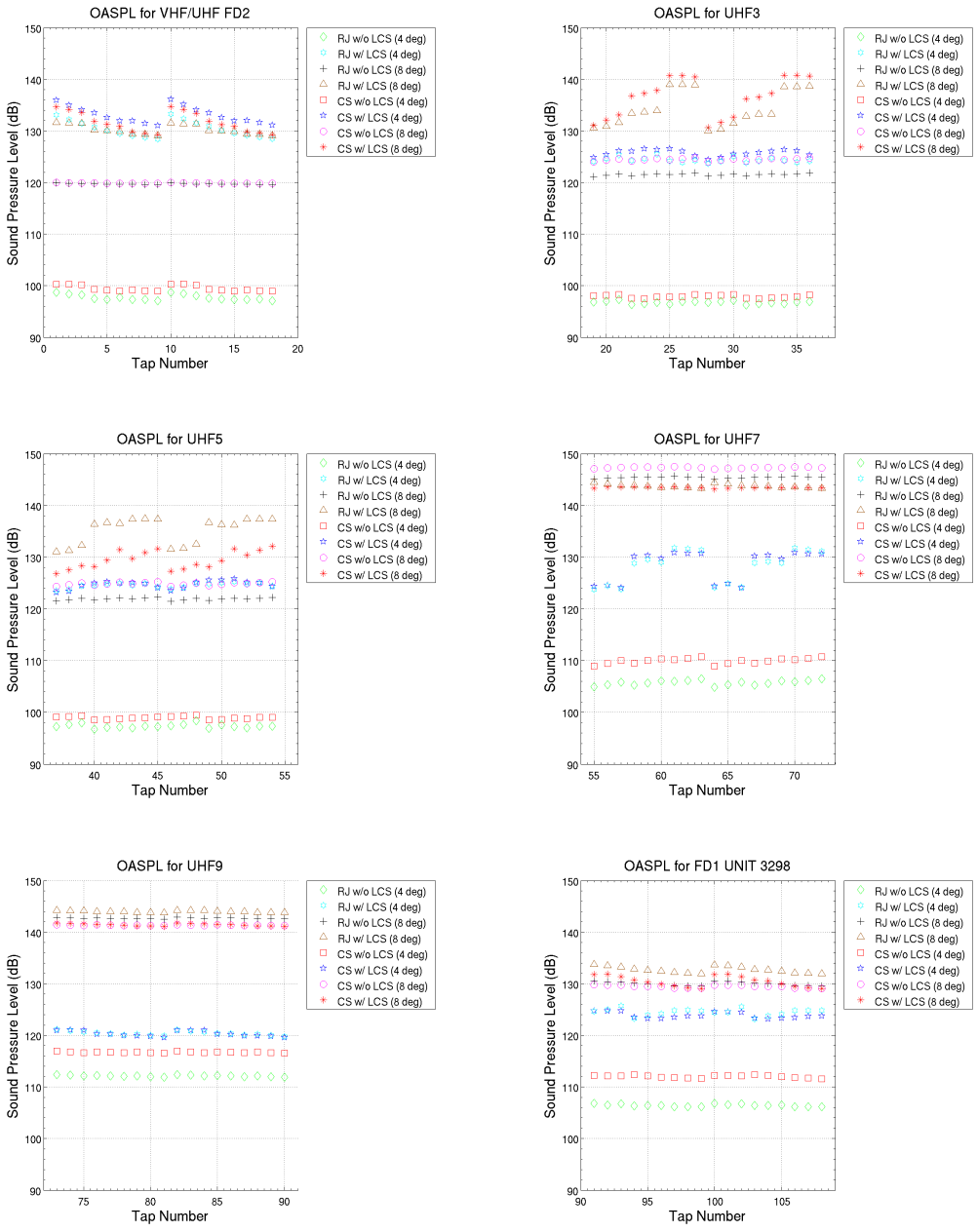


Figure C.7: Overall sound pressure levels at all tap locations for angle-of-attack sensitivity study

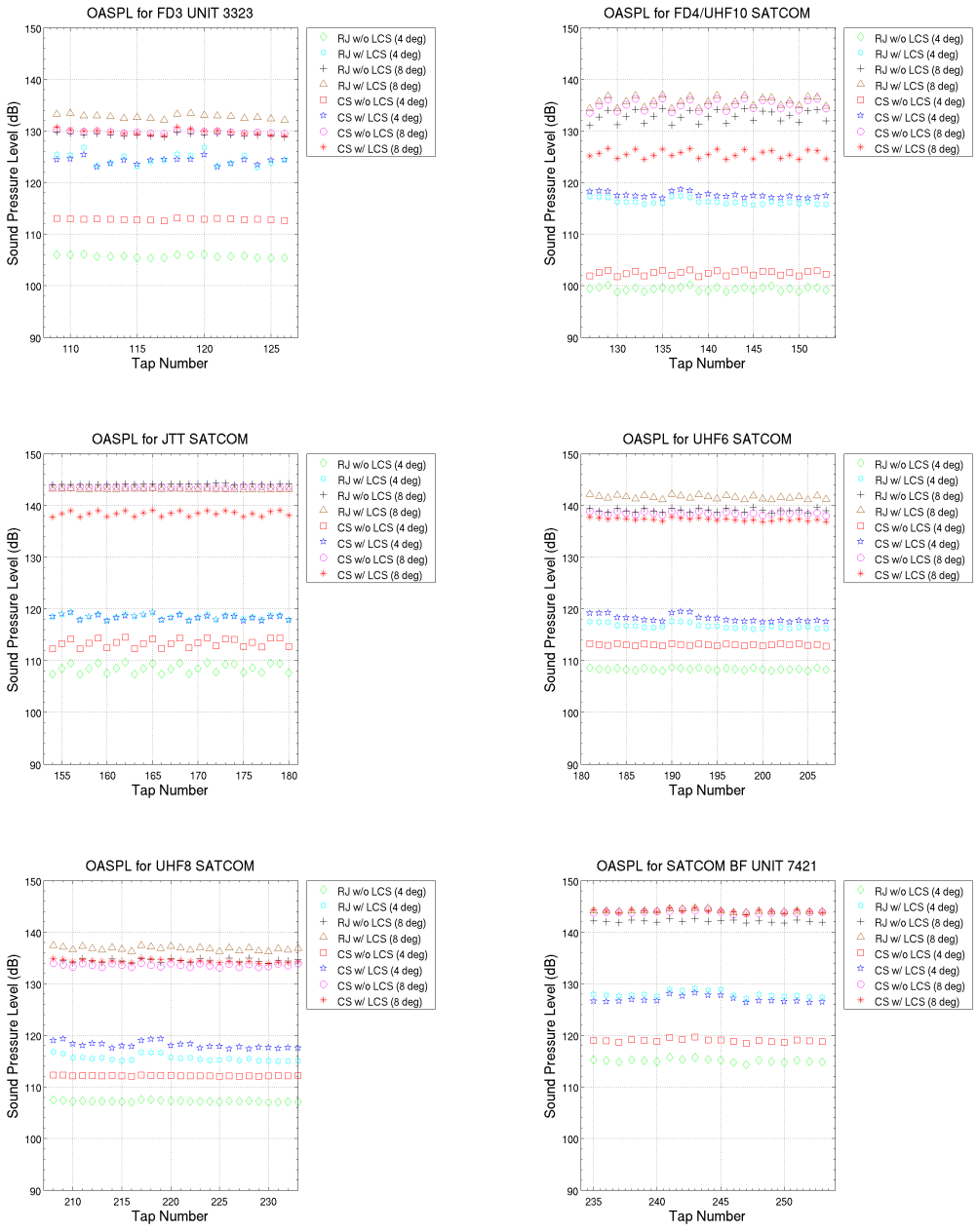


Figure C.8: Overall sound pressure levels at all tap locations for angle-of-attack sensitivity study

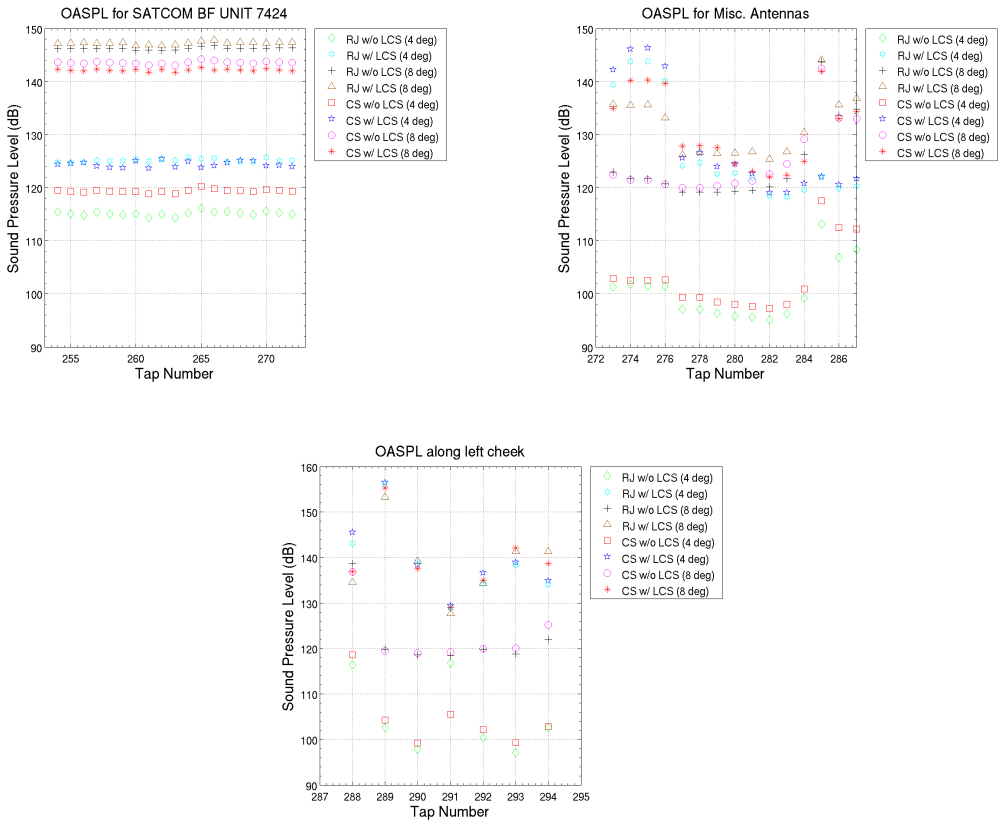


Figure C.9: Overall sound pressure levels at all tap locations for angle-of-attack sensitivity study

## *Bibliography*


1. http://www.jetphotos.net.
2. L. D. Burks, "Bl9 antenna-locations.ppt," October 2008.
3. TSgt Bobic, "UHF 3 Antenna vs. Long-wire." Powerpoint Presentation, November 2009.
4. R. H. Nichols, "Turbulence models and their application to complex flows, revision 4.01." University of Alabama at Birmingham, 2001.
5. P. R. Spalart, S. Deck, M. L. Shur, K. D. Squires, M. K. Strelets, and A. Travin, "A new version of detached-eddy simulation, resistant to ambiguous grid densities," *Theoretical and Computational Fluid Dynamics*, vol. 20, pp. 181–195, 2006.
6. D. J. Mavriplis, J. C. Vassberg, E. N. Tinoco, M. Mani, O. P. Brodersen, and B. Eisfeld, "Grid quality and resolution issues from the drag prediction workshop series," *46th AIAA Aerospace Sciences Meeting and Exhibit, Reno, NV*, January 2008. AIAA 2008-930.
7. J. T. Spivey, "CS1 Antennas Flight Vibration Results," Tech. Rep. G14156.04.32, L-3 Communications, 2010.
8. J. T. Spivey, "Continuing RJ BL9 UHF3 Antenna Failures." Memo 8-81900C/10M-018, February 2010.
9. R. M. Cummings, S. A. Morton, and D. R. McDaniel, "Experiences in accurately predicting time-dependent flows," *Progress in Aerospace Sciences*, vol. 44, pp. 241–257, April 2008 2008.
10. "U.S. Air Force Fact Sheet: RC-135V/W RIVET JOINT," November 2011. http://www.af.mil/information/factsheets/factsheet.asp?id=121.
11. "U.S. Air Force Fact Sheet: RC-135U COMBAT SENT," November 2011. http://www.af.mil/information/factsheets/factsheet.asp?id=191.
12. Boeing, *Substantiating Report for the RC-135/CFM56-2B-1 Flight Manual, Volume 1*, July 2007.
13. D. C. Stumpff. Personal Correspondence, March 2012. AFMC 645 AESG/WIJE.
14. J. D. Anderson, *Modern Compressible Flow: With Historical Perspective*. McGraw-Hill, 3rd ed., 2004.
15. F. M. White, *Viscous Fluid Flow*. McGraw-Hill, 3rd ed., 2006.
16. W. Z. Strang, R. F. Tomaro, and M. J. Grismer, "The Defining Methods of Cobalt60: A Parallel, Implicit, Unstructured Euler/Navier-Stokes Flow Solver," *37th AIAA Aerospace Sciences Meeting and Exhibit, Reno, NV*, January 1999. AIAA 99-0786.

17. J. Blazek, *Computational Fluid Dynamics: Principles and Applications*. Elsevier, 2005.

18. P. R. Spalart and S. R. Allmaras, "A one-equation turbulence model for aerodynamic flows," *30th Aerospace Sciences Meeting and Exhibit, Reno, NV*, January 1992. AIAA 92-0439.

19. F. R. Menter and M. Kuntz, "Adaptation of eddy-viscosity turbulence models to unsteady separated flow behind vehicles," *Symposium on the aerodynamics of heavy vehicles:trucks, buses, and trains, Monterey, USA*, Dec 2002.

20. CREATE-AV, Eglin AFB, FL, *Kestrel User's Guide*. Version 2.0.

21. S. Godunov, "A finite difference method for the numerical calculation of discontinuous solutions of the equations of fluid dynamics," *Matematicheskii Sbornik*, vol. 47, pp. 271–290, 1959.

22. B. van Leer, "Towards the ultimate conservative difference scheme," *Journal of Computational Physics*, vol. 32, pp. 101–136, 1979.

23. R. Tomaro, W. Strang, and L. N. Sankar, "An implicit algorithm for solving time dependent flows on unstructured grids," *AIAA*, vol. 97-0333, pp. 1–10, 1997.

24. R. W. MacCormack, "The effect of viscosity in hypervelocity impact cratering," *AIAA Hypervelocity Impact Conference*, 1969.

25. J. C. R. Hunt, A. Wray, and P. Moin, "Eddies, stream, and convergence zones in turbulent flows," *Center for Turbulence Research Report*, vol. CTR-S88, 1988.

26. G. Haller, "An objective definition of a vortex," *Journal of Fluid Mechanics*, vol. 525, pp. 1–26, September 3, 2004 2005.

27. A. Dauptain, "Spectral analysis for computational fluid dynamics." April 2011.

28. F. J. Harris, "On the use of windows for harmonic analysis with the discrete fourier transform," *Proceedings of the IEEE*, vol. 66, pp. 51–83, 1978.

29. P. D. Welch, "The use of fast fourier transform for the estimation of power spectra: A method based on time averaging over short, modified periodograms," *IEEE Transactions on Audio and Electroacoustics*, vol. AU-15, no. 2, pp. 70–73, 1967.

30. AFRL DSRC, *Raptor User Guide*.

31. "Top500 Supercomputer Sites," Nov 2011. http://i.top500.org/site/49284.

32. L. P. Davis, C. J. Henry, R. L. Campbell, and W. A. Ward, "High-performance computing acquisitions based on the factors that matter," *Computing in Science and Engineering*, pp. 35–44, November/December 2007.

33. *ANSYS ICEM CFD Release 13.0 Help Manual*, Nov 2010.

34. P. R. Spalart, "Young-person's guide to detached-eddy simulation grids," Tech. Rep. CR-2001-211032, NASA, 2001.

35. Air Force Research Lab CFD Research Branch, Wright-Patterson AFB, OH 45433-7521, *Air Vehicles Unstructured Solver (AVUS) User's Manual*, January 2005.

36. D. McDaniel. Personal Correspondence, Mar 2012.

# *Vita*

Captain Michael G. Chenery graduated from Millbrook High School in Raleigh, North Carolina. He then entered undergraduate studies at North Carolina State University, where he graduated with a degree in Aerospace Engineering in May 2006. He received his commission from Air Force Reserve Officer Training Corps Detachment 595.

In June 2006, he was assigned to the 625th Strategic Operations Squadron (formerly 625th Missile Operations Flight) at Offutt Air Force Base in Nebraska. Here he served as a ballistic missile trajectory engineer on a team dedicated to early warning and missile defense analysis for Air Force Space Command (AFSPC). In this role, he provided performance characterizations of foreign ballistic missile systems and maintained performance databases in support of United States Strategic Command (USSTRATCOM), AFSPC, and other DOD agencies.

In August 2010, he entered the Graduate School of Engineering and Management at the Air Force Institute of Technology located on Wright-Patterson AFB in Ohio. Upon graduation he will be assigned to the National Air and Space Intelligence Center (NASIC), where he will be the flight commander of Ballistic Missile Systems and Operations - West (SMB-W).

Permanent address: 2950 Hobson Way
Air Force Institute of Technology
Wright-Patterson AFB, OH 45433

# REPORT DOCUMENTATION PAGE

*Form Approved*
*OMB No. 0704–0188*



| 1. REPORT DATE (DD–MM–YYYY) | 2. REPORT TYPE | 3. DATES COVERED *(From — To)* |
|---|---|---|
| 22-03-2012 | Master's Thesis | August 2010 to March 2012 |

**4. TITLE AND SUBTITLE**
Computational Analysis and Characterization of RC-135 External Aerodynamics

5a. CONTRACT NUMBER
5b. GRANT NUMBER
5c. PROGRAM ELEMENT NUMBER

**6. AUTHOR(S)**
Michael G. Chenery, Capt, USAF

5d. PROJECT NUMBER
5e. TASK NUMBER
5f. WORK UNIT NUMBER

**7. PERFORMING ORGANIZATION NAME(S) AND ADDRESS(ES)**
Air Force Institute of Technology
Graduate School of Engineering and Management (AFIT/ENY)
2950 Hobson Way
WPAFB OH 45433-7765

**8. PERFORMING ORGANIZATION REPORT NUMBER**
AFIT/GAE/ENY/12-M06

**9. SPONSORING / MONITORING AGENCY NAME(S) AND ADDRESS(ES)**
645 AESG/WIJE
2530 Loop Rd West
Wright-Patterson AFB, OH 45433-7101
POC: David C. Stumpff
COMM: (937)255-2096
E-MAIL: David.Stumpff@wpafb.af.mil

10. SPONSOR/MONITOR'S ACRONYM(S)
645 AESG/WIJE

11. SPONSOR/MONITOR'S REPORT NUMBER(S)

**12. DISTRIBUTION / AVAILABILITY STATEMENT**
APPROVED FOR PUBLIC RELEASE; DISTRIBUTION UNLIMITED

**13. SUPPLEMENTARY NOTES** This material is declared a work of the U.S. Government and is not subject to copyright protection in the United States.

**14. ABSTRACT**

Both the RC-135V/W Rivet Joint (RJ) and the RC-135U Combat Sent (CS) aircraft are United States Air Force (USAF) electronics reconnaissance platforms. The RJ is the USAF's standard airborne signals intelligence (SIGINT) gathering platform, while the CS is designed to collect technical intelligence on adversary radar emitter systems. Both aircraft are extensively modified C-135's characterized by protruding "cheek" fairings along the sides of the fuselage forward of the wings as well as the addition of numerous antennas along the top and bottom of the fuselage. The major distinguishing feature between the two variants is the nose radome, wherein the RJ has an elongated nose while the CS has the standard C-135 nose with a protruding "chin" radome along the underside. The RJ has recently experienced problems with antenna buffeting resulting in broken antennas and damage to the aircraft. Flight testing confirmed the presence of unsteady loading on certain antennas that has been traced back to the turbulent exhaust flow of a liquid cooling system (LCS) installed in the forward cheek fairings. Both variants have this modification but only the RJ has experienced structural damage. Computational fluid dynamics (CFD) was applied with the intention of characterizing the differences between the two variants. The LCS mass flow rate, angle of attack, and configuration of each variant was altered and results compared. Slight differences in the flow-field about each variant were noted with very similar turbulent fluctuations observed with the LCS installed. A strong correlation to angle of attack was confirmed while a weak correlation to mass flow rate was discerned.

**15. SUBJECT TERMS**
Computational Fluid Dynamics

| 16. SECURITY CLASSIFICATION OF: | | | 17. LIMITATION OF ABSTRACT | 18. NUMBER OF PAGES | 19a. NAME OF RESPONSIBLE PERSON |
|---|---|---|---|---|---|
| a. REPORT | b. ABSTRACT | c. THIS PAGE | | | Andrew J. Lofthouse, Maj, USAF |
| U | U | U | UU | 135 | 19b. TELEPHONE NUMBER (Include Area Code) (937)674-4043; andrew.lofthouse@wpafb.af.mil |

**Standard Form 298 (Rev. 8–98)**
***Prescribed by ANSI Std. Z39.18***